

# Further development and application of the 3D microclimate simulation ENVI-met

Dissertation  
zur Erlangung des Grades

“Doktor der Naturwissenschaften”

im Promotionsfach Geographie

am Fachbereich Chemie, Pharmazie und Geowissenschaften  
der Johannes Gutenberg-Universität  
in Mainz

Sebastian Huttner  
geb. in Scherzingen

Mainz, den 26.04.2012

Dekan:

1. Berichtstatter:

2. Berichtstatter:

Tag der mündlichen Prüfung: 25. April 2012

D77 (Dissertation Universität Mainz)

## Zusammenfassung

Da die Zusammenhänge zwischen städtebaulichen bzw. architektonischen Maßnahmen und dem Mikroklima höchst komplex sind kann deren Einfluss auf das Mikroklima letztendlich nur mit Hilfe hochaufgelöster meteorologischer Simulationen, wie z.B. der Mikroklimasimulation ENVI-met, vorhergesagt werden.

Die vorliegende Dissertation beschreibt die technische Weiterentwicklung der Mikroklimasimulation ENVI-met in den Jahren 2007 bis 2010. Darüber hinaus enthält die Arbeit auch Beispiele für die Untersuchung von mikroklimatischen Fragestellungen im städtischen Umfeld.

Die Arbeit gliedert sich dabei in sechs Kapitel:

Kapitel eins und zwei beschreiben die Motivation für die Arbeit bzw. den Modellaufbau und die physikalischen Grundlagen von ENVI-met in der aktuellen Version 3.1.

Das dritte Kapitel beschäftigt sich mit der Implementierung und Validierung eines verbesserten Moduls zur Berechnung der Energie- und Temperaturflüsse an Fassaden und Dächern. Das neue Modul erlaubt eine detailliertere und akkuratere Aussage über den Einfluss verschiedener Fassadenmaterialien und -farben auf das Mikroklima in ihrer Umgebung. Darüber hinaus kann das neue Modul eine Schnittstelle zu Modellen für die Energiebilanzrechnung von Gebäuden genutzt werden. Ein erster Vergleich zwischen simulierten und gemessenen Dachoberflächentemperaturen zeigt eine gute Übereinstimmung.

Das vierte Kapitel beschreibt die Funktionsweise einer neuen Schnittstelle von ENVI-met welche es erlaubt Tagesgänge für verschiedene meteorologische Parameter wie Windrichtung und -stärke, Temperatur, Luftfeuchte und Strahlung vorzugeben. In vorherigen Versionen von ENVI-met war es nur möglich stark idealisierte Tagesgänge zu berechnen. Die neue Schnittstelle ermöglicht nun erstmals den genauen Vergleich zwischen gemessenen und simulierten Werten. In einem ersten Test wurden Messungen in zwei Gebieten mit den Ergebnissen von Simulationen verglichen welche Daten von einer meteorologischen Messstation außerhalb der Modellgebiete nutzten um die atmosphärischen Bedingungen an den Einströmrändern des Modellgebiets vorzugeben. Dieser Vergleich zeigt eine insgesamt gute Übereinstimmung.

Das fünfte Kapitel behandelt die Analyse von Simulationen welche mit ENVI-met im Rahmen des KLIMES Projekts durchgeführt wurden. Im ersten Teil des Kapitels werden zwei Stadtviertel von Freiburg - Vauban und Wiehre - auf den thermischen Komfort im Straßenraum an einem Hitzetag hin untersucht. Im zweiten Teil des Kapitels wird die Auswirkung verschiedener städtebaulicher und architektonischer Maßnahmen auf den thermischen Komfort in einer Straßenschlucht diskutiert. In beiden Teilen des Kapitels zeigt sich, dass im Bezug auf thermischen Komfort, das Pflanzen von Bäumen mit einem dichten Kronendach das größte Verbesserungspotential erbringt.

Im abschließenden sechsten Kapitel wird die Parallelisierung von ENVI-met auf Grafikkarten mittels der Programmiersprache OpenCL beschrieben. Da diese Maßnahme in der Praxis nicht den erwünschten Erfolg gebracht hat wird darüber hinaus diskutiert wie ENVI-met mittels Gebietszerlegung in Zukunft von der Parallelisierung auf mehrere CPUs profitieren könnte.

## Abstract

As the interaction between urban planning respectively architecture and the microclimate are very complex their influence on the microclimate can only be predicted by means of high resolution meteorological models like e.g. the microclimate simulation ENVI-met.

This dissertation describes the technical further development of the microclimate simulation ENVI-met in the years from 2007 to 2010 and shows examples of how ENVI-met can help solve typical microclimatic questions within an urban environment.

The work is divided into six chapters:

Chapter one describes the motivation for the work. Chapter two gives a short introduction to ENVI-met 3.1 and its physical foundations.

Chapter three describes the implementation and validation of an enhanced module for the calculation of the fluxes of energy and temperature within facades and roofs. The new module allows a more detailed and accurate prediction of the influence of different facade materials and colors on the microclimate in their vicinity. Furthermore the new module can be used as an interface with models that calculate the energy balance of buildings. A first comparison between measurements of roof temperatures and their simulated values shows a good agreement.

The fourth chapter of this work describes a new interface of ENVI-met that allows the user to define the diurnal variations for different meteorological parameters like wind speed and direction, air temperature, air humidity and solar irradiation at the boundaries of the model area. Previous versions of ENVI-met could only model heavily idealized diurnal variations. The new interface now allows for the first time to compare measurements and simulations. It was tested at two model areas. For the simulations the measurements of a meteorological station outside the model areas was used to create the boundary conditions of the simulations. The comparison between measured and simulated values shows a good overall accordance.

Chapter five describes the analysis of simulations with ENVI-met that were run in the framework of the KLIMES project. The first part of this chapter analyzes the human thermal comfort on street level in two urban quarters of Freiburg - Vauban and Wiehre - on a hot summer day. The second part of the chapter discusses the influence of different urbanistic and architectural measurements on the human thermal comfort within a street canyon on a hot summer day. Both parts of this chapter conclude that trees with a dense crown layer show the most positive impact on the human thermal comfort within street level.

The sixth chapter describes the parallelization of ENVI-met onto graphic cards via the programming language OpenCL. As the speedup of this parallelization is well below expectations the second part of the chapter contains a discussion on how ENVI-met could profit from a parallelization onto several cores of the CPU via domain decomposition.

# Contents

<b>I. Introduction</b>	<b>1</b>
<b>II. Concept of ENVI-met</b>	<b>5</b>
1. Summary	5
2. Introduction	5
3. Grid layout	5
4. Model physics	7
4.1. Wind flow . . . . .	8
4.2. Temperature and humidity . . . . .	10
4.3. Atmospheric turbulence . . . . .	10
4.4. Radiation . . . . .	11
4.5. Soil model . . . . .	13
4.6. Vegetation model . . . . .	14
4.7. Ground surfaces . . . . .	15
4.8. Building surfaces . . . . .	16
4.9. Gases and particles . . . . .	16
4.10. Initialization & boundary conditions . . . . .	17
4.11. Thermal comfort indices . . . . .	17
4.11.1. Calculation of the mean radiant temperature in ENVI-met . . . . .	19
4.11.2. BOTworld - calculation of a dynamic comfort index . . . . .	20
5. Numerical solution techniques	20
6. Shortcomings of ENVI-met	21
7. Conclusion	22
<b>III. Introducing a prognostic 3-node wall and roof model in the micro climate simulation ENVI-met</b>	<b>27</b>
1. Summary	27
2. Introduction	27
3. Physics	28
3.1. The original estimation of the facade temperature . . . . .	28
3.2. The new 3-node model . . . . .	29

3.3. Estimate of absorbed long wave radiation . . . . .	31
3.4. Calculation of indoor temperature . . . . .	32
<b>4. Comparison between new and old model</b>	<b>34</b>
<b>5. Single walls</b>	<b>36</b>
<b>6. Remodeling the ENVI-met editor</b>	<b>37</b>
<b>7. Validation</b>	<b>40</b>
7.1. Model area . . . . .	40
7.2. Simulation . . . . .	41
7.3. Modeled roof elements . . . . .	43
7.4. Comparison . . . . .	43
<b>8. Conclusions</b>	<b>46</b>
<b>IV. Implementing user-defined atmospheric boundary conditions into the numerical microclimate simulation ENVI-met</b>	<b>51</b>
<b>1. Summary</b>	<b>51</b>
<b>2. Introduction</b>	<b>51</b>
<b>3. ENVI-met model run without forcing</b>	<b>52</b>
<b>4. Nesting and Nudging - making climate simulations match observations</b>	<b>53</b>
4.1. Nesting - general . . . . .	53
4.2. Nudging - general . . . . .	55
4.3. Nesting, Nudging and ENVI-met . . . . .	56
<b>5. Concept of Forcing in ENVI-met</b>	<b>56</b>
<b>6. Forcing in ENVI-met</b>	<b>57</b>
6.1. Variables that can be forced . . . . .	57
6.2. Input data . . . . .	57
6.3. Radiation . . . . .	58
6.3.1. Cloud cover . . . . .	59
6.3.2. Radiation . . . . .	59
6.4. Gas and particles . . . . .	59
6.5. Wind speed . . . . .	59
6.6. Wind direction, potential air temperature and humidity . . . . .	60
<b>7. Preprocessing the data</b>	<b>60</b>

<b>8. Forcing simulations</b>	<b>60</b>
<b>9. Case studies</b>	<b>61</b>
9.1. Setup . . . . .	61
9.2. Model areas . . . . .	61
9.3. Model area 1: Erbprinzenstrasse . . . . .	61
9.4. Model area 2: Vauban . . . . .	62
9.5. Input data . . . . .	63
9.6. Simulations . . . . .	63
<b>10. Results</b>	<b>64</b>
10.1. Erbprinzenstrasse . . . . .	64
10.1.1. Mean radiant temperature . . . . .	65
10.1.2. Wind speed . . . . .	66
10.1.3. Temperature and relative humidity . . . . .	66
10.1.4. Physiologically equivalent temperature . . . . .	67
10.2. Vauban . . . . .	67
<b>11. Discussion</b>	<b>67</b>
<b>12. Conclusion</b>	<b>68</b>
<b>V. Simulating the urban microclimate with ENVI-met</b>	<b>71</b>
<b>1. Summary</b>	<b>71</b>
<b>2. Simulating the impact of global warming on the summerly urban microclimate in Central Europe</b>	<b>72</b>
2.1. Introduction . . . . .	72
2.2. Model areas . . . . .	72
2.3. Model area Vauban . . . . .	74
2.4. Model area Wiehre . . . . .	74
2.5. Boundary conditions . . . . .	75
2.6. Simulations . . . . .	76
2.6.1. Results Vauban . . . . .	76
2.6.2. Results Wiehre . . . . .	82
2.7. General discussion and Conclusion . . . . .	82
<b>3. Simulating the impact of surface materials, vegetation and overhanging facades on human thermal comfort within a street canyon in Central European summers</b>	<b>85</b>
3.1. Introduction . . . . .	85
3.2. Model area . . . . .	85
3.3. Simulation . . . . .	87

3.4. Results . . . . .	88
3.4.1. Influence of orientation and H/W of street canyon . . . . .	88
3.4.2. Albedo of facades . . . . .	88
3.4.3. Emissivity of facades . . . . .	90
3.4.4. Facade surface temperature . . . . .	90
3.4.5. Trees . . . . .	91
3.4.6. Albedo of ground surface . . . . .	91
3.4.7. Galleries . . . . .	92
3.5. Discussion . . . . .	92
3.6. Conclusion . . . . .	95
<b>VI. Parallelization of ENVI-met</b>	<b>99</b>
<b>1. Summary</b>	<b>99</b>
<b>2. Introduction</b>	<b>99</b>
<b>3. GPGPU - theory</b>	<b>100</b>
3.1. GPU evolution . . . . .	100
3.2. GPU vs CPU . . . . .	100
3.3. GPU manufacturers . . . . .	101
<b>4. OpenCL</b>	<b>101</b>
4.1. Choosing the framework . . . . .	101
4.2. General information about OpenCL . . . . .	102
4.3. OpenCL architecture . . . . .	103
4.3.1. Execution model . . . . .	103
4.3.2. Memory model . . . . .	105
4.3.3. Programming Model . . . . .	106
<b>5. Implementation in ENVI-met</b>	<b>106</b>
5.1. Conversion from Delphi to C++ . . . . .	106
5.2. ADI-Routines . . . . .	107
5.3. Implementation . . . . .	110
<b>6. Results</b>	<b>111</b>
<b>7. Discussion</b>	<b>112</b>
<b>8. Alternative parallelization on CPUs</b>	<b>113</b>
8.1. Theory . . . . .	113
8.2. Proposition for an implementation into ENVI-met . . . . .	114
8.2.1. Decomposition of the model area . . . . .	114
8.2.2. Initialization . . . . .	116



8.2.3. Model run - exchange between sub-areas . . . . .	116
8.3. Discussion . . . . .	118
8.4. Summary . . . . .	118
<b>A. Index of symbols</b>	<b>122</b>
A.1. latin letters . . . . .	122
A.2. greek letters . . . . .	123
<b>B. Source code listings</b>	<b>123</b>
<b>C. List of figures</b>	<b>132</b>
<b>D. List of tables</b>	<b>135</b>



# Part I.

## Introduction

The human perception of atmospheric conditions is defined by processes taking place on two different scales. On the one hand there are large scale processes in the upper layers of the troposphere that govern the path of air masses on their way around the globe. These large scale processes define what we usually call “weather” by defining the path and exchange of air masses with different physical properties around the globe.

On the other hand there also are smaller scale processes within the lowest layer of the troposphere. The meteorological conditions within this layer are also influenced by the large scale processes, but the exchange processes between soil, water, buildings and plants and the atmosphere superimpose upon these large scale processes to create a special microclimate which can intensify or counteract large scale weather and climate trends.

The good - or bad - thing about microclimate is that humans can directly and almost instantaneously influence it. The best example for this human influence on microclimate is the so called urban heat island (UHI). The term UHI describes the observation that the air temperature in cities can be significantly higher than in the surrounding rural areas. This effect is caused by artificial surface materials, lower vegetation density and the modification of the wind field by buildings [Oke, 1982].

Because of the numerous interactions and non-linear correlations among the different aspects of microclimate it is not always possible to develop generalized guidelines for microclimatic advantageous urban planning and architecture. An action that might prove beneficial in one city, e.g. the optimization of wind flow, might have undesired side effects in another city with different (mesoscale) climate conditions. Therefore the best approach for urban planners and architects who want to assess the impact of their projects on urban microclimate is to simulate their specific project with the help of microclimate modeling software.

In order to accurately simulate the physics of the atmospheric boundary layer of an urban area the modeling software has to meet the following requirements:

- the grid size of the model area has to be small enough to resolve buildings, i.e. grid size  $\leq 10\text{m}$
- the model has to implement the energy balance of surfaces of all types
- the simulation of the physical and physiological properties of plants has to be included
- the calculation of the atmospheric processes should be prognostic and transient.

Most microscale models that are currently used in research and in urban planning only focus on a single aspect of microclimate and do therefore not fulfill all of the requirements mentioned above. Some models like MISKAM [Eichhorn, 1989] or MUKLIMO\_3

[Sievers, 1995] mainly focus on the wind field and the distribution of gases and aerosols within the atmosphere and neglect thermodynamical effects or the calculation of building surface temperatures. Other models like Solweig [Lindberg et al., 2008] or Rayman [Matzarakis et al., 2007] concentrate on the simulation of the radiation fluxes within the urban environment. Again other microscale models focus only on the interaction of plants with the microclimate [Mahrer and Avissar, 1984].

The three-dimensional microclimate model ENVI-met ([www.envi-met.com](http://www.envi-met.com)) is one of the few microscale models that fulfill all of the above-mentioned criteria. Development of the model was started in 1995 by Michael Bruse at the Ruhr-Universität Bochum. ENVI-met is freeware and runs - in contrast to many other climate simulations - on a standard x86 personal computer with a Microsoft Windows operating system. A version that runs on Unix operating systems has also recently become available.

As of 2010 ENVI-met has more than 1700 registered users from all over the world and is successfully used for research on air quality and urban microclimate in many different locations like Trier (Germany) [Junk et al., 2003], Lisbon (Portugal) [Andrade and Alforcado, 2008], Cairo (Egypt) [Fahmya et al., 2010], Sao Paulo (Brazil) [Spangenberg and Shinzato, 2008], Singapore [Wong and Jusuf, 2007] and Colombo (Sri Lanka) [Emmanuel et al., 2007], to name only a few.

This doctoral thesis describes the work on and with ENVI-met in the period between 2007 and 2010. The main part of the work performed in this time can be split into four different categories:

1. Development of a new, improved module for the calculation of the energy balance of facades and buildings.
2. Implementation of user defined atmospheric boundary conditions to allow ENVI-met to use real (measured) diurnal variations as inflow profiles or to nest ENVI-met into a mesoscale climate model.
3. Parallelization of ENVI-met onto a graphics card via OpenCL.
4. Numerical study of the bio-meteorological performance of different central European residential zones in summer conditions.

Each of these subjects is treated in its own section in this work.

The first section of this work gives a short overview on the concept and the model physics of ENVI-met.

## References

- H. Andrade and M. Alforçado. Microclimatic variation of thermal comfort in a district of lisbon (telheiras) at night. *Theoretical and Applied Climatology*, 92:225–237, 2008.
- J. Eichhorn. *Entwicklung und Anwendung eines dreidimensionalen mikroskaligen Stadtklima-Modells*. PhD thesis, Univ. Mainz, 1989. URL [http://www.staff.uni-mainz.de/eichhorn/docs/diss\\\_eichhorn\\\_1989](http://www.staff.uni-mainz.de/eichhorn/docs/diss\_eichhorn\_1989). PDF Retrieved 20.02.2011.
- R. Emmanuel, H. Rosenlund, and E. Johannson. Urban shading - a design option for the tropics? a study in colombo, sri lanka. *International Journal of Climatology*, 27(14):1859 – 1873, 2007.
- M. Fahmya, S. Sharplesa, and M. Yahiya. Lai based trees selection for mid latitude urban developments: A microclimatic study in cairo, egypt. *Building and Environment*, 45(2):345–357, 2010.
- J. Junk, A. Helbig, and J. Lüers. Urban climate and air quality in trier/germany. *International Journal of Biometeorology*, 47:230–238, 2003.
- F. Lindberg, B. Holmer, and S. Thorsson. Solweig 1.0 - modelling spatial variations of 3d radiant fluxes and mean radiant temperature in complex urban settings. *International Journal of Biometeorology*, 52:697–713, 2008. ISSN 0020-7128.
- Y. Mahrer and R. Avissar. A numerical simulation of the greenhouse microclimate. *Mathematics and Computers in Simulation*, 26(3):218 – 228, 1984.
- A. Matzarakis, F. Rutz, and H. Mayer. Modelling radiation fluxes in simple and complex environments - application of the rayman model. *International Journal of Biometeorology*, 51:323–334, 2007.
- T. Oke. The energetic basis of the urban heat island. *Quart. J. R. Met. Soc.*, 108:1–34, 1982.
- U. Sievers. Verallgemeinerung der stromfunktionsmethode auf drei dimensionen. *Meteorologische Zeitschrift*, 4:3–15, 1995.
- J. Spangenberg and P. Shinzato. Simulation of the influence of vegetation on microclimate and thermal comfort in the city of sao paulo. *Revista da Sociedade Brasileira de Arborizacao Urbana*, 3(2):1–19, 2008.
- N. Wong and S. Jusuf. Environmental study of the impact of greenery in an institutional campus in the tropics. *Building and Environment*, 42:2949–2970, 2007.



# Part II.

## Concept of ENVI-met

### 1. Summary

This section sums up the existing documentation of the microclimate simulation ENVI-met, version 3.1, and provides an overview on the general model concept. Additional features implemented in the course of the work of this doctoral thesis are outlined in the corresponding chapters. These new features will be made available to the public in future versions of ENVI-met.

### 2. Introduction

ENVI-met is a prognostic three-dimensional climate model. The main difference between ENVI-met and large-scale atmospheric models used for the prediction of the daily weather or future climate conditions is the temporal and spatial model resolution. With a typical spatial resolution between 0.5m and 10m and time steps of  $\leq 10$ s ENVI-met is simulating the interactions between atmosphere, soil, vegetation and buildings on a microscale level. Every single plant and every urban structure can explicitly be simulated, making ENVI-met the perfect tool for urban planners, architects and urban climatologists who want to simulate the meteorological components of the urban environment.

The following section sums up the existing documentation of ENVI-met and explains the basic model structure of ENVI-met and the physical equations and mathematical methods used in the different sub-models.

A more detailed but partly outdated documentation of the physical formulas and numerical methods used in ENVI-met can be downloaded from the ENVI-met website [Bruse, 2004b].

### 3. Grid layout

The ENVI-met model consists of several sub-models (fig: 2) that interact with each other:

- a 1D boundary model
- a 3D atmospheric model
- a 3D/1D soil model

The one-dimensional boundary model is mainly used for the initialization of the model and for the boundary conditions of the three-dimensional atmospheric model. It reaches from ground level ( $z=0$ ) up to a height of  $H = 2500m$  above ground level.

The three-dimensional model areas are divided into  $I \times J \times K$  rectangular grid cells with the dimensions  $\Delta x \times \Delta y \times \Delta z$ . Buildings, vegetation and the digital elevation model are constricted to this rectangular grid. This means that a cell is either fully occupied by one of these obstacles or not at all. Borders of objects that do not run parallel to the main axes  $x, y, z$  of the model area therefore have to be approximated by jagged borders. This is also true for semi-permeable obstacles like trees.

The horizontal spacings  $\Delta x$  and  $\Delta y$  are constant for all grid cells. The horizontal spacing of the grid cells  $\Delta z$  can be set to either constant or telescoping. In a constant vertical grid all grid cells have the same height  $\Delta z$  - except the lowest grid cell which is divided into five sub grid cells so that the vertical extension of these grid cells is  $0.2 \cdot \Delta z$ . The lower vertical resolution of the grid cells closest to the ground has the advantage that the exchange processes between atmosphere and ground, which have a substantial influence on the microclimate at ground level, can be simulated more accurately.

In a telescoping grid the vertical extension of the grids  $\Delta z$  increases with height (fig. 1). This allows a high vertical extension of the model area while keeping a higher resolution in the lower levels that are most interesting from a biometeorological point of view and where the majority of the overall energy transfer within the model area takes place.

The vertical spacing of the 3D model is also used for the 1D boundary model - up to

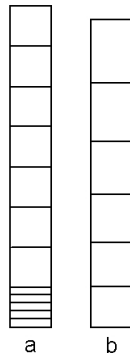


Figure 1: Schematic of vertical grid layout with a.) constant b.) telescoping grid

the upper boundary of the 3D model. The spacing of the cells of the 1D model which are between the top of the 3D model ( $Z$ ) and the top of the 1D model ( $H$ ) at 2500m above ground, is determined via an iteration that splits the remaining height  $H - Z$  into 15 cells with a telescoping grid. That is the vertical spacing of these cells increases with height above ground.

The soil model that is used to calculate temperature and humidity fluxes within the soil consists of  $I \times J \times N$  grid cells.  $N$  is currently set to 14 and the vertical spacing of these cells is a telescoping one reaching from ground level to 1.75m below ground level. The computation of the temperature and humidity fluxes within the soil is calculated only along the  $z$ -axis. Therefore the soil model itself has to be called a 1D model - despite its three-dimensional extent.



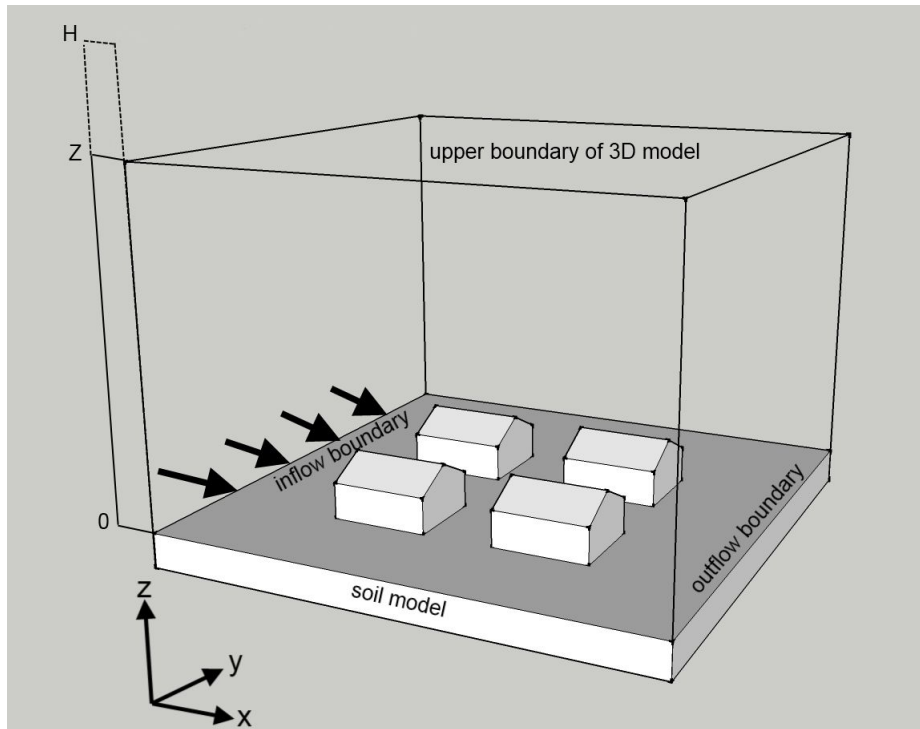


Figure 2: Schematic of basic model layout

#### 4. Model physics

The main prognostic variables calculated by ENVI-met are [Bruse and Fler, 1998]:

- wind speed and direction
- air and soil temperature
- air and soil humidity
- turbulence
- radiative fluxes
- gas and particle dispersion

For the calculation of these variables ENVI-met uses several sub-models (fig. 3) that are coupled with each other.

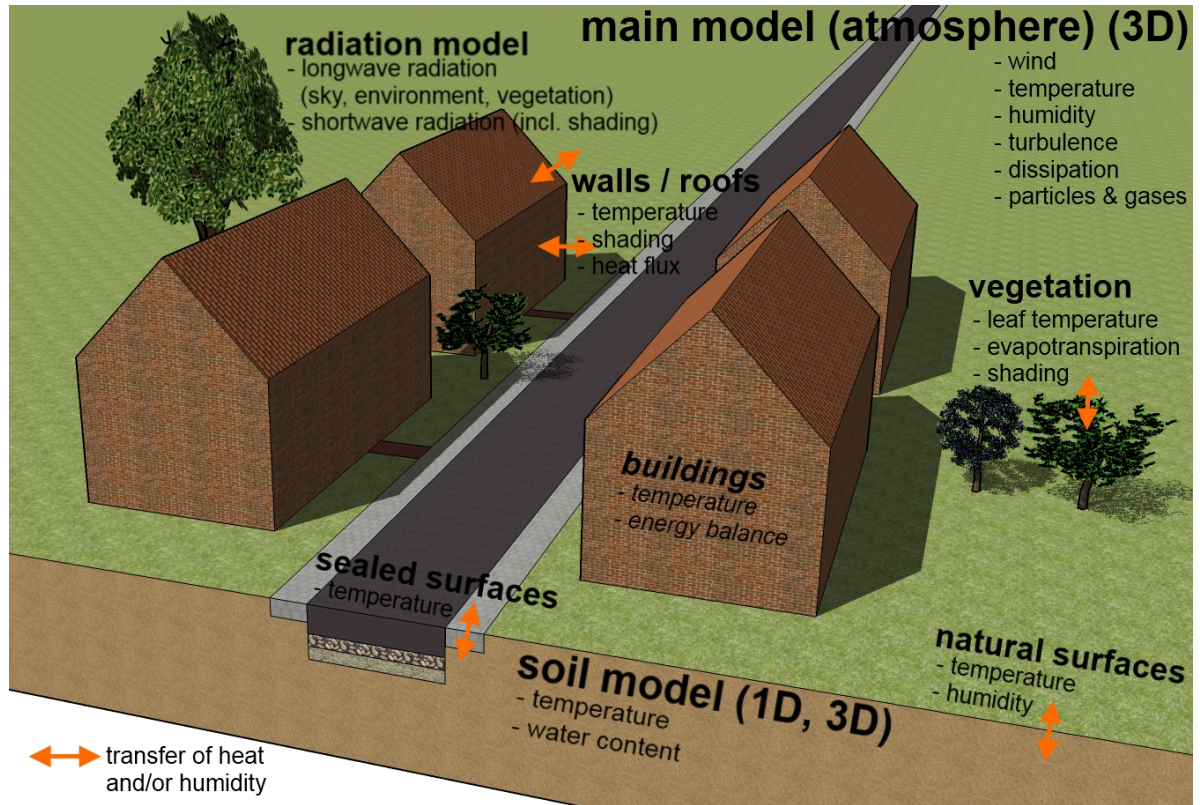


Figure 3: Schematic of the sub models of ENVI-met.

#### 4.1. Wind flow

The temporal and spatial development of the wind speed and direction is calculated using the three-dimensional non-hydrostatic Navier-Stokes equations:

$$\begin{aligned} \frac{\partial u}{\partial t} + u \frac{\partial u}{\partial x} + v \frac{\partial u}{\partial y} + w \frac{\partial u}{\partial z} = & \\ & - \frac{1}{\rho} \frac{\partial p'}{\partial x} + \frac{\partial}{\partial x} \left( K_m \frac{\partial u}{\partial x} \right) + \frac{\partial}{\partial y} \left( K_m \frac{\partial u}{\partial y} \right) + \frac{\partial}{\partial z} \left( K_m \frac{\partial u}{\partial z} \right) \\ & + f(v - v_g) - S_u(x, y, z) \quad (1a) \end{aligned}$$

$$\begin{aligned} \frac{\partial v}{\partial t} + u \frac{\partial v}{\partial x} + v \frac{\partial v}{\partial y} + w \frac{\partial v}{\partial z} = & \\ & - \frac{1}{\rho} \frac{\partial p'}{\partial y} + \frac{\partial}{\partial x} \left( K_m \frac{\partial v}{\partial x} \right) + \frac{\partial}{\partial y} \left( K_m \frac{\partial v}{\partial y} \right) + \frac{\partial}{\partial z} \left( K_m \frac{\partial v}{\partial z} \right) \\ & + f(u - u_g) - S_v(x, y, z) \quad (1b) \end{aligned}$$

$$\begin{aligned} \frac{\partial w}{\partial t} + u \frac{\partial w}{\partial x} + v \frac{\partial w}{\partial y} + w \frac{\partial w}{\partial z} = \\ - \frac{1}{\rho} \frac{\partial p'}{\partial z} + \frac{\partial}{\partial x} \left( K_m \frac{\partial w}{\partial x} \right) + \frac{\partial}{\partial y} \left( K_m \frac{\partial w}{\partial y} \right) + \frac{\partial}{\partial z} \left( K_m \frac{\partial w}{\partial z} \right) \\ - S_w(x, y, z). \end{aligned} \quad (1c)$$

$p'$  is the local pressure perturbation and  $K_m$  the local exchange coefficient. The Coriolis parameter  $f$  describes the rotation of the wind near ground compared to the geostrophic wind components  $u_g$  and  $v_g$ . The Coriolis parameter can be calculated as  $f = 2\Omega \sin \varphi$ , where  $\Omega = 7 \cdot 10^{-5} \text{s}^{-1}$  is the pulsance of the earths rotation and  $\varphi$  is the latitude of the models location. The Coriolis parameter is implemented in ENVI-met but is switched off by default.

$S_u, S_v$  and  $S_w$  are local source/ sink terms that model the wind drag of semi-permeable obstacles, i.e. vegetation. When air flows through a porous body a pressure gradient along the direction  $i$  of the wind component  $u_i$  ( $u_i = u, v, w$  with  $i = 1, 2, 3$ ) is generated. The influence of this pressure gradient on the wind can be describes as [Yamada, 1982]:

$$S_{u_i}(x, y, z) = \left. \frac{\partial p''}{\partial x_i} \right|_p = c_{d,p} LAD(x, y, z) u_i W(x, y, z). \quad (2)$$

$LAD$  is the leaf area density [ $\text{m}^2/\text{m}^3$ ],  $c_{d,p}$  the mechanical drag coefficient of the leaves and  $W(x, y, z)$  the mean wind speed in the grid cell:

$$W(x, y, z) = \sqrt{u^2(x, y, z) + v^2(x, y, z) + w^2(x, y, z)}. \quad (3)$$

The mechanical drag coefficient is set to  $c_{d,p} = 0.2$ .

For further simplification the Boussinesq-approximation is used to eliminate the density  $\rho$  from the Navier-Stokes equations which can then - using the Einstein summation - be written as:

$$\frac{\partial u}{\partial t} + u_i \frac{\partial u}{\partial x_i} = - \frac{\partial p'}{\partial x} + K_m \left( \frac{\partial^2 u}{\partial x_i^2} \right) + f(v - v_g) - S_u \quad (4a)$$

$$\frac{\partial v}{\partial t} + u_i \frac{\partial v}{\partial x_i} = - \frac{\partial p'}{\partial y} + K_m \left( \frac{\partial^2 v}{\partial x_i^2} \right) + f(u - u_g) - S_v \quad (4b)$$

$$\frac{\partial w}{\partial t} + u_i \frac{\partial w}{\partial x_i} = - \frac{\partial p'}{\partial z} + K_m \left( \frac{\partial^2 w}{\partial x_i^2} \right) + g \frac{\theta(z)}{\theta_{ref}(z)} - S_w \quad (4c)$$

Due to the air now being treated as an incompressible fluid an additional continuity equation has to be satisfied:

$$\frac{\partial u}{\partial x} + \frac{\partial v}{\partial y} + \frac{\partial w}{\partial z} = 0 \quad (5)$$

## 4.2. Temperature and humidity

The potential temperature  $\theta$  can be calculated by using the combined advection-diffusion equation:

$$\frac{\partial \theta}{\partial t} + u_i \frac{\partial \theta}{\partial x_i} = K_h \left( \frac{\partial^2 \theta}{\partial x_i^2} \right) + \frac{1}{c_p \rho} \frac{\partial R_{lw}}{\partial z} + Q_\theta. \quad (6)$$

$Q_\theta$  is a term that defines the heat exchange between air and vegetation and  $K_h$  is the turbulent exchange coefficient for heat. The term  $\frac{1}{c_p \rho} \frac{\partial R_{lw}}{\partial z}$  describes the change in air temperature due to divergence of the long wave radiation.

For the humidity the advection-diffusion equation can be written as:

$$\frac{\partial q}{\partial t} + u_i \frac{\partial q}{\partial x_i} = K_q \left( \frac{\partial^2 q}{\partial x_i^2} \right) + Q_q \quad (7)$$

$Q_q$  defines the exchange of humidity between air and vegetation and  $K_q$  is the turbulent exchange coefficient for humidity.

ENVI-met does not model the phase transformation between water and water vapour and vice versa. This means that the relative humidity is always below 100%.

## 4.3. Atmospheric turbulence

ENVI-met uses a 1.5 order turbulence closure model. This model is based on the work of Mellor and Yamada [Mellor and Yamada, 1974] [Mellor and Yamada, 1982] and adds two additional equations for turbulence ( $E$ ) and its dissipation ( $\epsilon$ ):

$$\frac{\partial E}{\partial t} + u_i \frac{\partial E}{\partial x_i} = K_E \left( \frac{\partial^2 E}{\partial x_i^2} \right) + Pr - Th + Q_E - \epsilon \quad (8)$$

$$\frac{\partial \epsilon}{\partial t} + u_i \frac{\partial \epsilon}{\partial x_i} = K_\epsilon \left( \frac{\partial^2 \epsilon}{\partial x_i^2} \right) + c_1 \frac{\epsilon}{E} Pr - c_3 \frac{\epsilon}{E} Th - c_2 \frac{\epsilon^2}{E} + Q_\epsilon \quad (9)$$

The constants  $c_1$ ,  $c_2$  and  $c_3$  are empiric constants. The default values used in ENVI-met are taken from Launder and Spalding [Launder and Spalding, 1974]:

$$c_1 = 1.44 \quad c_2 = 1.92 \quad c_3 = 1.44$$

However special flow situations can require a change in these values.

The terms  $Pr$  and  $Th$  denote the production and dissipation of turbulent energy caused by wind shearing ( $Pr$ ) and thermal stratification (buoyancy production) ( $Th$ ). They can be written as:

$$Pr = K_m \left( \frac{\partial u_i}{\partial x_j} \frac{\partial u_j}{\partial x_i} \right) \frac{\partial u_i}{\partial x_j} \quad (10)$$

$$Th = \frac{g}{\theta_{ref}(z)} K_h \frac{\partial \theta}{\partial z} \quad (11)$$

$\theta_{ref}(z)$  is the potential temperature at the inflow boundary in height  $z$ . Under stable conditions  $Th$  can be neglected.

The turbulence induced by vegetation  $Q_E$  and the accelerated cascade of turbulence energy from large scales to smaller ones near plant foliage  $Q_\epsilon$  can be summed up as [Liu, 1996] [Wilson, 1988]:

$$Q_E = c_{d,f}LAD(z) \cdot W^3 - 4c_{d,f}LAD(z) \cdot |W| \cdot E \quad (12)$$

$$Q_\epsilon = 1.5c_{d,f}LAD(z) \cdot W^3 - 6c_{d,f}LAD(z) \cdot |W| \cdot \epsilon. \quad (13)$$

The diffusion coefficients are then derived from the  $E - \epsilon$  field with the assumption of the isotropy of local turbulence:

$$K_m = c_\mu \frac{E^2}{\epsilon}$$

$$K_h = K_q = 1.35K_m$$

$$K_E = \frac{K_m}{\sigma_E}$$

$$K_\epsilon = \frac{K_m}{\sigma_\epsilon}$$

with  $c_\mu = 0.09$ ,  $\sigma_E = 1$  and  $\sigma_\epsilon = 1.3$ . These are also empiric constants that may require an adjustment in special flow conditions.

#### 4.4. Radiation

The calculation of the incoming shortwave and long wave fluxes is based on a two-stream approximation in combination with some empiric formula [Taesler and Anderson, 1984] [Gross, 1991].

The atmospheric radiation budget is defined by the absorption and emission coefficients of the different atmospheric layers. These coefficients depend on the optical thickness of the atmosphere, i.e. the number of aerosols and the amount of water vapour, carbon dioxide, ozone, and other greenhouse gases within the layer of atmosphere. For an accurate calculation of the radiative fluxes it would therefore be necessary to know the exact distribution of aerosols and greenhouse gases within the atmosphere and to account for their partly overlapping emission and absorption spectra. ENVI-met uses a much simpler approximation that only takes the water vapour into account.

In a model with  $N$  layers the incoming long wave radiation at a height  $z$  can be calculated as [Paltridge and Platt, 1976]:

$$Q_{lw}^\downarrow(z) = \sum_{n=1}^N \sigma T^4(n) [\epsilon_n(m + \Delta m) - \epsilon_n(m)]. \quad (15)$$

$m$  is the amount of water vapour between height  $z$  and the lower boundary of layer  $n$ ,  $m + \Delta m$  the amount of water vapour between height  $z$  and the upper boundary of layer  $n$ .  $\epsilon_n$  is the emissivity,  $T$  the absolute temperature of layer  $n$ . The calculation of  $\epsilon_n$  is

based on an empiric formula that requires the amount of water vapour as input [Kuhn, 1963] [Pielke, 1982].

The incoming shortwave radiation at the upper boundary of the model area is calculated by integrating the radiation intensity of the sun  $I_0$  from the wavelength  $\lambda = 0.29\mu\text{m}$  to  $\lambda = 4.0\mu\text{m}$ :

$$Q_{sw}^* = \int_{0.29}^{4.0} I_0(\lambda) \exp\{-\alpha_R(\lambda)m + \alpha_M(\lambda)m\} d\lambda \quad (16)$$

The optical air mass  $m$  depends on the sun height  $h$ :

$$m = \begin{cases} \frac{1}{\sin h} & \text{if } h > 10 \\ 1.22 \left( \frac{1.0144}{\sin(h+1.44)} - 0.49 \right) & \text{if } h \leq 10. \end{cases} \quad (17)$$

$\alpha_R(\lambda) = 0.00816 \cdot \lambda^{-4}$  and  $\alpha_M = \lambda^{-1.3} \beta_t r$  are the coefficients for Rayleigh and Mie scattering, with  $0.004 \leq \beta_t r \leq 1$  as the opacity coefficient.

The absolute amount of direct short-wave radiation  $R_{sw,dir}^0$  is given by:

$$Q_{sw,dir}^0 = Q_{sw}^* - Q_{sw,abs}. \quad (18)$$

$Q_{sw,abs}$  is the shortwave radiation that is absorbed by water vapour and it can be calculated as [Liliequist and Cehak, 2006]:

$$Q_{sw,abs} = 70 + 2.8 \cdot e_{2m} \cdot m. \quad (19)$$

$e_{2m}$  is the water vapour pressure in [hPa] in 2m above ground level.

The diffuse shortwave radiation for a cloudless sky depends on the incoming direct shortwave radiation and the sun height  $h$  [Brown and Islält, 1974]:

$$Q_{sw,dif}^0 = R_{sw,dir}^0 \sin h \left( \frac{\Upsilon(h)}{1 - \Upsilon(h)} \right) \quad (20)$$

with  $\Upsilon(h) = \frac{1}{1+8(\sin h)^{0.7}}$ .

If clouds are present the terms for the direct and diffuse radiation have to be adapted [Taesler and Anderson, 1984]:

$$Q_{sw,dir}^0(\text{clouds}) = Q_{sw,dir}^0 \left( 1 - \frac{N}{8} \right) \quad (21)$$

$$Q_{sw,dif}^0(\text{clouds}) = \left( \frac{Q_{sw,dir}^0 \sin h}{1 - \Upsilon(h)} \right) \left( \frac{a_s - 1}{a_s a_c - 1} \right) - Q_{sw,dir}^0(\text{clouds}) \sin h. \quad (22)$$

$N$  is the cloud cover in  $\frac{1}{8}$ ,  $a_c$  the albedo of the clouds and  $a_s$  the albedo of the soil.

Within the model area the radiation fluxes are strongly modified by (partial) shading from buildings and vegetation. This modification of the long wave and shortwave radiation fluxes is modeled via a number of coefficients  $\sigma_{\dots}$  that range between 0 (i.e. the radiation flux is completely blocked) to 1 (i.e. the radiation flux is not disturbed).

The sky view factor  $\sigma_{svf}$  is a measure for the amount of sky seen from the center of a grid cell:

$$\sigma_{svf} = \frac{1}{360} \sum_{\pi=0}^{360} \cos \omega(\pi) \quad (23)$$

where  $\omega$  denotes the maximum cutoff angle in spatial direction  $\pi$ .

Other coefficients describe the influence of vegetation on direct  $\sigma_{sw,dir}$  and diffuse  $\sigma_{sw,dif}$  shortwave radiation and on upward  $\sigma_{lw}^\uparrow$  and downward  $\sigma_{lw}^\downarrow$  long wave radiation:

$$\sigma_{sw,dir} = \exp(F \cdot LAI^*(z))$$

$$\sigma_{sw,dif} = \exp(F \cdot LAI(z, z_p))$$

$$\sigma_{lw}^\uparrow = \exp(F \cdot LAI(0, z))$$

$$\sigma_{lw}^\downarrow = \exp(F \cdot LAI(z, z_p)).$$

$LAI$  is the vertical leaf area index of the plant from level  $z$  up to the top of the plant  $z_p$  or down to the ground  $z = 0$ . For shortwave solar radiation  $LAI^*$  replaces  $LAI$ . For the calculation of  $LAI^*$  the angle of incidence of the incoming sun rays is taken into account.

The shortwave radiation budget can be summed up as:

$$Q_{sw}(z) = \sigma_{sw,dir}(z)Q_{sw,dir}^0 + \sigma_{sw,dif}(z)\sigma_{svf}(z)Q_{sw,dif}^0 + (1 - \sigma_{svf}(z))Q_{sw,dir}^0 \cdot \bar{a} \quad (25)$$

with  $Q_{sw,dir}^0$  as the direct and  $Q_{sw,dif}^0$  as the diffuse shortwave radiation at the top of the model area. The term  $\bar{a}$  denotes the average albedo of all walls within the model area.

The long wave radiation fluxes can be written as:

$$Q_{lw}^\downarrow(z) = \sigma_{lw}^\downarrow(z, z_p)Q_{lw}^{\downarrow,0} + (1 - \sigma_{lw}^\downarrow(0, z))\epsilon_f \sigma_B \bar{T}_{f+}^4 + (1 - \sigma_{svf}(z))Q_{lw}^{\leftrightarrow} \quad (26a)$$

$$Q_{lw}^\uparrow(z) = \sigma_{lw}^\uparrow(0, z)\epsilon_s \sigma_B T_0^4 + (1 - \sigma_{lw}^\uparrow(0, z))\epsilon_f \sigma_f \bar{T}_{f-}^4 \quad (26b)$$

$\bar{T}_{f-}^4$  and  $\bar{T}_{f+}^4$  are the average foliage temperature of the underlying, respectively overlying vegetation.  $\epsilon_s$  and  $\epsilon_f$  denote the emissivities of the surface and foliage.  $T_0$  is the surface temperature and  $R_{lw}^{\leftrightarrow}$  is the horizontal long wave radiation flux from surrounding walls.  $\sigma_B$  is the Stefan-Boltzmann constant:  $\sigma_B = 5.67 \cdot 10^{-8} W m^{-2} K^{-4}$ .

## 4.5. Soil model

The soil model calculates the temperature and humidity of the soil down to a depth of 1.75m. For greater depths the diurnal variations of temperature and humidity can be assumed negligible in their effect on the atmosphere - at least within the timescales usually simulated with ENVI-met ( $\leq 3$  days).

Each horizontal grid cell has a soil profile with 14 layers that differ in depth. The depth of the single layers increases from top to bottom: while the top layers have a thickness

of only 1cm, the lowest layer has a thickness of 50cm.

Within the soil model only vertical fluxes of temperature and humidity are calculated (1D model). The soil temperature  $T_s$  and the volumetric water content  $\eta$  are calculated as:

$$\frac{\partial T_s}{\partial t} = \kappa_s \frac{\partial^2 T_s}{\partial z^2} \quad (27)$$

$$\frac{\partial \eta}{\partial t} = D_\eta \frac{\partial^2 \eta}{\partial z^2} + \frac{\partial K_\eta}{\partial z} - S_\eta(z) \quad (28)$$

The thermal diffusivity  $\kappa_s$  is constant for impermeable soils and a function of soil moisture  $\eta$  for all other soils.

## 4.6. Vegetation model

The vegetation in ENVI-met interacts with the atmospheric model as well as with soil model and the radiation model.

Plants in ENVI-met 3.1 are modeled as vegetation columns. A database defines the height of the plant  $z_p$  and the leaf area Density  $LAD$  in ten layers. The height of each layer of the plant is defined as  $z_{pl} = \frac{z_p}{10}$ . The maximum depth of the roots  $-z_p$  and the root area density  $RAD$  are defined analogously.

The direct heat flux  $J_{f,h}$ , the evaporation flux  $J_{f,evap}$  and the transpiration flux  $J_{f,trans}$  that define the interactions between vegetation and atmosphere can be written as:

$$J_{f,h} = 1.1r_a^{-1}(T_f - T_a) \quad (29)$$

$$J_{f,evap} = r_a^{-1}\Delta q\delta_c f_w + r_a^{-1}(1 - \delta_c)\Delta q \quad (30)$$

$$J_{f,trans} = \delta_c(r_a + r_s)^{-1}(1 - f_w)\Delta q \quad (31)$$

$T_a$  is the air temperature,  $T_f$  the foliage temperature,  $q_a$  the specific humidity of the air and  $\Delta q$  is the humidity difference  $\Delta q = q^*T_a - q_a$ .  $q^*$  is the saturated value of  $q$  at the leaf surface.  $\delta_c$  defines whether evapotranspiration is possible ( $\delta_c = 1$ ) or not ( $\delta_c = 0$ ).  $r_a$  is the aerodynamic resistance which is a function of the leaf diameter  $D$  and the wind speed  $W$  [Braden, 1982]:

$$r_a = A\sqrt{\left(\frac{D}{W}\right)} \quad (32)$$

The parameter  $A$  depends on the type of plant: for conifers  $A$  is  $87s^{0.5}m^{-1}$ , for grass and deciduous trees  $A$  is  $200s^{0.5}m^{-1}$ .  $D$  is the average diameter of the leaf.

The most important factor regulating the evapotranspiration of plants are the so called stomata, little opening within the leaves that allow the exchange of gases between air and leaf. The stomatal resistance  $r_s$  is a measure for the degree to which the stomata are opened. The original method of calculating the stomatal resistance was based on the work of Deardoff [Deardoff, 1978] and calculates  $r_s$  as a function of shortwave radiation, soil water content in combination with the root area density and the general state of



the plant, i.e. whether the plant is in a growth phase or not. In ENVI-met 3.1 this model has been replaced by a more sophisticated  $A - g_s$  model based on the work of Jacobs [Jacobs, 1994]. The  $A - g_s$  uses the photosynthesis rate  $A_n$  in combination with the stomatal conductance  $g_s [mm s^{-1}]$  of a plant to calculate its evapotranspiration. The basic relation of the model can be summed up as [Bruse, 2004a]:

$$g_s = 1.6 \frac{A_n}{C_s - C_i} \quad (33)$$

with  $C_s$  and  $C_i$  as the  $CO_2$  concentrations at the surface and inside the leaf. The relation between stomatal resistance and stomatal conductance is:  $r_s = \frac{1}{g_s} \cdot 1000$ .

#### 4.7. Ground surfaces

For the calculation of the temperature  $T_0$  at the ground surface the energy balance at ground level has to be solved:

$$Q_{sw,net} + R_{lw,net}(T_0) - G(T_0) - H(T_0) - LE(T_0, q_0) = 0 \quad (34)$$

$Q_{sw,net}$  is the net shortwave radiation at the surface,  $Q_{lw,net}$  the net long wave radiation at the surface,  $G$  is the soil heat flux,  $H$  the sensible and  $LE$  the latent turbulent heat flux.

With  $R_{sw,dir}(z = 0)$  and  $Q_{sw,dif}(z = 0)$  as the direct and diffuse fraction of the shortwave radiation at the surface  $Q_{sw,net}$  can be calculated as:

$$Q_{sw,net} = [\cos \beta^* \cdot Q_{sw,dir}(z = 0)](1 - a_s) \quad (35)$$

$\beta^*$  is the angle between the direct solar radiation and the surface (Lambert's cosine law). The albedo  $a_s$  of impermeable surfaces is constant, for all other soils it is a function of the sun angle and the soil water content of the uppermost soil layer [Idso et al., 1975]. The long wave energy balance of the ground surface is split into two parts:

$$Q_{lw,net}(T_0) = \sigma_{svf} Q_{lw,net}^{free}(T_0) + (1 - \sigma_{svf}) Q_{lw,net}^{screened}(T_0) \quad (36)$$

$Q_{lw,net}^{sky}$  is the long wave radiation for the part of the sky with unobstructed view and  $Q_{lw,net}^{screened}$  the long wave radiation for the screened part, i.e. the parts where vegetation and buildings block the view.

$$Q_{lw,net}^{sky}(T_0) = \sigma_{lw}^{\downarrow}(0, z_p)(Q_{lw}^{\downarrow,0} - \varepsilon_s \sigma T_0^4) + (1 - \sigma_{lw}^{\downarrow}(0, z_p)) \frac{\varepsilon_v \varepsilon_s}{\varepsilon_v + \varepsilon_s - \varepsilon_v \varepsilon_s} (\sigma \bar{T}_v^4 - \sigma \bar{T}_0^4) \quad (37a)$$

$$Q_{lw,net}^{screened}(T_0) = \frac{\varepsilon_w \varepsilon_s}{\varepsilon_w + \varepsilon_s - \varepsilon_w \varepsilon_s} (\max(\sigma \bar{T}_w^4, \sigma \bar{T}_0^4) - \sigma \bar{T}_0^4) \quad (37b)$$

$\varepsilon_s$ ,  $\varepsilon_v$  and  $\varepsilon_w$  denote the emissivities of the surface, vegetation and walls. Analogously  $T_f$  is the surface temperature of the vegetation and  $T_w$  the surface temperature of the

walls.

The turbulent fluxes  $H$  and  $LE$  are a function of the turbulent exchange coefficients  $K_h$  and  $K_q$  and the temperature, respectively humidity of the ground surface and the lowest atmospheric grid cell:

$$H(T_0) = \rho c_p K_h^0 \frac{T_0 - \theta_{k=1}}{0.5 \Delta z_{k=1}} \quad (38)$$

$$LE(T_0, q_0) = \rho L(T_0) K_q^0 \frac{q_0 - q_{k=1}}{0.5 \Delta z_{k=1}} \quad (39)$$

with  $L(T_0) = (2.501 - 0.00237(T_0 - 273.15)) \cdot 10^6$ .

The soil heat flux  $G$  can be calculated as:

$$G(T_0) = \lambda_s(k=1) \frac{T_0 - T_{k=-1}}{0.5 \Delta z_{k=-1}} \quad (40)$$

#### 4.8. Building surfaces

The calculation of the energy balance of facades and roofs is described in detail in part III of this work.

#### 4.9. Gases and particles

ENVI-met can simulate the dispersion of gases and fine particles, i.e. aerosols, within the atmosphere. In Version 3.1 the diffusion of only one sort of gas or particle can be simulated at the same time.

For the calculation of the dispersion the standard advection-diffusion equation is used [Bruse, 2007]:

$$\frac{\partial \chi}{\partial t} + u \frac{\partial \chi}{\partial x} + v \frac{\partial \chi}{\partial y} + w \frac{\partial \chi}{\partial z} = \frac{\partial}{\partial x} (K_x \frac{\partial \chi}{\partial x}) + \frac{\partial}{\partial y} (K_y \frac{\partial \chi}{\partial y}) + \frac{\partial}{\partial z} (K_z \frac{\partial \chi}{\partial z}) + Q_\chi(x, y, z) + S_\chi(x, y, z) \quad (41)$$

where  $\chi$  denotes the gaseous or particulate atmospheric component under investigation and  $Q_\chi$  and  $S_\chi$  describe its source and sink terms (sedimentation or chemical transformation). The unit of  $\chi$  is  $[mgkg^{-1}]$ .

ENVI-met allows the user to place different types of gas/ particle sources throughout the model area. The four basic types of sources are:

- point sources:  $q_p [mgs^{-1}]$
- line sources:  $q_l [mgs^{-1}m^{-1}]$
- area sources:  $q_a [mgs^{-1}m^{-2}]$
- volume sources:  $q_v [mgs^{-1}m^{-3}]$

With the grid cell dimensions  $\Delta x$ ,  $\Delta y$  and  $\Delta z$  all four kinds of sources can be transformed into  $q^*$  [ $mg s^{-1}$ ]:

$$q^* = q_p \quad (42)$$

$$= q_l \cdot \Delta x, y \quad (43)$$

$$= q_a \cdot \Delta x \Delta y \quad (44)$$

$$= q_v \cdot \Delta x \Delta y \Delta z \quad (45)$$

The source term  $Q_\chi$  can then be written as:

$$Q_\chi = \frac{q^*}{\Delta x \Delta y \Delta z \cdot \rho} \quad (46)$$

The sources in ENVI-met can have a diurnal variation. The database features 24 entries, each corresponding to an emission rate for each of the 24 hours of the day. The emission rates for points in time in between are linearly interpolated.

The sink term  $S_\chi$  consists of three separate components:

- gravitational settling and deposition at surfaces ( $\chi^\downarrow$ )
- deposition at leaf surfaces ( $\chi_{plants}$ )
- chemical transformations: the concentration of components A and B decreases, the concentration of component AB increases

Gravitational settling only applies to particles, not to gaseous components. The chemical transformation only occurs for reactive gases. Furthermore this transformation needs a reaction partner. In version 3.1 of ENVI-met this chemical transformation is not included. Therefore only inert gases can be simulated.

At the Flemish Institute for Technological Research (VITO) a version of ENVI-met has been developed that allows the simulation of more than one gaseous atmospheric component and that also features chemical transformations [De Maerschalck et al., 2008].

## 4.10. Initialization & boundary conditions

A description of the initialization process of the model and its boundary conditions can be found in section 3 of part IV.

## 4.11. Thermal comfort indices

While the calculation of the different atmospheric parameters is relatively straightforward the assessment of the influence of these parameters on human perception of the current meteorological conditions is much more complicated.

Whereas most people - and generations of weather forecasters - consider the air temperature to be the most important indicator of human thermal comfort it is also strongly

influenced by three other atmospheric variables, adding up to the following four meteorological parameters:

- air temperature  $T_a$
- wind speed  $\mathbf{u}$
- air humidity  $q_a$
- radiant temperature (= radiation budget)  $T_{mrt}$

The connection between these four parameters and human thermal comfort is neither linear for one variable (e.g. an increase of wind speed by  $2\text{m.s}^{-1}$  does not necessarily have double the impact on the human perception of thermal comfort as an increase of  $1\text{m.s}^{-1}$ ) nor for the interdependence of the different variables (i.e. a change in one of the variables does not always have the same effect on human thermal comfort but rather depends on the values of the other three variables).

Furthermore the human perception of the climate conditions not only depends on atmospheric conditions but also on the metabolism (gender, size, weight, age, fitness level, work load) and clothing (insulation, albedo) of a person. To complicate matters even further the perception of human thermal comfort might also depend on cultural and psychological factors.

There exist several models that try to assess human thermal comfort by calculating the energy balance of a human person in specific meteorological conditions. One of the oldest of these models, still widely used by bio-meteorologists, is the so called “predicted mean vote” (PMV) model by Fanger [FANGER, 1972]. PMV predicts the mean judgment of a large group of people on the ASHRAE thermal sensation scale, which runs from -3 (very cold) to +3 (hot). PMV had originally been developed for the assessment of indoor climate but has also successfully been used for the assessment of outdoor locations.

Many more modern human thermal comfort indices exist. The biggest difference between these indices and PMV is the level of detail used for calculating the energy balance of the human body. All these biometeorological indices assume that the person for whom the index is calculated is standing in place until his or her body has adapted to the surrounding atmospheric conditions. In an urban environment however this static treatment is often inaccurate because the microclimatic atmospheric conditions - especially wind and radiant temperature - can vary drastically within the space of a few meters.

At the moment ENVI-met supports the calculation of PMV and the more modern “physiologically equivalent temperature” (PET) [Höppe, 1999] while the newest human thermal comfort index, the “universal thermal climate index” (UTCI) [Win, 2001] has not yet been implemented.

The calculation of all of these biometeorological indices does not require any feedback from ENVI-met but just the output results for air temperature, wind speed, air humidity and radiant temperature. In ENVI-met 3.1 the calculation of these thermal comfort indices is therefore no longer implemented directly into the simulation software but rather into an additional software that can read the output files of ENVI-met. This approach also offers the possibility to recalculate the human thermal comfort index with different

personal-related parameters (e.g. weight, clothing) or update the calculations without having to run another complete simulation of the model area in ENVI-met .

#### 4.11.1. Calculation of the mean radiant temperature in ENVI-met

ENVI-met calculates the mean radiant temperature  $T_{mrt}$  for a cylindric shaped body:

$$T_{mrt} = \left( \frac{1}{\sigma} (Q_{lw,in} + \frac{ak}{\varepsilon} * (Q_{sw-diff,in} + Q_{sw-dir,in})) \right)^{0.25}$$

where the emission coefficient of the human body ( $\varepsilon$ ) is set to 0.97 and  $ak$  as the absorption coefficient of the human body for short wave radiation is set to 0.7.  $\sigma$  is the Stefan-Boltzmann constant.

The incoming long wave radiation  $Q_{lw,in}$  is assumed to come to 50% from the sky, buildings and vegetation and to 50% from the ground surface:

$$Q_{lw,in} = 0.5 * (vf_{veg} \bar{\varepsilon}_{veg} \sigma \bar{T}_{veg}^4 + vf_{bldg} \bar{\varepsilon}_{bldg} \sigma \bar{T}_{bldg}^4 + vf_{sky} Q_{lw,sky} + vf_{bldg} (1 - \bar{\sigma}_{bldg}) Q_{lw,sky}) + 0.5 * (\sigma \varepsilon_{ground} T_{ground}^4). \quad (47)$$

The view factors  $vf$  give the percentage of vegetation/ buildings/ sky that can be seen from the specific grid point. The physical correct approach would be to calculate the long wave radiation fluxes based on the emissivity and temperature of the elements within view. This would however require considerable amounts of CPU time and RAM. Therefore the average emissivity  $\bar{\varepsilon}$  and temperature  $\bar{T}$  of all plants/ building surfaces within the model area are used instead. The incoming long wave radiation from the sky  $Q_{lw,sky}$  is calculated based on the air temperature, air humidity and some empirical parameters ([Oke, 1987]). For long wave radiation coming from the ground only the emissivity and surface temperature of the grid corresponding grid cell are taken into account.

The diffuse incoming short wave radiation  $Q_{sw-dir,in}$  is calculated accordingly:

$$Q_{sw-dir,in} = 0.5 * (vf_{bldg} \bar{r}_{bldg} Q_{sw-dir,sky} + vf_{sky} Q_{sw-diff,sky}) + 0.5 * (rf_{ground} Q_{sw,ground}) \quad (48)$$

With  $rf$  as the reflectivity and  $Q_{sw,ground}$  as the overall shortwave radiation at the ground surface of the corresponding grid cell.

The incoming direct short wave radiation  $Q_{sw-dir,in}$  is calculated as the direct short wave radiation within the grid cell multiplied with an projection factor  $pf$ :  $Q_{sw-dir,in} = pf * Q_{sw-dir}$ . This projection factor depends on the azimuth angle of the sun  $\Phi$ :

$$pf = 0.42 * \cos\Phi + 0.043 * \sin\Phi. \quad (49)$$

#### 4.11.2. BOTworld - calculation of a dynamic comfort index

In addition to the calculation of static human thermal comfort indices like PMV or PET ENVI-met also allows the non-static biometeorological assessment of a model area via the multi-agent simulation BOTworld ([www.botworld.info](http://www.botworld.info)). In BOTworld, simulated agents called bots move through the model area on user-definable paths and assess the model area depending on their actual thermal sensation which is - in contrast to PET or PMV - not calculated by recalculating the equations until an equilibrium is reached (i.e. the body has adjusted to the atmospheric conditions). Instead the bots walk through the model area and keep their thermal history. With this method a much more realistic assessment of the thermal performance of urban quarters is possible.

### 5. Numerical solution techniques

The differential equations are solved by using the finite difference method and are solved forward in time:

$$\frac{\partial \phi}{\partial t} \rightarrow \frac{\phi^{n+1} - \phi^n}{\Delta t}$$

with  $\Delta t$  as the time step, i.e. the interval at which the equations are solved and  $\phi^n$  the (known) variable at the previous time step and  $\phi^{n+1}$  the (searched for) variable at the next time step.

For the solution of the combined advection-diffusion equations the so called Alternating Direction Implicit (ADI) method is used. Further information on this method can be found in section 5.2 of part IV of this work.

For the calculation of the wind field the dynamic pressure  $p'$  is removed from the equations (1a), (1b) and (1c) and calculated separately, using the Poisson equation

$$\nabla^2 p' = \frac{\rho_0}{\Delta t} \nabla \mathbf{u}^{aux} \quad (50)$$

with  $\mathbf{u}^{aux}$  as the preliminary wind field which was calculated without any pressure correction. For the iterative calculation of the Poisson equation the Simultaneous Over-Relaxation (SOR) method is used ([Patrinos and Kistler, 1977]).

The new wind field  $\mathbf{u}^*$  can then be calculated as:

$$\mathbf{u}^* = \mathbf{u}^{aux} - \frac{\delta t}{\rho_0} \nabla p'. \quad (51)$$

In order to get a numerically stable calculation of the turbulence and its dissipation the size of the time step between calculations has to be chosen carefully. The maximum allowed time step depends on the velocity of the wind ( $u, v, w$ ) and the size of the grid cells ( $\Delta x, \Delta y, \Delta z$ ) and can be calculated as:

$$\Delta t_{max} = \frac{0.8}{|u/\Delta x|_{max} + |v/\Delta y|_{max} + |w/\Delta z|_{max}}$$

Experience has shown that this criterion is not sufficient as - in some conditions - it allows time steps that are too large and lead to numerical instability. Therefore an arbitrary - maximum value is defined:  $\Delta t = 0.3$ .

## 6. Shortcomings of ENVI-met

ENVI-met is continually being updated and new features are introduced regularly. However ENVI-met is far from being a perfect simulation of reality and has some (major) limitations.

The following list gives a short overview on the most prominent shortcomings of ENVI-met:

- **Turbulence:** The standard  $k - \epsilon$  closure used by ENVI-met is known to have a tendency to overestimate the turbulent production  $k$  in areas with a high acceleration or deceleration, such as e.g. the flow around a building. This behaviour can often be found in simulations with ENVI-met.

There exist several modifications of the  $k - \epsilon$  closure which are supposed to solve this problem or at least mitigate it. The modification that seems to be most often used and has been found to produce the best results ([Lopez, 2002]) is the Kato-Launder modification [Kato and Launder, 1993]. This modification has also been tested in ENVI-met but is not used as it caused only slightly lower values for  $k$  near stagnation points but at the same time also made the simulations more prone to numerical instabilities.

Other methods for the closure of the turbulent kinetic energy like Direct Numerical Simulation (DNS) or Large Eddy Simulation would require a complete reprogramming of ENVI-met and are therefore not applicable to ENVI-met in the foreseeable future.

- **Radiation:** the radiative fluxes within the model area are not calculated accurately:
  - the scattering of the upward and downward diffuse radiation is considered to be isotropic.
  - the diffuse short wave radiation is not influenced by plants. This means that neither short wave diffuse radiation is absorbed when passing through vegetation, nor is diffuse short wave radiation created when direct short wave radiation passes through plants (i.e. no scattering of direct short wave radiation).
  - the short wave radiation scattered upwards by the ground and vegetation is not taken into account.
  - the part of the incoming long wave radiation which is emitted by nearby plants and surfaces is not calculated based on the temperature of the single surfaces and leaves within the field of view but rather on an average temperature. Thus the long wave radiation budget within areas with colder surfaces (as e.g. a small inner courtyard) is overestimated while it is underestimated in the vicinity of warmer surfaces.
- **Soil model:** at the moment there is no way to simulate the irrigation of the soil/plants.

- Fair weather model: ENVI-met can neither simulate precipitation nor temperatures below the freezing point.

The effect of these shortcomings on the results of simulations strongly depend on the model setup. For example in a simulation of soybean crop the overall results of the radiative fluxes calculated by ENVI-met have shown to be in reasonable accordance with the output of other, validated, radiative models [Samaali et al., 2007].

In any case the user has to be aware of the limitations of ENVI-met and should have at least a limited background knowledge of atmospheric physics in order to be able to assess the quality of a simulation.

## 7. Conclusion

With its different sub-models that simulate every aspect of urban climate ENVI-met might be called the Swiss army knife of urban microclimate simulations. The huge number of users and the variety of projects ENVI-met is used for bear witness to this claim. To our knowledge there is currently no other freely available microclimate simulation with the same functional range and accuracy as ENVI-met.

Nonetheless ENVI-met still has room for improvement and might not be the perfect tool for the investigation of every problem of urban microclimate. In particular users who are only interested in one specific element of urban microclimate can almost always find another software that delivers the desired results faster and possibly even more accurately: e.g. someone interested in only the wind-induced flow around buildings can easily achieve faster results with a higher spatial resolution by using a computational fluid dynamics (CFD) software.



## References

- H. Braden. Simulationsmodell für den wasser- energie- und stoffhaushalt in pflanzenbeständen. *Rep. Inst. Meteorol. Uni. Hannover*, 23, 1982.
- G. Brown and E. Islält. Solar irradiation and sun shading devices. In *Report R19:1974*. Nat. Swedish Council for building Research, Stockholm, 1974.
- M. Bruse. Envi-met implementation of the  $a - g_s$  model to calculate the stomata conductance (working paper). Retrieved 16.03.2011, 2004a. URL [http://envi-met.com/documents/new\\\_a\\\_gs.pdf](http://envi-met.com/documents/new\_a\_gs.pdf).
- M. Bruse. Bleeding edge: The most-recent doc you can have. Retrieved 16.03.2011, 2004b. URL <http://envi-met.com/documents/Envimet30.PDF>.
- M. Bruse. Particle filtering capacity of urban vegetation: A microscale numerical approach. In W. Endlicher, editor, *Tagungsband zum Workshop über den wissenschaftlichen Erkenntnisstand über das Feinstaubfilterungspotenzial (qualitativ und quantitativ) von Pflanzen am 1. Juni 2007 in Berlin/Adlershof (=Berliner Geographische Arbeiten 109)*, pages 61–70, 2007.
- M. Bruse and H. Fler. Simulating surface-plant-air interactions inside urban environments with a three dimensional numerical model. *Environmental Modelling & Software*, 13:373–384, 1998.
- B. De Maerschallck, S. Janssen, C. Mensink, A. van den Burg, and P. Fortuin. Cfd simulations of the impact of a line vegetation element along a motorway on local air quality. *Croatian meteorological journal*, 43:339–344, 2008.
- J. Deardoff. Efficient prediction of ground surface temperature and moisture with inclusion of a layer of vegetation. *J. Geophys. Research*, 83:1889–1903, 1978.
- P. O. FANGER. *Thermal comfort. Analysis and applications in environmental engineering*. McGraw Hill, New York, 1972.
- G. Gross. Anwendungsmöglichkeiten mesoskaliger simulationsmodelle dargestellt am beispiel darmstadt: Teil 1: Wind- und temperaturfelder. *Meteorol. Rundschau*, 43: 97–112, 1991.
- P. Höppe. The physiological equivalent temperature - a universal index for the biometeorological assessment of the thermal environment. *Int. J. Biometeorol*, 42:71–75, 1999.
- S. Idso, Jackson R., B. Kimball, and Nakagama F. The dependence of bare soil albedo on soil water content. *J. Appl. Met.*, 14:109–113, 1975.
- C. Jacobs. *Direct impact of atmospheric CO<sub>2</sub> enrichment on regional transpiration*. PhD thesis, Wageningen Agricultural University, 1994.

- M. Kato and B. Launder. The modeling of turbulent flow around stationary and vibrating square cylinders. *Proceedings of the 9th Symposium on Turbulent Shear Flows*, pages 10.4.1–10.4.6, 1993.
- P. Kuhn. Radiometer observations of infrared flux emissivity of water vapour. *J. Appl. Meteorol.*, 2:368–378, 1963.
- B. Launder and D.B. Spalding. The numerical computation of turbulent flow. *Computer Methods in Appl. Mechanics and Engineering*, 3:269–289, 1974.
- G. Liljequist and K. Cihak. *Allgemeine Meteorologie*. Springer, Berlin, 2006. ISBN 3540415653.
- J. Liu.  $e - \epsilon$  modelling of turbulent air flow downwind of a model forest edge. *Boundary Layer Meteorology*, 77:21–44, 1996.
- S. Lopez. *Numerische Modellierung turbulenter Umströmung von Gebäuden*. PhD thesis, Alfred-Wegener-institut für Polar- und Meeresforschung, Bremerhaven, 01 2002. URL <http://epic.awi.de/Publications/10423.pdf>.
- G.L. Mellor and T. Yamada. A hierarchy of turbulence closure models for planetary boundary layers. *Journal for Atmospheric Science*, 31:1791–1806, 1974.
- G.L. Mellor and T. Yamada. Development of a turbulence closure model for geophysical fluid problems. *Rev. Geophys.*, 20:851–875, 1982.
- T. Oke. *Boundary Layer Climates*. Halsted press, New York, 1987.
- G. Paltridge and C. Platt. *Radiative processes in Meteorology and Climatology*. Elsevier, New York, 1976. ISBN 044414444.
- A. Patrinos and A. Kistler. A numerical study of the chicago lake breeze. *Boundary layer meteorology*, 12:93–123, 1977.
- R.A. Pielke. *Mesoscale Meteorological Modelling*. Academic Press, New York, 1982. ISBN 9780125547666.
- M. Samaali, D. Courault, M. Bruse, A. Olioso, and R. Ocelli. Analysis of a 3d boundary layer model at local scale: Validation on soybean surface radiative measurements. *Atmospheric Research*, 85(2):183 – 198, 2007.
- R. Taesler and C. Anderson. A method for solar radiation computations using routine meteorological observations. *Energy and Buildings*, 7:341–352, 1984.
- J.D. Wilson. A second order closure model for flow through vegetation. *Boundary Layer Meteorology*, 70:371–392, 1988.
- Looking for a Universal Thermal Climate Index UTCI for Outdoor Applications*, April 5-8 2001. Windsor-Conference on Thermal Standards. URL [http://www.utci.org/isb/documents/windsor\\_vers04.pdf](http://www.utci.org/isb/documents/windsor_vers04.pdf).

T. Yamada. A numerical study of turbulent airflow in and above a forest canopy. *J. Meteorolog. Soc. Japan*, 60:439–454, 1982.



## Part III.

# Introducing a prognostic 3-node wall and roof model in the micro climate simulation ENVI-met

## 1. Summary

This chapter deals with the way ENVI-met calculates the surface temperature of facades. In ENVI-met 3.1 a simple, physically incorrect steady state model is used to calculate the temperature of wall and roof elements (that all have the same physical properties within the whole model area). In this chapter the integration of a more accurate transient state multi-node facade model into ENVI-met is discussed and the output of the new model is compared to actual measurements. The Results of this comparison show a good accordance between measurements and simulation.

## 2. Introduction

One of the main fields of application of a microclimate simulation like ENVI-met is the analysis of the influence of buildings on the urban microclimate (e.g.[Ali-Toudert and Mayer, 2004]). The size and shape of buildings influences the wind flow and solar access within the streets and thereby greatly influence human thermal comfort on street level. But the interaction between buildings and the atmosphere is not limited to the wind field and shading: the color and texture of the buildings surfaces define the radiative budget within their vicinity. The structure and materials of the facades determine how much heat can be stored within the walls and how well heat is transferred between the inside of a building and the atmosphere on the outside. The combination of all physical properties defines the surface temperature of the facade, which in turn influences the air temperature.

But not only urban planners looking at the microclimate would benefit from an accurate modeling of the energy exchange between facades and the atmosphere: it also helps architects and building engineers to better asses the amount of energy a building needs for cooling and heating and to monitor the feedback between the building and its vicinity.

In order to get a realistic simulation of urban climate it is therefore necessary to use a detailed model of the energy balance of walls and roofs - something not implemented in ENVI-met 3.1.

The following chapter describes how the limitations of the simulation of the energy balance of a wall or roof in prior versions of ENVI-met are overcome by the introduction of

a prognostic 3-node facade model in ENVI-met 4.0 and how the ENVI-met editor had to be modified in order to allow the user to take advantage of this new feature by creating more detailed model areas. In order to show the performance of the new 3-node facade model the output of a simulation is compared to measurements of roof surface temperatures taken at the Fraunhofer Institut for Building Physics in Holzkirchen, Southern Germany.

### 3. Physics

#### 3.1. The original estimation of the facade temperature

In versions prior to ENVI-met 4.0 the calculation of the outside wall/roof surface temperature is based on a simple steady-state energy balance. Parameters taken into account are the general thermal properties of the facade element (albedo, emissivity and U-value) in addition to the sensible heat transfer between the atmosphere and the facade and the heat conduction through the wall material. The general properties of the facades are identical for all wall and roof elements within the model domain. This means that there is no possibility to assign individual values to a single wall or roof element.

The steady-state energy balance of a wall/roof element is given by

$$Q_{sw,net}^{abs} + Q_{lw,net}^{abs} - \varepsilon_f \sigma T_w^4 - c_p \rho_w K_h^w \frac{T_w - T_{w+1}}{Dx} - \frac{\lambda_w}{d(T_w - T_{w,i})} = 0 \quad (1)$$

with  $Q_{sw,net}^{abs}$  and  $Q_{lw,net}^{abs}$  being the absorbed incoming shortwave and long wave radiation [ $Wm^{-2}$ ],  $\varepsilon_f$  the emissivity [%] of the facade,  $\sigma$  the Stefan-Boltzman constant,  $T_w$  the temperature [ $K$ ] of the facade,  $c_p$  the specific heat capacity of air at constant pressure ( $1200[J(kgK)^{-1}]$ ),  $\rho_w$  the density [ $kgm^{-3}$ ] of the facade,  $K_h^w$  the heat exchange coefficient [ $m^2s^{-1}$ ] at the surface of the wall/roof,  $T_{w+1}$  the air temperature [ $K$ ] at the grid cell next to the facade,  $Dx$  the distance [ $m$ ] between the facade and the centre of the next grid cell,  $\lambda_w$  the heat transmission coefficient [ $W(m^2K)^{-1}$ ] of the facade and  $T_{w,i}$  the temperature [ $K$ ] of the inner surface of the wall.

The heat exchange between the outer and the inner side of the wall is driven by the heat transfer coefficient  $\lambda_w$ .  $\lambda_w$  is not exactly equal to the U-value of the wall which can often be found in literature. The U-value describes the heat exchange between the inner and the outer air and hence implicitly also includes the heat transfer resistance between the surface and the adjacent inner and outer air layer.

The indoor temperature is set to a constant value and the inner wall is assumed to have the same temperature as the indoor air. Consequently, the heat exchange depends only on the temperature gradient between the outer and the inner surface of the wall or roof element.

In order to get more realistic temperatures of the facade, albeit the fact that heat storage within the wall is completely neglected, the absorbed incoming shortwave radiation  $Q_{sw,net}^{abs}$  for walls is set to half of its actual value. For roofs, which are assumed to

be much thinner and to therefore have a much lower heat storage capacity than walls,  $Q_{sw,net}^{abs}$  is left untouched.

The absorbed long wave radiation  $Q_{lw,net}^{abs}$  for walls is calculated as

$$Q_{lw,net}^{abs} = \varepsilon_f \left( (1 - svf) \left( \frac{1}{3} Q_{lw,ground} + \frac{2}{3} Q_{lw,buildings} \right) + svf \left( \frac{1}{2} Q_{lw,sky} + \frac{1}{2} Q_{lw,ground} \right) \right) \quad (2)$$

and for roofs as

$$Q_{lw,net}^{abs} = \varepsilon_f \left( (1 - svf) Q_{lw,buildings} + svf Q_{lw,sky} \right) \quad (3)$$

$svf$  is the sky view factor, which is the fraction of the open sky that can be seen from the center of the grid cell,  $Q_{lw,ground}$  the long wave radiation emitted by the ground,  $Q_{lw,buildings}$  the long wave radiation emitted by other buildings and  $Q_{lw,sky}$  the long wave radiation coming from the atmosphere.

For the calculation of the long wave radiation emitted from the surfaces of ground and buildings, the average of all ground/ facade temperatures within the model area are taken:  $Q_{lw,ground} = \varepsilon_g \sigma \overline{T_g^4}$ , respectively  $Q_{lw,buildings} = \varepsilon_f \sigma \overline{T_f^4}$ . The long wave radiation coming from the atmosphere ( $Q_{lw,sky}$ ) is calculated based on the air temperature, air humidity and some empirical parameters.

As one can easily see this approach has several shortcomings. The main problem of this approach clearly is the lack of any heat storage within the wall or roof. This lack of heat storage has two consequences:

- when the wall/roof element is exposed to the sun (i.e. direct short wave radiation) the increase in wall/roof temperature is strongly overestimated
- once the wall/roof element is no longer in the sun the temperature of the facade immediately steeply declines. The release of energy from the facade element to the atmosphere during the night - one of the characteristics of the urban heat island - can therefore not be simulated.

The first consequence is not solved but at least mitigated by using only 50% of the incoming shortwave solar radiation  $Q_{sw,net}^{abs}$  within the calculation.

### 3.2. The new 3-node model

The new calculation of the surface temperature of walls and roofs is based on a multiple-node transient state model motivated by the work of Terjung, and O'Rourke [Terjung and O'Rourke, 1980]. In their work Terjung and O'Rourke find the results of the transient state model to be more realistic than those of an alternatively proposed steady-state model but nevertheless conclude that the use of steady-state models for the calculation of wall/roof surface temperatures "appears justified as a reasonable approximation of

urban surface temperatures (reradiation) and convection patterns”. This conclusion was mainly influenced by the fact that the transient state model took considerably longer to calculate than the steady state model used in their study. More than 30 years later however the computing power has increased thus far that this reasoning is no longer valid and the transient state model for the calculation of wall/roof temperatures can be used in microclimate simulations like ENVI-met without noticeably prolonging the total simulation time.

The new transient state model can use an infinite number of nodes within the wall. For a first implementation and a proof of concept only three nodes, i.e. one at the outside, one in the middle and one on the inside of the wall (see fig. 1) were implemented. More nodes can and will be implemented in later versions of ENVI-met.

The physical properties of the wall/roof included in the calculation of the proposed transient state model are: reflectivity, absorption, transmission, emissivity, heat transfer coefficient, specific heat capacity and the thickness of the wall.

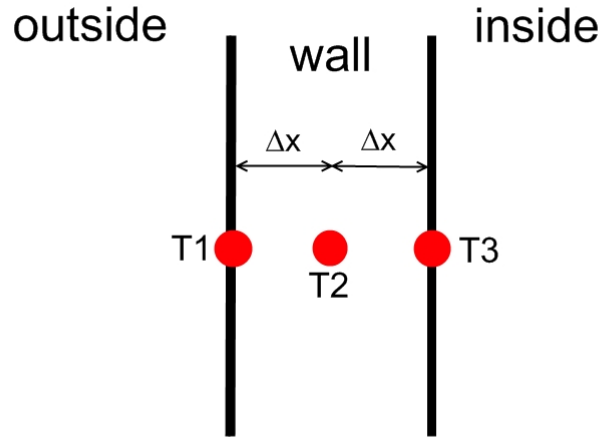


Figure 1: Schematic of the new 3-node model

The energy balance of the outer facade surface node (T1) can be written as

$$Q_{sw,net}^{abs} + Q_{lw,net}^{abs} - \varepsilon\sigma T_1^{*4} + h_{c,0}(T_{air} - T_1^*) + \frac{\lambda}{\Delta x}(T_2^* - T_1^*) = \frac{c_{wall}\rho_w\Delta x}{2\Delta t}(T_1^* - T_1) \quad (4)$$

with  $h_{c,0}$  being the heat convection coefficient for the outside wall [ $Wm^{-2}K^{-1}$ ],  $\lambda$  the heat transfer coefficient [ $W(Km)^{-1}$ ],  $\Delta x$  the distance between two nodes [ $m$ ],  $c_{wall}$  heat capacity of the wall [ $Jkg^{-1}K^{-1}$ ],  $T_n^*$  the temperature [ $K$ ] at node  $n$  at present ( $T_n$ ) or



future ( $T_n^*$ ) time step.

The heat convection coefficient  $h_{c,0}$  is calculated according to German DIN 6946 [DIN, 2005] as  $h_{c,0} = 4 + 4v$  with  $v$  being the wind speed [ $ms^{-1}$ ] in front of the wall/roof element.

With the Fourier Equation

$$\frac{\delta T}{\delta t} = \frac{\lambda}{c_{wall}\rho_w} \frac{\delta^2 T}{\delta x^2} \quad (5)$$

the heat fluxes at the node  $T_2$  located in the center of the wall can be summed up as

$$(P + 2)T_2^* - T_3^* = PT_2 + T_1^* \quad (6)$$

with  $P = \frac{\Delta x^2 c_{wall}\rho_w}{\lambda\Delta t}$ . For the node T3 at the inside of the wall the energy balance sums up to

$$-T_2^* + \left(\frac{P}{2} + \frac{h_c\Delta x}{\lambda} + 1\right)T_3^* = \frac{P}{2}T_3 + \frac{h_{c,i}\Delta x}{\lambda}T_i \quad (7)$$

with  $T_i$  being the temperature of the air inside the building and  $h_{c,i}$  as the heat convection coefficient at the inside which is set to  $7.7Wm^{-2}K^{-1}$  [DIN, 2005].

Equation 7 can be written as:

$$T_3^* = \left(T_2^* + \frac{P}{2}T_3 + \frac{h_{c,i}\Delta x}{\lambda}T_i\right)R \quad (8)$$

with  $R = \left(\frac{P}{2} + \frac{h_c\Delta x}{\lambda} + 1\right)^{-1}$ .

Equation 8 can then be inserted into equation 6:

$$T_2^* = \left(PT_2 + T_1^* + \frac{P}{2}T_3R + \frac{h_{c,i}\Delta x}{\lambda}T_iR\right)\frac{1}{P + 2 - R} \quad (9)$$

And finally equation 9 is inserted into equation 4:

$$\begin{aligned} \varepsilon\sigma T_1^{*4} + T_1^* \left( h_{c,0} + \frac{\lambda}{\Delta x} \left( 1 - \frac{1}{P + 2 - R} \right) + \frac{c_{wall}\rho_w\Delta x}{2\Delta t} \right) \\ = Q_{sw,net}^{abs} + Q_{lw,net}^{abs} + h_{c,0}T_{air} + \frac{c_{wall}\rho_w\Delta x}{2\Delta t}T_1 \\ + \frac{\lambda}{\Delta x(P + 2 - R)} \left( PT_2 + \frac{P}{2}T_3R + \frac{h_{c,i}\Delta x}{\lambda}T_iR \right) \end{aligned} \quad (10)$$

Equation 10 is then solved by applying the Newton's method.  $T_2^*$  and  $T_3^*$  can then directly be calculated via equations 9 and 8.

### 3.3. Estimate of absorbed long wave radiation

For the calculation of the absorbed long wave radiation  $Q_{lw,net}^{abs}$  separate view factors for each wall/roof element are used in the new approach. These view factors contain detailed information about the fraction of ground, sky, buildings and vegetation within

the field of view of the facade. Using these new view factors, the long wave radiation absorbed by a wall/roof element can be written as

$$Q_{lw,net}^{abs} = \epsilon_f (fvf_{ground} Q_{lw,ground} + fvf_{buildings} Q_{lw,buildings} + fvf_{sky} Q_{lw,sky} + fvf_{veg} Q_{lw,veg}) \quad (11)$$

The wall/roof view factors for soil ( $fvf_{ground}$ ), buildings ( $fvf_{buildings}$ ), sky ( $fvf_{sky}$ ) and vegetation ( $fvf_{veg}$ ) are calculated at the beginning of the simulation by the use of a ray tracing algorithm. This algorithm checks for every grid cell which elements can be seen from the center of the grid cell. The step width of the angles at which the tracing rays are emitted from the facade is  $10^\circ$  in the horizontal as well as the vertical direction. All in all  $36 \times 18$  rays are emitted and traced from each grid cell. E.g. the  $fvf_{ground}$  can be calculated as:

$$fvf_{ground} = \sum_{i=-9}^8 \sum_{j=0}^{35} \frac{1}{36} (\sin(10 + i * 10) - \sin(i * 10)) I_{ground}$$

with  $I_{ground} = \begin{cases} 1 & \text{if ground is first obstacle in path of traced ray} \\ 0 & \text{otherwise} \end{cases} \quad (12)$

The factor  $(\sin(10 + i * 10) - \sin(i * 10))$  takes the geometrics of the hemisphere into account, i.e. the fact that the percentage of the field of view attributed to one ray depends upon the angle at which the ray is emitted.

The view factors have to sum up as:

$$fvf_{ground} + fvf_{buildings} + fvf_{sky} + fvf_{vegetation} = 1 \quad (13)$$

For an accurate calculation of the incoming long wave radiation at the surface of the wall/roof element this ray tracing procedure would have to be repeated at every timestep the facade temperature is calculated. Due to computational limits this is not implemented. Instead a mean temperature value of all surfaces / buildings / vegetation within the model area is used for the calculation of  $Q_{lw,ground}$ ,  $Q_{lw,buildings}$  and  $Q_{lw,veg}$ .

### 3.4. Calculation of indoor temperature

The calculation of the building indoor temperature is not only a required helper variable, but an important parameter to analyse and control a buildings thermal performance. There are two different ways the indoor temperature can be handled in ENVI-met:

- (a) as a prognostic variable progressing with respect to the calculated energy fluxes at the building envelope (non-climate controlled building) and,
- (b) as a constant value defined by the user.

In the first case, the model will calculate the evolution of the indoor temperature. In the second case the required energy to keep the given temperature value constant is calculated.

**Indoor air temperature as prognostic parameter** When the indoor temperature of a building or a building part is treated as a prognostic parameter, its value is calculated based on the energy fluxes through the associated building envelope. The indoor air temperature  $T_i^*$  of a building is derived from the heat convection from the indoor surfaces of the associated wall/roof elements plus the energy directly transmitted through transparent facade elements:

$$T_i^* = T_i + \frac{1}{c_p V} \int_{e=1}^E (A(e)(Q_{sw}^{tr}(e) + h_{c,i}(T_3^*(e) - T_i))dt \quad (14)$$

Here,  $V$  is the indoor air volume [ $m^3$ ] of the analysed building or building zone  $i$ ,  $T_i$  is the old air temperature of zone  $i$  and  $T_i^*$  is the new one after the time step  $dt$  [ $s$ ].  $E$  is the counter over all facade elements that form the envelope of the analysed building (zone)  $i$  with  $A(e)$  being the surface area [ $m^2$ ] of the wall or roof element  $e$ .  $Q_{sw}^{tr}$  is the shortwave radiation [ $Wm^{-2}$ ] that is transmitted through the facade element  $e$ . For oblique facade elements,  $Q_{sw}^{tr}$  is always zero.

The sensible heat transfer between the inner building wall and the air is taken into account through the heat convection coefficient  $h_{c,i}$ .

ENVI-met automatically defines individual buildings by checking which grid cells share a common surface. For a more detailed definition of buildings and building zones, the user must define the boundaries of the buildings or the logical building zones by hand. At the moment only vertical divisions of buildings are possible (see fig.2). It is planned to integrate the possibility of horizontal building borders in a future version of ENVI-met.

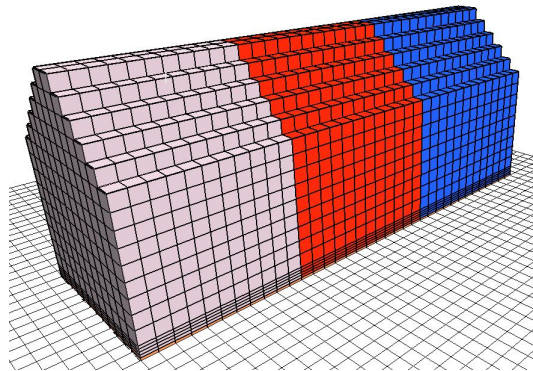


Figure 2: Building block with three different building zones (color coded). The energy budget and indoor temperature is calculated separately for each of the three building zones.

This method allows only a very rough estimation of the diurnal variation of air temperature within a building. The major flaw of this calculation is that the inside of the building is only treated as homogeneous volume of air with instantaneous heat flow and no convection. Furthermore the storage and production of heat within the building

are also completely neglected and there is also no interaction whatsoever between adjacent building zones. The volume of the air inside the building zone is calculated as  $N_b \times \Delta x \times \Delta y \times \Delta z$  with  $N_b$  as the number of grid cells occupied by a building zone. The thickness of the walls is not taken into account for this calculation. Compared to the other assumptions made in the calculation of the facade energy balance this seems to be an acceptable approach.

At the initialization of ENVI-met, the temperatures at the nodes at the inner surface node ( $T_3$ ) is set equal to the buildings indoor temperature. The temperature at the outer surface node ( $T_1$ ) is set to the air temperature of the adjacent cell. The temperature at the middle of the wall/ roof element is calculated as  $T_2 = \frac{T_1 + T_3}{2}$ .

With grid sizes of typically more than  $1m^2$  and the walls consisting of only one material, the heat flux parallel to the facades surface is assumed to be significantly lower than the heat flux perpendicular to the surface of the facade. Therefore the model only calculates the heat flux perpendicular to the surface of the wall/roof element.

As the model at the present stage only uses three nodes it is not possible to model walls that consist of more than one material - which is the case for almost all modern walls. The user has to take this into account when creating the database containing the wall/roof materials used by ENVI-met by using physical properties that are averaged over the whole depth of the wall.

During the simulation the temperature of the facades is updated at the same intervals as the air temperature. The standard time step for this update interval is set to 180 seconds.

## 4. Comparison between new and old model

In order to compare the new 3-node facade model to the old facade model a simple model area of  $10 \times 10 \times 34$  grids with a resolution of  $2m \times 2m \times 2m$  was created. In the middle of the model area a square building block with a horizontal extension of 8m (=4 grid cells) and a height of 12m was created. The facade properties of the new 3-node model were set to the following values: albedo=0.3, emissivity=0.9, K-value= $1.3 Wm^{-2}K^{-1}$ , specific heat capacity=840 J/(kgK), thickness=0.3m.

For the simulation with the old facade model the heat transmission was set to  $4.3 Wm^{-2}K^{-1}$  and the albedo to 0.3.

Otherwise the same configuration file was used for both simulations, simulating a cloudless summer day (June 23rd) with an initial air temperature of 293K (=19.85°C) and the wind coming from the east at a speed of 3m/s in 10m above ground. The air temperature inside the building block was set to 293K (=19.85°C). A second simulation using the new 3-node facade model but with a variable building temperature was also started. As can be seen in figure 3 the results of the new 3-node facade model differ noticeably from the results of the old simulation. While the temperature of the westward facade shows a diurnal variation of only 7.9K for the old facade model, the new facade model calculates a maximum temperature difference of 28.3K. For the old model the maximum

surface temperature is reached at 16:30CET while the new model calculates the maximum surface temperature for 18:30CET.

The comparison of the two runs of the new facade model shows the expected results: the maximum facade surface temperature is slightly lower (0.1K) as more energy is transferred from the facade into the building. During the night the facade of the building with variable facade temperature stays slightly warmer (0.6K) as there is an energy flux from within the warmer building inside to the outside.

The temperatures of the different nodes of the facade model shows the expected time wise shift in peak temperatures as the energy is slowly transferred from the outside node towards the inside node (Fig. 4). For the simulation with a constant building temperature the outside facade node reaches its peak value at 18:30CET, the time at which the westwards exposed facade has the maximum solar input. The center facade node reaches the maximum two hours later at 20:30CET, the inside node at 23:00CET.

For the simulation with the variable building temperature the peak for the outside temperature also occurs at 18:30 while the peaks for the center and inside node occur half an hour later than with fixed building temperature (at 21:00CET and 23:30CET).

The setting of the inside temperature not only influences the time of the peak temperatures at the different nodes but also the peak values. While the temperatures at the outer node only differs by less than 0.1K the temperature at the two inner nodes show larger deviations. The temperature at the center node differs up to 1.4K, the temperature at the inner node up to 2.5K.

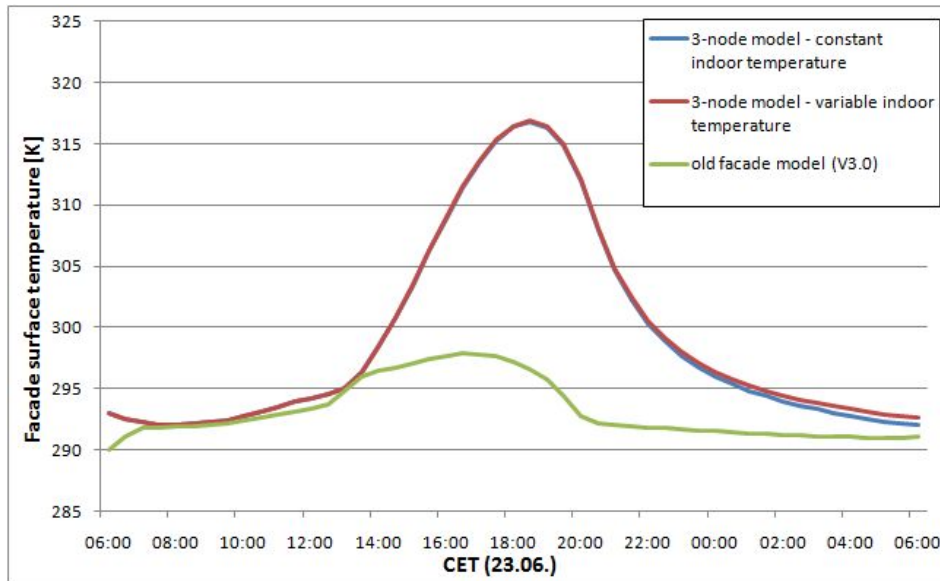


Figure 3: Comparison of simulated surface temperature of a westward facade for a cloudless summer day (23.06.) between old and new facade model. (Albedo=0.3; Heat transmission =  $4.3 \text{ Wm}^{-2}\text{K}^{-1}$ )

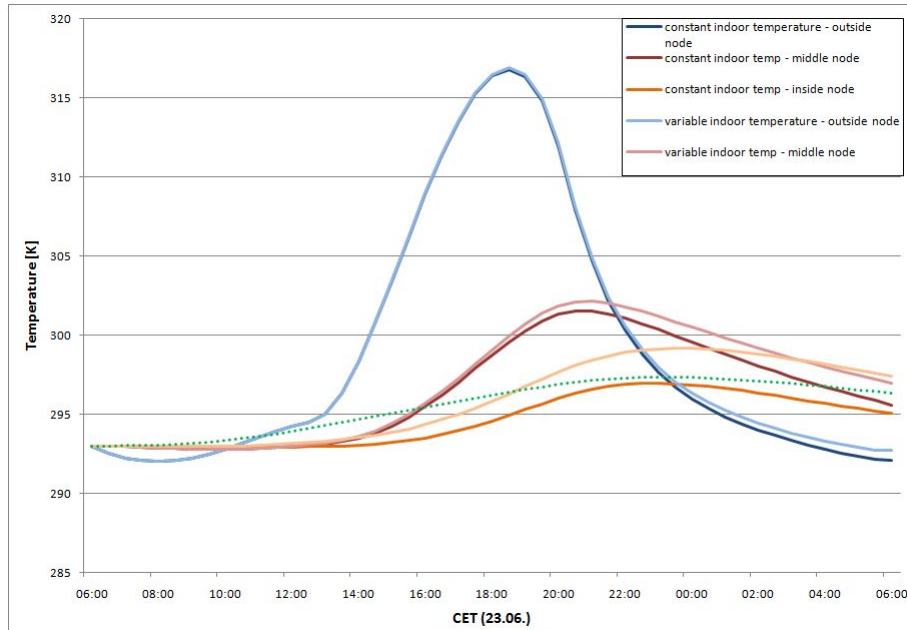


Figure 4: Comparison of simulated facade temperatures of a westward facade for a cloud-less summer day between fixed and variable indoor temperature.

## 5. Single walls

In version 4.0 of ENVI-met a new kind of building element is introduced: single walls.

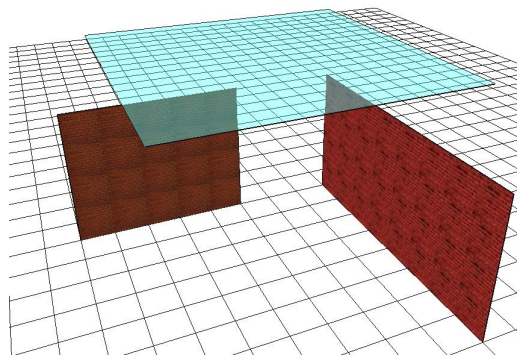


Figure 5: Example of single walls in model area.

These single walls are walls that are not an integral part of a building, i.e. are not part of the closed surface of the building. They allow to more accurately recreate obstacles like small walls, awnings or similar structures that do not fill a whole grid cell (Fig.5). Before the introduction of these single walls such elements had either to be neglected or be approached by putting a building in the grid cell concerned.

Single walls in ENVI-met have the same physical properties as normal walls. They are a solid obstacle for wind flow and turbulence but can transmit radiation.

These single walls however do not use the same routines for the calculation of their temperature as normal walls. The main difference is the assumption that those single walls are thin and not well insulated - i.e. have a low heat transfer coefficient  $\lambda$  - and therefore have a homogeneous temperature distribution within. With this assumption their temperature can be calculated by solving the single equation of their energy balance:

$$Q_{sw,net}^{abs} + Q_{lw,net}^{abs} - 2\varepsilon\sigma T_w^{*4} + (4 + 4v_1)(T_{air,1} - T_w^*) + (4 + 4v_2)(T_{air,2} - T_w^*) = \frac{c_{wall}\rho_w\Delta x}{\Delta t}(T_w^* - T_w). \quad (15)$$

$T_w^*$  is the temperature of the single wall at the next time step,  $v_1$ ,  $v_2$ ,  $T_{air,1}$  and  $T_{air,2}$  the wind speed and air temperature at the grid cells that are separated by the single wall.

This equation can be transformed into

$$2\varepsilon\sigma T_w^{*4} + T_w^*((4 + 4v_1) + (4 + 4v_2) + \frac{c_{wall}\rho_w\Delta x}{\Delta t})T_w^* - (Q_{sw,net}^{abs} + Q_{lw,net}^{abs} + \frac{c_{wall}\rho_w\Delta x}{\Delta t}T_w + (4 + 4v_1)T_{air,1} + (4 + 4v_2)T_{air,2}) = 0 \quad (16)$$

and then solved by applying the Newtons method.

## 6. Remodeling the ENVI-met editor

In versions prior to 4.0 of ENVI-met the whole creation and editing of the model area is done in a 2D mode. The user sees the horizontal grid of the model area and can define the top and bottom of a building for every grid cell. This allows an easy digitization of the model area and the information can be stored in a normal text file - that can also be edited with a normal text editor. However this approach allows neither complex architectural structures like e.g. buildings with holes in them nor is it possible to use different wall materials for every single facade element.

In order to overcome these shortcomings and take full advantage of the new 3-node facade model the whole ENVI-met editor had to be reengineered. The new editor of the ENVI-met package 4.0 now incorporates a full 3D data format as well as a 3D editing tool.

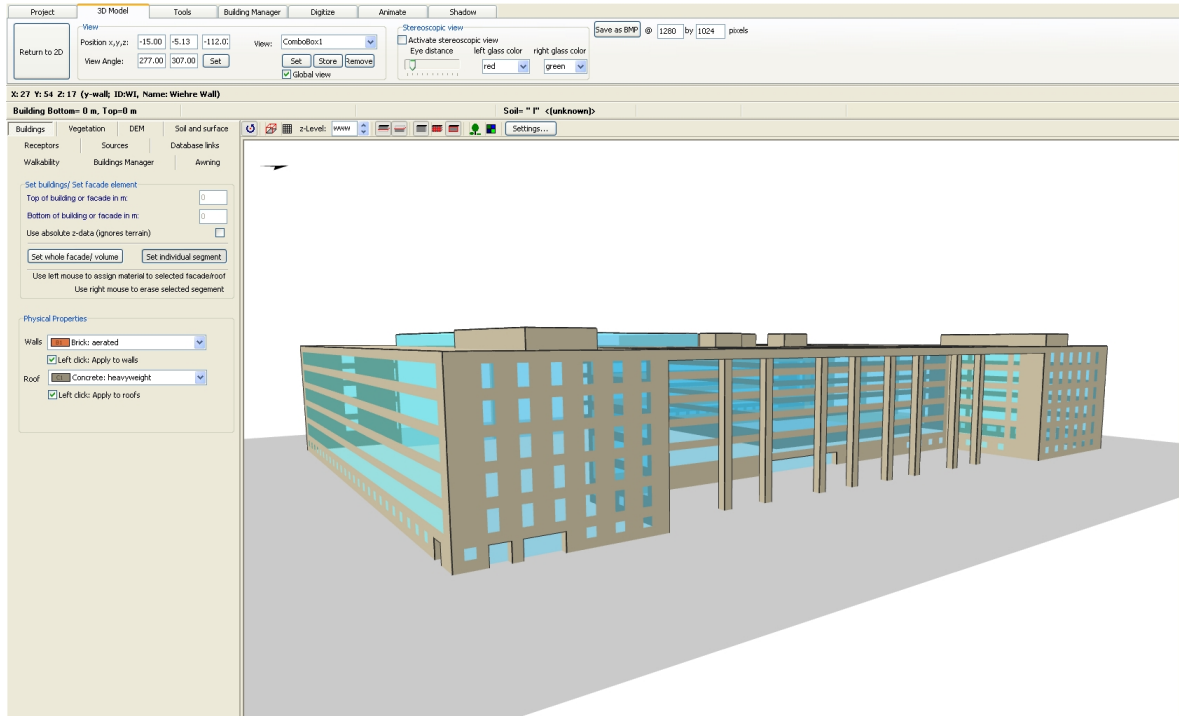


Figure 6: Prototype of the new model area editor for ENVI-met

The new file format uses a three dimensional grid in order to define which grid cells are occupied by buildings and which facade materials are used. For latter information three data fields are needed: one for each way a facade can face in the editors rectangular grid (x,y,z). This information is then saved in a binary file. The wall directions are defined according to the direction of the normal of the surface (fig.7)

This new file format can only live up to its full potential if the editing also allows to modify each grid cell. Therefore the editor now offers a 3D view that enables the user to look and work on his model area from every possible angle. The visualization in 3D is realized using the cross-language, cross-platform application programming interface OpenGL. In this 3D view the user can assign a specific material to every facade element of every grid cell and get corresponding visual feedback. Different wall/roof materials can either be represented by different (user definable) colors or by textures. Transparent materials, e.g. glass, can also be rendered as transparent.

The physical properties of each facade material (tab. 1) are stored in a text file database which is common to the editor and ENVI-met itself. In the building file there only is a link to this database rather than to the actual values, allowing an easy readjustment of the physical properties of wall and roof materials.



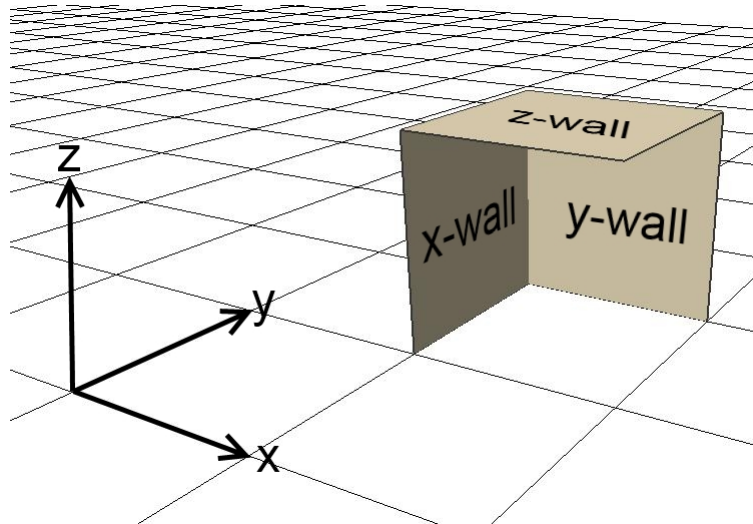


Figure 7: Wall directions.

In order to facilitate the creation of model areas in this new 3D format an additional software tool has been created that can import 3D polygon models in the file formats COLLADA (Collaborative Design Activity) and DXF (Drawing Interchange File Format) and transform them into the block based format of ENVI-met.

The XML based COLLADA format is best known for its use in Google Earth. The proprietary but well documented DXF format has been introduced by Autodesk in 1982 in combination with the well known computer-aided design software AutoCAD. Both formats are supported by a wide variety of 3D modeling software so that virtually any 3D polygon based model can be transferred into one of these formats.

The software transforms the polygon based models into the block model used by ENVI-met (fig. 8). At the moment only the geometric information of the models is extracted and further information like textures or materials are completely neglected. It is planned to integrate this information in future versions of the tool.

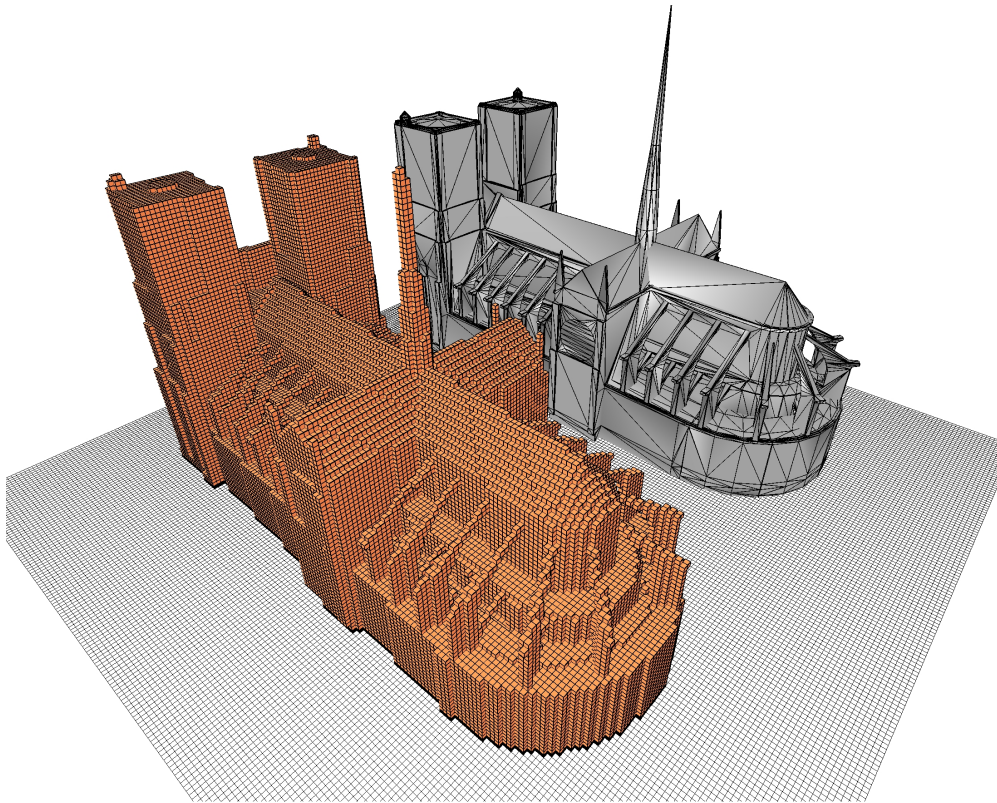


Figure 8: Transformation of a complex polygon based 3D model (rear) into block based ENVI-met model area (front)

## 7. Validation

In order to judge the quality of the new wall/roof model, simulated values were compared to measurements of the facade surface temperature taken at the outdoor testing site of the Fraunhofer Institute for Building Physics (IBP) in Holzkirchen, southern Germany. Unfortunately only data for several roof elements are available for comparison here. As the measurements were taken on a flat roof the results of this comparison are assumed to be also applicable for wall elements.

### 7.1. Model area

The outdoor testing site of the IBP offers a large area to test building constructions, building components and buildings materials as well as installation components for heating systems, ventilation and energy systems on a 1:1 scale under real climate conditions. The area is situated at  $47.9^{\circ}$  N,  $11.7^{\circ}$  E at about 700m above sea level. Nearly all facades are directly pointing in direction of one of the four cardinal points. Some of the

buildings have angled roofs which cannot be correctly simulated in ENVI-met with its strictly orthogonal grid structure. For the comparison of simulated and measured roof temperatures a building with a flat roof was therefore chosen.

A weather station is situated on site. Data from this weather station were used to force the diurnal variation of the meteorological parameters at the inflow boundary of the model area, thus ensuring that the simulated atmospheric conditions correspond to those of the day the measurements were taken on.

The size of the model area is 145m in east-west direction and 269m in north-south direction. The resolution of the grid is 1m in all directions, resulting in a total of  $145 \times 269 \times 34$  grid cells. Most buildings within the model area are lower than 10m, the tallest building height being 14m.

## 7.2. Simulation

The 10th of April 2009 was chosen as simulated day. It was a sunny day in spring with nearly no cloud coverage and air temperature of up to  $23^{\circ}\text{C}$  in 2m above ground and wind speed in 10m above ground varying between 1 and 3.5m/s.

The simulation starts shortly after dawn at 6CET and runs until 5CET the next morning. The diurnal variations of air temperature, wind speed and direction, atmospheric long wave radiation and the direct and diffuse incoming shortwave radiation measured by the weather station on site were used to create corresponding boundary conditions for the simulation with ENVI-met (see part IV). The boundary conditions for these parameters are given every full hour. ENVI-met automatically interpolates linearly between these sampling points.

The temperature at the inside of the buildings was set to a fixed value of  $20^{\circ}\text{C}$  throughout the simulation.

The relative humidity in 2m above ground was set to 80% at the start of the simulation at 06:00CET.

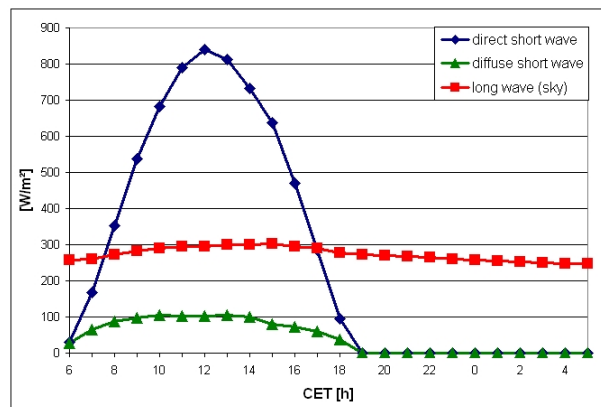


Figure 9: Boundary conditions for incoming long wave and short wave (direct and diffuse) radiation. Measurements taken by on-site weather station.

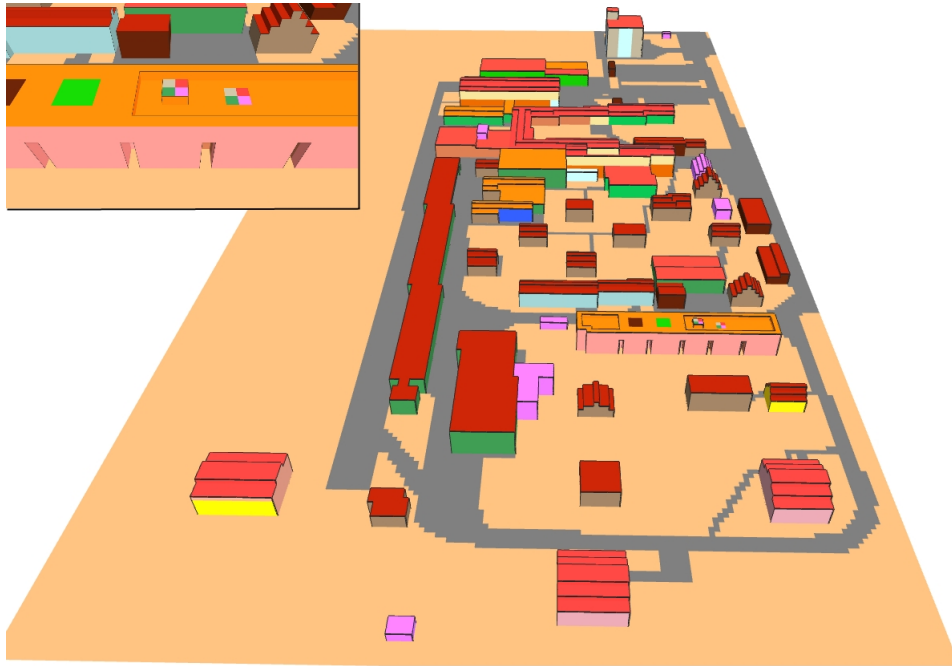


Figure 10: Model area and building with test roofs (top left). Facade materials and soil type color-coded

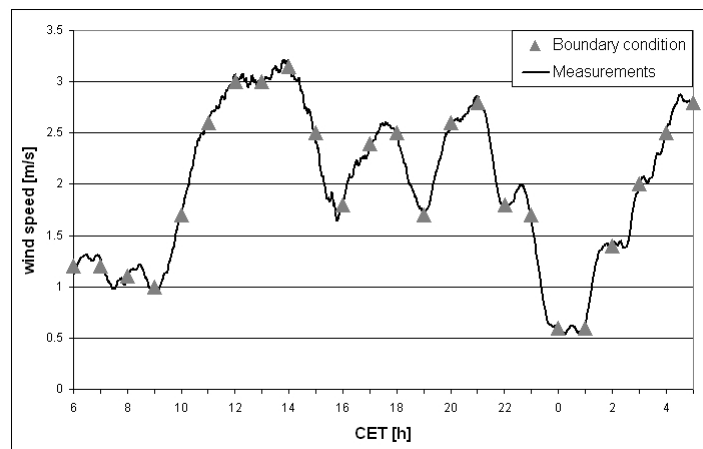


Figure 11: Measurements of wind speed and boundary conditions for simulation in 10m above ground. Black line: moving average (60 minutes) of measurements. Grey triangles: values used for the boundary conditions of the simulation.

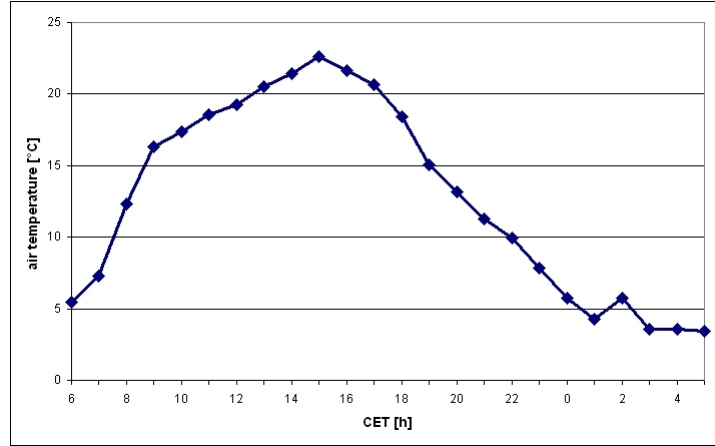


Figure 12: Air temperature in 2m above ground at inflow boundary.

### 7.3. Modeled roof elements

For this work the temperatures of four flat roof elements were chosen for the comparison between measured and simulated facade surface temperature. The roof has a height of 6m above ground and is not shadowed by any other building or tree. All elements consist of the same material but are painted in different colors (Tab: 1).

Table 1: physical properties of selected roof elements

	density [ $kg/m^3$ ]	rf [%]	ab [%]	tr [%]	$\varepsilon$ [%]	$\lambda$ [ $W/(mK)$ ]	$c_{wall}$ [ $J/(kgK)$ ]	$\Delta x$ [m]
black roof	770	5	95	0	90	0.07	1000	0.2
grey roof	770	15	85	0	90	0.07	1000	0.2
silver roof	770	80	20	0	5	0.07	1000	0.2
white roof	770	77	23	0	86	0.07	1000	0.2

The radiative properties of the facades surface were measured directly. As the roof consists of several layers of different materials, the values for density, heat transfer coefficient and specific heat capacity were calculated as average values for the whole layer of roof element.

### 7.4. Comparison

At the start of the simulation the temperature of the outside surface of the facades is set equal to the air temperature. Several test runs with different initialization temperatures of the roof elements have shown that the effects of the initialization temperature is only visible during the first hour of simulated time.

This observation however is only valid because of the specific physical properties of the facade material and the fact that the roof elements are exposed to direct sunshine from

the start of the simulation on. If this was not the case, i.e. the roof element had a lower heat transfer coefficient or was shaded at the beginning of the simulation, the initialization temperature would have a longer lasting effect on the simulations results. In this section only the results from 7CET onwards are compared to the measurements. The comparison between simulated and measured facade surface temperatures shows an overall good agreement (Tab. 2). In the morning hours however a distinctive deflection can be observed for all four differently colored roof elements (Figs. 13-16). The simulated values lag approximately half an hour behind the measured ones - albeit the fact that the simulated and measured temperatures at 7CET, one hour after initialization, differ by only 2K. From noon on this lag is no longer visible.

The cause of this lag is most probably due to the model roof consisting of only one material while the real roof features several layers of different materials. Due to the lower heat transfer in the outer (insulating) layer this layer heats up faster than the homogeneous material in the model wall.

The peak in measured facade temperature at 15CET for all elements can be explained by a short drop in wind speed to 1m/s for several minutes before and after 15CET. This short decrease in wind speed is not visible in the moving average of 60 minutes that was used for creating the boundary conditions (Fig. 11). A reduced wind speed leads to reduced heat exchange between surface and air. As the surface temperatures at this point greatly exceeds the air temperature above the roof less energy from the roof is transferred to the air, leading to an increase in the surface temperature of the facade.

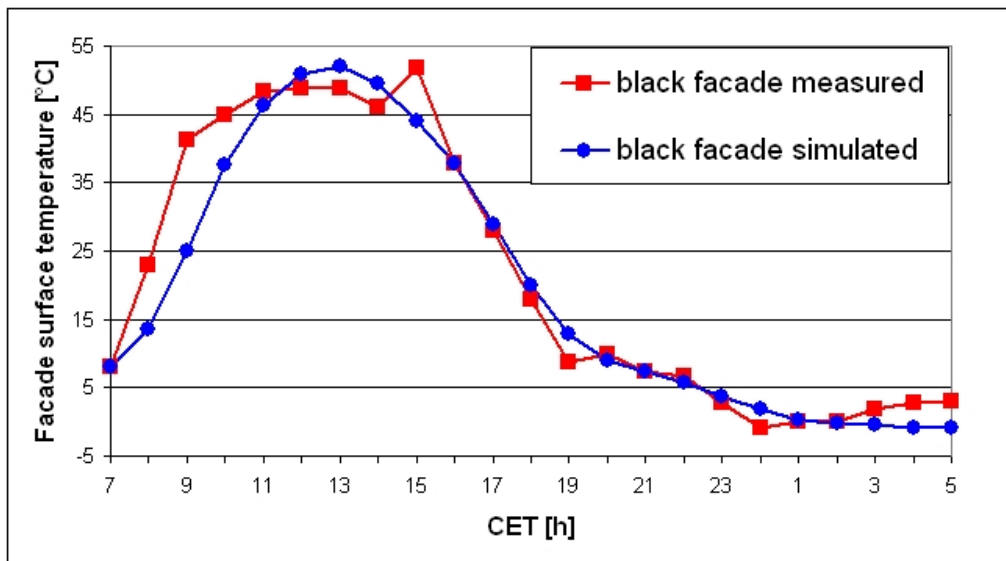


Figure 13: Measured and simulated surface temperature of black roof element

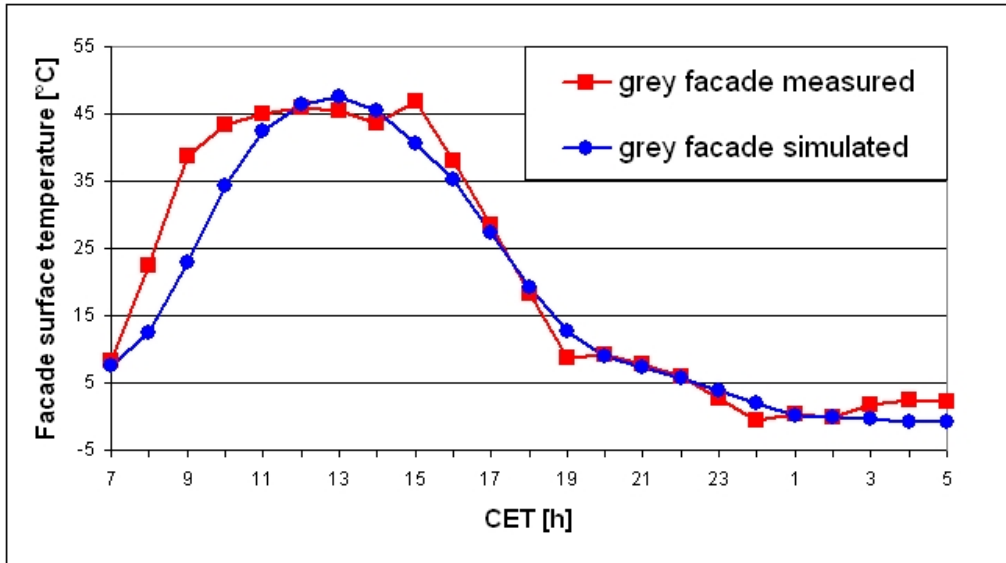


Figure 14: Measured and simulated surface temperature of grey roof element

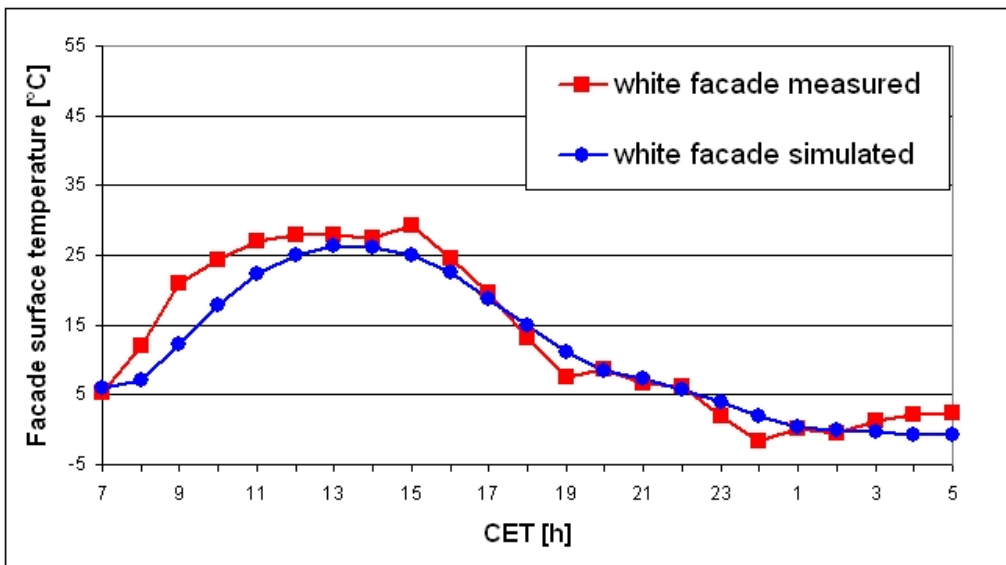


Figure 15: Measured and simulated surface temperature of white roof element

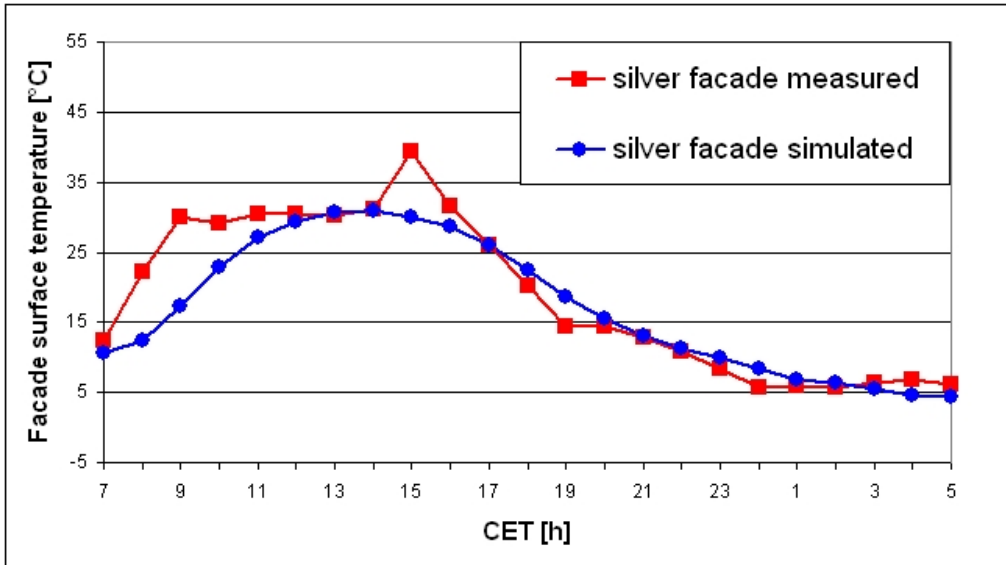


Figure 16: Measured and simulated surface temperature of silver roof element

Table 2: Comparison between measured and simulated facade surface temperatures. Average deviation and root mean square error

	root mean square error [K]	$R^2$
black roof element	5.0	0.93
grey roof element	4.8	0.91
white roof element	3.1	0.87
silver roof element	4.2	0.83

## 8. Conclusions

Despite its simplicity the new approach to calculating facade surface temperatures is a huge step forward for the accuracy of ENVI-met. The three-node model manages to reproduce the typical diurnal variation of the surface temperature. In combination with the new editor that allows to set each facade element separately ENVI-met is now able to simulate the surface temperature of a building much more realistically (see fig. 17).

At the moment the model still has two major drawbacks:

- the wall/roof elements can only consist of a single material. The physical properties of wall/roof elements that consist of more than one material can only be approximated by modeling a material that has the average physical properties of all materials used in the real facade element.



- the simulation of the indoor air temperature is overly simplified. ENVI-met completely neglects inner walls that block the air flow within a building, can act as additional heat storage and define the heat exchange between adjacent building sections. Neither are additional internal heat sources as personal computers, printers or humans implemented.

The first drawback can easily be solved by the implementation of more nodes with different (material properties) into the wall temperature model. This would only require very little additional computing time. The number of nodes  $N_n$  necessary to simulate a wall consisting of  $x$  different materials is  $N_n = 2x + 1$ . A first test with a seven-node model, i.e. walls and roofs consisting of up to three different materials, shows promising results. But further testing has to be done.

Regarding the simulation of temperatures inside buildings the best solution is to couple ENVI-met with a specific simulation of the energy balance of buildings. The implementation of all elements necessary to realistically calculate the indoor air temperature of buildings would not only require a lot of work on the model itself but would also drastically increase the simulation time - all the while not offering the same accuracy as software specifically designed to calculate the energy balance of buildings.

ENVI-met will therefore only be able to provide a very rough estimation of a buildings energy balance and the diurnal variation of air temperature within.

Another possible amelioration for the three-node model would be to implement the energy fluxes parallel to the surface of the facade. At the moment this is not planned to happen in the near future as it is not certain that the gain in accuracy justifies the costs and other measures that promise to be of more advantage, like increasing the number of nodes, should be implemented first.

The calculation of the surface temperature of the newly introduced single wall elements in its current state is physically less accurate than the formulas used for the calculation of the energy balance of wall/roof elements. These single walls simulate mostly very thin elements like sun-sails made from cloth, or wind blocking elements made from thin sheets of wood or glass, which have a rather evenly distribution of temperature within and do not have a huge heat storage capacity. The simplified calculation method therefore seems justified and the effects of a more accurate simulation of surface temperature of these single wall elements on human thermal comfort within street level or atmospheric temperature is thought to be negligible.

However, in future versions of ENVI-met a modified version of the three-node-model might also be used for the calculation of the energy balance of these elements.

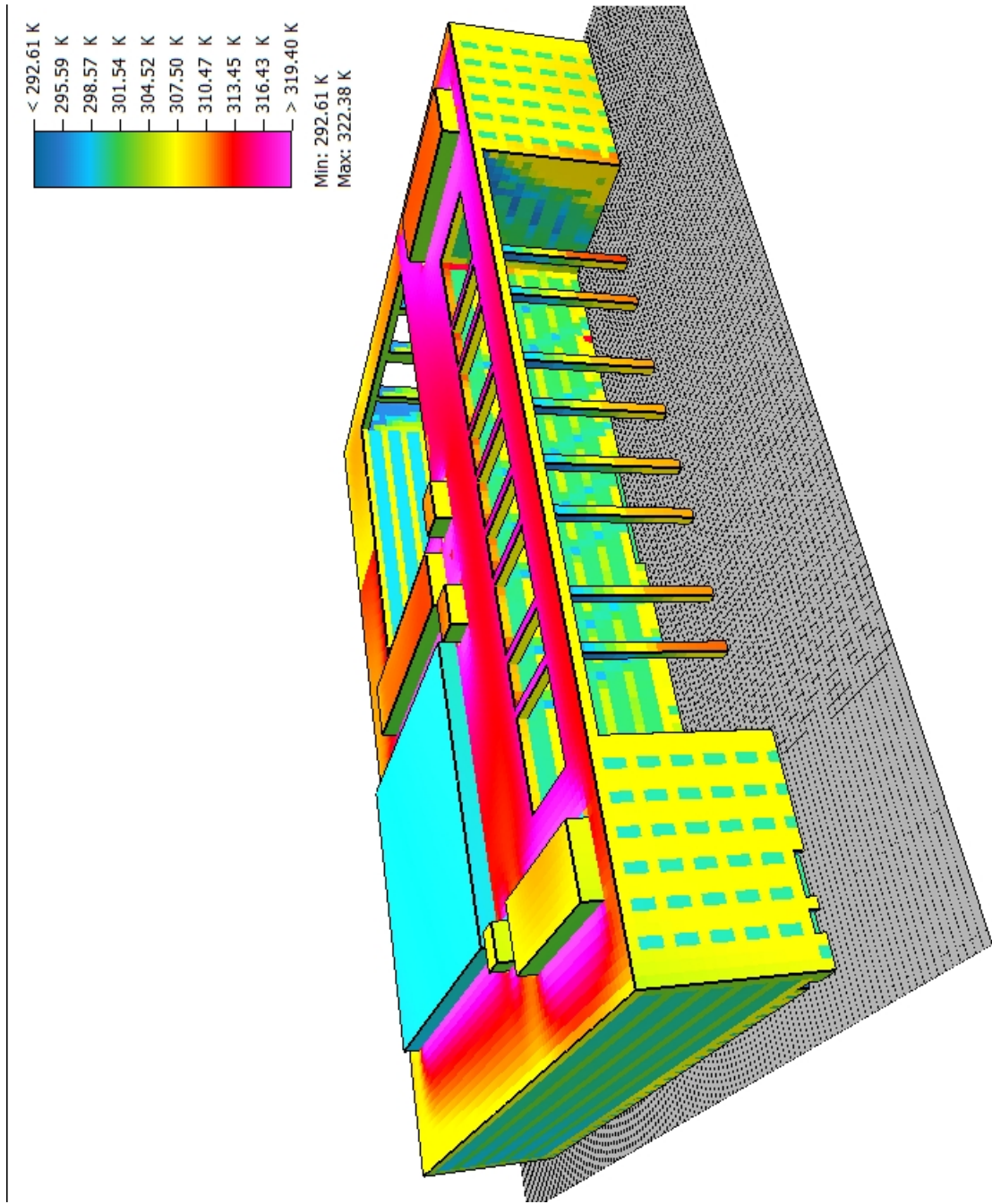


Figure 17: Modeled surface temperature of a complex building model.

## References

- Din 6946: Building components and building elements. thermal resistance and thermal transmittance calculation method, 2005.
- F. Ali-Toudert and H. Mayer. Numerical study on the effects of aspect ratio and orientation of an urban street canyon on outdoor thermal comfort in hot and dry climate. *Building and Environment*, 41:94–108, 2004.
- W. Terjung and P. O'Rourke. Simulating the casual elements of urban heat islands. *Boundary-Layer Meteorology*, 19(1):93–118, 1980.



## Part IV.

# Implementing user-defined atmospheric boundary conditions into the numerical microclimate simulation ENVI-met

## 1. Summary

Up to Version 3.1 the micro-climate simulation ENVI-met develops its own diurnal profile for all atmospheric variables. The diurnal variation mainly depends on the geographical position of the model area and the simulated date, the initialization values and the selected lateral boundary conditions of the model are. While this method offers an easy approach with a minimum of necessary input data it is neither possible to validate the simulations with measurements, nor to simulate specific scenarios, like e.g. the impact of climate change.

This section describes how a “forcing” mechanism that allows the user to manually define the diurnal variation of all meteorologically relevant variables at the inflow boundary was implemented in ENVI-met. This new feature finally allows a realistic comparison between simulation and measurements.

To show the performance of the forcing mechanism the results of two measurement campaigns are compared to the output of the same areas modeled in ENVI-met using forcing. The two model areas analyzed are situated in Freiburg (SW Germany) and were subject to the joint research project KLIMES. Measurements of wind speed, air temperature, relative humidity and the radiative fluxes were conducted in both areas. These measurements were compared to the data of simulations performed with ENVI-met, using the boundary conditions of the specific days the measurements took place. The data for the diurnal profile of the boundary conditions were derived from measurements of a weather station situated 53m above ground 1km and 3km north of the model areas.

The comparison between measurements and simulations shows a good overall accordance, but also illustrates the limitations of the described methods for the creation of the inflow profiles.

## 2. Introduction

The quality of the results of a micro-climate simulation like ENVI-met strongly depends on the accuracy of the boundary conditions used in the simulation.

In versions prior to ENVI-met 4.0 uses a few meteorological input variables (initial temperatures of air and soil, wind speed, humidity) together with geographical information

to create its own diurnal profile of atmospheric conditions at the inflow boundary of the model area.

This approach has the advantage that the model requires only very few input variables to simulate atmospheric conditions within the model area over a period of time and thus also allows people with only little meteorological and numerical background knowledge to use ENVI-met and get reasonable results.

The disadvantage of this approach however is that it results in - spatially and temporally - heavily idealized boundary conditions, making it very difficult, if not impossible to validate the simulations made with ENVI-met, to use ENVI-met within the context of field measurements or to use the output of mesoscale numerical models as input for micro-scale simulations with ENVI-met.

This chapter describes the improvement of ENVI-met regarding the above-mentioned limitations, allowing the user to manually define the boundary conditions of the model, using The quality of the newly implemented forcing mechanism is shown by a comparison between a forced simulation with ENVI-met and measurements made in Freiburg [Mayer et al., 2008] in the summer of 2007 within the KLIMES project.

### 3. ENVI-met model run without forcing

In standard - non-forcing - mode of ENVI-met the diurnal variation of all meteorological parameters is defined by the following start-up parameters that are defined in the configuration file:

- geographical position and time (solar radiation)
- $u_{10m}$ : horizontal wind speed in 10m above ground
- wind direction
- $z_0$ : roughness length
- $T_{start}$ : initial air temperature
- $q_H$ : specific humidity at the top of the model (H=2500m)
- $f_{rel,2m}$ : relative humidity in 2m above ground
- $T_{start,s}$ : initial soil temperature
- $N$ : cloud cover (in  $\frac{1}{8}$ )

With these initialization values the program first calculates an 1D model that extends from ground level up to a height of 2500m above ground. From the ground to the top of the 3D model the 1D model has the same spacing as the 3D model. The 1D model is then integrated until the vertical profile of all variables (wind speed, turbulence, air temperature, specific humidity) is in a quasi-stationary state. Subsequently this 1D model is used to initiate the 3D model.

The initialization of the wind field of the 3D model is achieved in three steps: first the wind flow in the model area without any obstacles is calculated. In the second step the obstacles are set to a porosity of 50% and the wind flow is adapted accordingly. In the last step the obstacles are set to their final porosity. After each step the wind field is recalculated by integrating over the space of time of 10s. This ensures that the wind field becomes quasi-stationary and can be used as the initialization wind field of the simulation.

During the simulation run itself the development of the atmospheric variables within the 3D model area strongly depends on the boundary conditions chosen for the simulation. For the 3D model there exist three different settings for the lateral boundary conditions:

- open: the values of the next grid point close to the border are copied to the border for each time step.
- forced (closed): the values of the 1D model are copied to the border.
- cyclic: the values of the downstream model border are copied to the upstream model border.

The default boundary condition is set to open because it is the boundary condition that least influences the inner parts of the model. But as well as the cyclic boundary condition it is slightly prone to numerical instabilities due to undesired feedback.

The boundary conditions at the top of the model area are set to forced for all variables, i.e. the values from the 1D model are copied to the top of the 3D model.

At solid obstacles like buildings and digital elevation model a so called *No-Slip* condition is applied:  $u = v = w = 0$ .

This kind of model initialization has the huge advantage that only very few parameters have to be known in order to start a simulation. Thus also users with very little meteorological knowledge can successfully start a simulation.

But unfortunately this initialization is not capable of producing realistic diurnal variations for most meteorological variables. The diurnal variations are highly idealized and often do not even reproduce days with meteorologically “boring” weather (i.e. a stable atmosphere) accurately.

## **4. Nesting and Nudging - making climate simulations match observations**

### **4.1. Nesting - general**

One of the problems all regional climate models face is that these models only simulate a part of the global atmospheric system and therefore can not accurately simulate the atmospheric conditions within the model area over a prolonged period of time because

of the lack of knowledge about the physical properties of the air masses advected from outside of the model area.

In order to solve this problem the regional model has to be provided with additional information from a larger scale model or meteorological measurements at the inflow boundaries of the model area (fig. 1). This information can then be used for the boundary conditions of the regional climate model.

The use of a coarser, larger scale model that provides the boundary conditions for the regional climate model is usually referred to as nesting. There are two different nesting modes:

- one-way nesting. The output of the model with the coarser resolution is used to drive the higher resolution model. The coarser resolution simulation is run independently and does not get any feedback from the higher resolution simulation (e.g. [Giorgi and Bates, 1989], [Ji and Vernekar, 1997]).
- two-way nesting. The coarser resolution simulation is used to provide the boundary conditions for the higher resolution simulation and at the same time the higher resolution simulation provides feedback to the coarser resolution simulation (e.g. [Zhang et al., 1986]) .

The two-way nesting is the physically more accurate solution while the one-way nesting is easier to implement. For two-way nesting to work correctly both simulations have to use exactly the same model physics and parametrizations and have to feature a corresponding interface. It is thus not possible to combine just any two simulation programs. In most cases in which two-way nesting is used the same simulation software calculates the larger, coarser simulation area as well as one or more nested areas with a higher resolution within. Examples for climate models capable of this are the “PSU/NCAR mesoscale model” (known as MM5) [Dudhia et al., 2005] or the “weather research and forecasting model” (known as WRF) [Moeng et al., 2007].

The results of nested simulations however do not only depend on the quality of the simulation of the coarser area but also on several other factors [Denis et al., 2002] [Warner et al., 1997]:

- the numerical formulation of the nesting, i.e. the way the results of the coarser simulation grid are applied at the boundaries of the finer resolution grid [Staniforth, 1997]
- the scale differences between the two grids. The larger the difference in grid resolution, the more information is lost due to spatial interpolation. For the MM5 model the nesting ratio is usually 3:1, other models have similar restrictions. If higher ratios are desired a cascade of nestings (i.e. a nesting grid within a nesting grid) has to be applied (e.g. [Christensen et al., 1998]). Furthermore larger grid resolutions allow larger time steps within the simulation, adding possible inaccuracy due to temporal interpolation.
- the size and position of the nested grid in relation to the coarser grid [?].



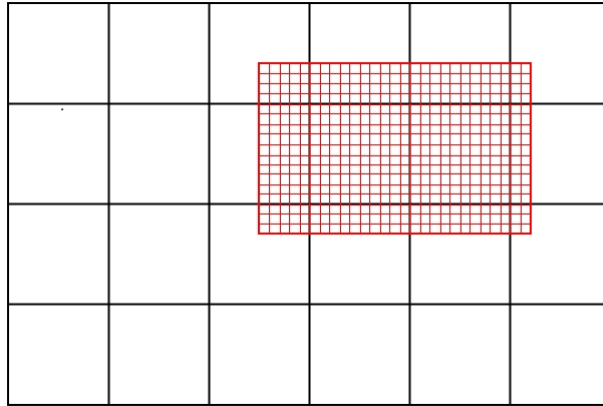


Figure 1: Concept of nesting: a high resolution nesting area (red) is positioned within a coarser resolution model area (black) that provides the lateral boundary conditions for the nesting area.

- the size of the nested model area. The smaller the size of the nested area, the more the results are influenced by the boundary conditions. If the area is however too large the atmospheric processes in the middle of the nested area might not comply with the conditions prescribed by the coarser model (e.g. [?]).

#### 4.2. Nudging - general

One way of implementing a one-way nesting into climate simulation is to just replace the results of the different variables  $\Phi$  at the inflow boundary of the higher resolution grid with the results of the the corresponding grid cell from the coarser grid simulation  $\Phi^f$ .

A more sophisticated approach which is used by some models is to not only force the values of the grid cells at the inflow boundary but to also nudge the results of grid cells that are further away from the border towards the value  $\Phi^f$  provided by the nesting simulation. This process is often referred to as nudging and it can be written as

$$\Phi^{n+1} = (1 - \delta_n)\Phi^* + \delta_n\Phi^f.$$

$\Phi^*$  is the original result of the higher resolution model calculated for time step  $n + 1$  and  $\delta_n$  is the so called nudging coefficient, a non-physical variable that ranges between 0 (no nudging) and 1 (result is identical to forcing value  $\Phi^f$ ). The actual value of the nudging factor depends on the distance of the regarded grid cell from the boundaries of the model area. Directly at the boundaries the value is normally set to  $\delta_n = 1$  and decreases rather quickly towards the center of the model area. There is however no unique solution and every model uses a different approach [Schlünzen, 1996].

In comparison with the forcing of only the grid cells at the boundaries the nudging has

the distinct advantage of being able to better control the impact of the coarser grid simulation on the nested simulation. Furthermore this approach can also be used in a non-nesting scenario in order to nudge the simulation towards measurements. In this case the nudging factor would have to be adapted in a way that  $\delta_n = 1$  at the sites where the measurements were taken.

### 4.3. Nesting, Nudging and ENVI-met

Regarding ENVI-met and the possible use of nesting there are mainly two problems. The first problem is a numerical/ computational one: due to the small grid size of the cells in ENVI-met (0.5m-10m) a long cascade of nestings would be necessary in order to nest it into a meso-scale climate model, demanding a lot of computing power. When trying to circumvent this problem by using a larger nesting ratio of above 10:1 the accuracy of the model output would be decreased.

The second problem is caused by the usage of ENVI-met. A significant part of ENVI-mets user base consists of urban planners and architects who have neither the necessary meteorological background knowledge nor the necessary computing power that would be needed to take advantage of a version of ENVI-met that can nest its model area into the output of a meso-scale climate simulation software. Most requests by ENVI-met users concerning this topic concentrate on the ability to have a better influence on the diurnal variation of air temperature and wind speed and thus more accurately recreate the meteorological conditions of a certain day when measurements were taken.

Nudging was regarded as an option for ENVI-met but has not yet been implemented. With the limited number of cells currently available the nudging factor  $\delta_n$  would have to decrease very quickly the further away from the border. Otherwise the nudging might annihilate the subtle changes in microclimate that can occur within the distance of a few meters.

Therefore a simpler approach which does not require an additional simulation and does not include nudging is used in this first implementation of forcing in ENVI-met.

## 5. Concept of Forcing in ENVI-met

In order to compare the results of a numerical simulation with measured data or to simulate a specific meteorological development it is necessary to “force” the simulation by adjusting the variables at the inflow boundaries of the model.

ENVI-met up to version 3.1. already supports a so called “forced (closed)” boundary condition. With this boundary condition the values of the 1D model are copied to the grid cells at the inflow boundary of the model. The implementation of “forcing” in ENVI-met uses this boundary condition and lets the user define the temporal and spatial development of the 1D model.

While the forced boundary condition itself has no problems with numeric instability due

to undesired feedback from and to the model area, the user-defined 1D-profiles have to be chosen carefully: drastic changes in the variables, particularly wind speed and wind direction, can easily cause numeric instabilities. These problems can however partly be avoided by adapting the time steps for the interpolation between user-given 1D profiles as well as for the calculation of the forced variables themselves.

## 6. Forcing in ENVI-met

### 6.1. Variables that can be forced

The variables that can be forced are:

- $u_{hor}$ : horizontal wind speed
- wind direction
- $T$ : potential air temperature
- $q$ : specific humidity
- $R_{sw,dir}^\downarrow$ : short wave direct radiation
- $R_{sw,dif}^\downarrow$ : short wave diffuse radiation
- $R_{lw}^\downarrow$ : incoming long wave radiation
- $N$ : cloud cover
- background concentration of particles/ gases

Apart from two exceptions these variables can be forced independently from each other and in any chosen combination. The two exceptions are:

- cloudiness and radiation. These can not be used at the same time since the cloud cover has a direct influence on the radiation budget.
- wind speed and direction: as these two variables are closely coupled it is not possible to force only one of them. They always have to be used together.

Meteorological variables that are not provided by the user are calculated by ENVI-met, based on the settings for the model initialization made in the configuration file.

### 6.2. Input data

As input format for the forcing data a specially formatted text file was chosen. In this text file the values for the forced values are chronologically listed. The user can freely select the temporal interval of the forcing, with ENVI-met using a linear temporal interpolation in between the given values.

The recommended intervals for forcing strongly depend on the values that are to be forced.

ENVI-met expects the atmospheric variables that have a vertical profile (wind speed and direction, air temperature and specific humidity) and are to be forced to be given at at least of two height levels: ground level ( $z=0$ ) and the top of the (1D) model area ( $z=2500\text{m}$ ). Values for all height levels in between can be interpolated by ENVI-met, using very basic interpolation methods.

A software tool has been written in order to facilitate the creation of these forcing files. This software always extrapolates the values for height level 0m and 2500m from a value provided at any height between.

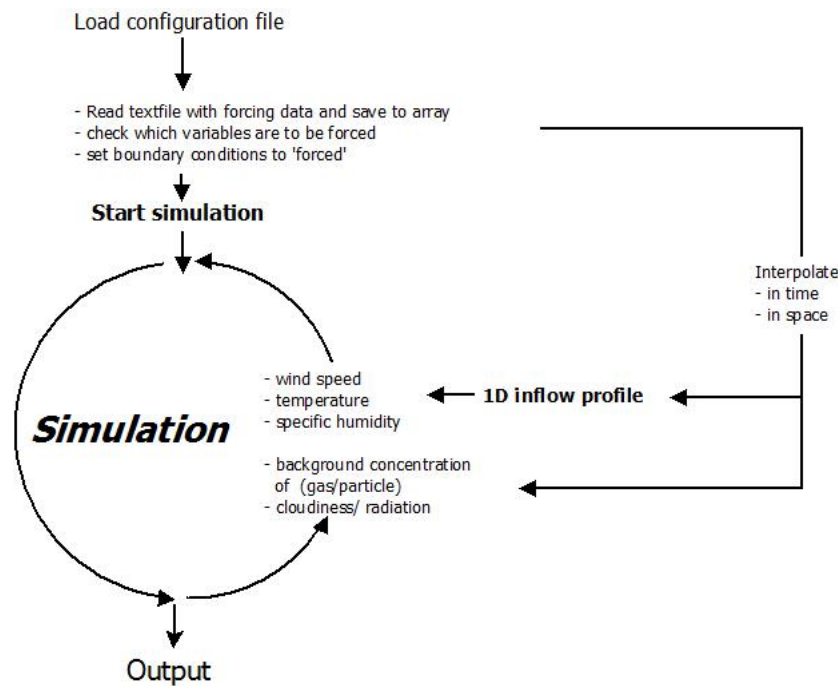


Figure 2: Schematic work flow of ENVI-met with Forcing enabled

### 6.3. Radiation

The forcing of the radiation can be achieved either by adjusting the values for cloud cover, with ENVI-met calculating the incoming radiation at model height, or by providing the measured values for incoming direct and diffuse short wave radiation as well as long wave radiation.

### 6.3.1. Cloud cover

The cloud cover  $N$  has to be given in the meteorologically usual way of  $\frac{N}{8}$ , with  $\frac{0}{8}$  being a clear sky and  $\frac{8}{8}$  being a totally cloud covered sky.

The radiative properties of a cloud strongly depend on the composition of the cloud. ENVI-met therefore discerns between low ( $N_l$ ), middle ( $N_m$ ) and high ( $N_h$ ) clouds, with  $N = N_l + N_m + N_h \leq 8$ . For the calculation of the short and long wave fluxes at the top of the 3D model ENVI-met uses a two-stream approximation and some empirical formula (Taesler and Anderson 1984).

If cloud cover is forced ENVI-met uses a linear temporal interpolation for all three cloud covers. The linear interpolation can in certain cases lead to  $N > 8$ . If this happens the software first lowers  $N_m$  so that  $N_h + N_m \leq 8$  and then  $N_l$  until  $N = N_h + N_m + N_l = 8$ .

### 6.3.2. Radiation

In most cases only the incoming global short wave radiation is measured, making it necessary to calculate or estimate the ratio of direct to diffuse short wave radiation. As this ratio hugely depends on cloudiness and the optical density of the atmosphere, it is not possible to implement an automated splitting of this variable into ENVI-met. Without the availability of further measurements, the user can solve this problem by forcing cloudiness instead of radiation.

The calculation of the incoming long wave radiation, which is often not measured at weather stations, can be done by ENVI-met. If the forcing value for the incoming long wave radiation is set to zero, ENVI-met calculates this value using air temperature, humidity and cloudiness - the latter being automatically set to zero in the case of short wave radiation being forced. This is a limitation that has to be kept in mind if only short wave radiation is forced and clouds are present during the measurement.

## 6.4. Gas and particles

In order to do research on the distribution of particles and gases and their interaction with plants, it is also possible to force the background concentration of various gases and particles (De Maerschalck et al., 2008). The temporal interpolation between the given values is linear.

## 6.5. Wind speed

The wind speed is always assumed to be 0m/s at ground level (0m) (*No-Slip* condition). For the top of the model it is extrapolated logarithmically to 2500m from the next lower height level for which a value is given.

## 6.6. Wind direction, potential air temperature and humidity

These variables are assumed to be constant with height and the values at the lower (0m) and upper (2500m) boundaries of the profile are taken from the next higher or lower height level for which the user has provided data.

## 7. Preprocessing the data

The meteorological data normally available from measurements or mesoscale models includes the diurnal variation of temperature, wind speed, wind direction and humidity. If radio soundings or a mesoscale simulation are used, a height profile for these variables is available, but the data has to be manually preprocessed in most cases. The two major problems are the different vertical resolutions of the data compared to the vertical spacing of ENVI-met and different wind directions in different height levels.

To facilitate working with ENVI-met, this extrapolation from measured to model height is automatically done by ENVI-met using a linear interpolation for temperature and specific humidity and a logarithmic interpolation for wind speed. Therefore no further preprocessing of the data is necessary in this case.

Differing wind directions at different height levels are mainly problematic because the inflow boundaries of the model area are defined once for the whole area and not every single height level. Furthermore, a large wind shear increases the risk of numerical instability occurring during the simulation. For these reasons, the wind direction is assumed to be the same from ground level up to 2500m above ground. In most cases the effect of this simplification on the results within the 3D model area, which usually has a height of less than 200m above ground, are thought to be negligible.

## 8. Forcing simulations

If ENVI-met finds a Forcing section in the configuration file, it reads the whole file and saves all variables into arrays. At startup, as well as during the simulation, it checks between which forcing steps the simulation is at the moment, interpolates the values accordingly - temporally and spatially - and writes the values into the 1D-profile of the inflow (Figure 2). A linear interpolation between time steps is used for all variables:

$$\phi_t = \phi_{t1} + (\phi_{t2} - \phi_{t1}) * ((t - t1)/(t2 - t1))$$

with  $t$  being the current simulated time,  $t1$  and  $t2$  the previous/ next time step for which data is provided and  $\phi$  being the variable at the respective time steps.

The vertical interpolation for potential temperature and specific humidity is also linear, while wind speed is interpolated logarithmically.

The values from the 1D profiles are then copied into the cells at the inflow boundaries of the model area. The same 1D profile is used for all cells so that the meteorological conditions are the same at all cells of the inflow boundaries. Due to the small extent ( $\leq 1\text{km}$ ) of typical model areas simulated with ENVI-met this is thought to be a realistic approach. Future versions of ENVI-met might incorporate the possibility to apply different profiles for different sections of the inflow boundaries.

Due to the linear temporal interpolation, the time step between forcings should not be chosen too big (i.e. larger than one hours) if smooth (realistic) diurnal profiles for the forced variables are desired.

As per default settings ENVI-met updates the wind field every 900 seconds of simulated time. In order to avoid numerical instability because of sudden big changes in wind speed and wind direction at the inflow boundary, ENVI-met decreases this time step automatically so that the change in wind direction is smaller than  $1^\circ$  per time step. As every calculation of the flow field takes up a considerable amount of computing time the lowest possible time step is set to 60s and it is reset to higher values as soon as possible, with an upper limit of 900s.

## **9. Case studies**

### **9.1. Setup**

For this case study two areas within the city of Freiburg im Breisgau in South West Germany were selected. Meteorological measurements in these areas were conducted within the scope of the KLIMES project.

Model area 1 is a street canyon near the city center in which measurements took place over a period of 24 hours, starting on May 24th 2007 at 08:00 CET (UTC+1).

Model area 2 deals with Vauban, a quarter in Freiburg which is situated about 3km south of the city center. Measurements there took place on July 15th 2007 during daylight and include additional hourly measurements at four points within the quarter. For this study the time between 09:00 and 18:00 CET was analyzed.

### **9.2. Model areas**

Both model areas presented in this study were digitized by using aerial photos and pictures taken at ground level. The height of the buildings was mainly estimated from these pictures and the number of levels of the buildings. Considering the horizontal and vertical model resolution of 2m, the results obtained by this approach are believed to be sufficiently accurate.

### **9.3. Model area 1: Erbprinzenstrasse**

The model area Erbprinzenstrasse is situated just South West of the city center of Freiburg im Breisgau. The extent of the simulated area was limited to  $186 \times 118 \times 25$  grids with a resolution of  $2 \times 2 \times 2\text{m}$  per grid cell. To the south, the area is confined by

the river Dreisam. All other borders were selected so that a realistic wind flow at the measurement site is guaranteed. The measurement station was situated on a southerly exposed pavement in front of a building (figure 3).

The street axis is orientated in nearly east-west-direction ( $97^\circ$ ) and the measured relation of height to width (H/W) of the urban canyon is 1.09. Due to the block structure of the model, the facades of the houses along the canyon are strictly orientated northward and southward. The canyon has a width of 12m and the house north of the measuring station a height of 12m, the house on the other side of the street a height of 14m, resulting in a H/W of 1.16 in the model.



Figure 3: Model area Erbprinzenstrasse (372 x 236m). Buildings (grey), vegetation (green) and surface materials color coded. Red dot: measurement site.

#### 9.4. Model area 2: Vauban

The Model area Vauban has an extent of 256x197x25 Grids, with a resolution of 2x2x2m. In order to minimize problems arising from the rectangular grid of the model, the whole area was rotated  $20^\circ$  out of the north, so that most facades are aligned parallel to the grid structure (figure 4).

The borders of the model area were chosen in a way to allow realistic wind flow within the core model - westerly winds assumed. The building height is ranging from 4m to 28m with the majority of buildings between 10m and 14m height.

The stationary measurement station was set up at a northward orientated sidewalk (point 1 in figure 5). Additional mobile measurements were made at four points (point 2-5 in Figure 5) in the vicinity, once every hour.





Figure 4: Model area Vauban (512 x 386m). Buildings (grey), vegetation (green) and surface materials color coded.

## 9.5. Input data

The necessary 1D-profile for the atmospheric boundary conditions was created with data from the Meteorological Urban climate Station in Freiburg, which is located on top of a 13 story building at 51.3 m above ground, about 1 km north of the city center. This input data is not ideally suited for forcing, as the vertical profile for all variables has to be deduced by making the assumptions mentioned before. Furthermore the wind measurements are influenced by the turbulence created by the building itself. For short wave radiation only the global value is provided. This value was split into direct and diffuse radiation with the fixed - arbitrary - ratio of four to one.

This kind of data (i.e. measurements at one height level from a station that is not ideally positioned relative to the model area) is often the only data available for such simulations and the following discussion of the result will show how much can be expected from it.

## 9.6. Simulations

ENVI-met was run on an Intel Core2Duo running at 3GHz with 2GB of Ram on which the simulations took about 240 hours for the model area Erbprinzenstrasse and about 300 hours for the model area Vauban.



Figure 5: Positions of stationary (1) and mobile (2-5) measurement sites within model area

## 10. Results

For the evaluation of the model, the main output parameters of ENVI-met, i.e. air temperature  $T$ , wind speed  $\mathbf{u}$ , relative humidity  $f_{rel}$  and mean radiant temperature  $T_{mrt}$  (as a measure for the radiation budget), are compared to the measurements. Furthermore, the human thermal comfort index PET (physiologically equivalent temperature), which is derived from these variables, is also used for the comparison of measurements and simulation in this study.

### 10.1. Erbprinzenstrasse

The comparison of the measurements to the simulations (Fig. 6) shows a good accordance during day time (8-20CET). During the night time (20-8CET) however, the simulated values for wind speed, air temperature and relative humidity show a considerably larger aberration. It appears that the measurements from the weather station at 53m above ground are not suitable as input during the night, as atmospheric events at ground level seem to be uncoupled from the events in this height.

As the wind direction changes from westwards to eastwards during the evening this event is possibly linked to a local wind system that only affects the lowest 50m of the atmosphere and has its source in the valleys of the black forest which is situated east of Freiburg. Therefore the assumptions made for the input profile, i.e. a neutral stratification of the atmosphere, a logarithmic wind profile and constant relative humidity, are not valid in this case and ENVI-met cannot reproduce the results of the measurement. Thus only the data from 8:00CET to 20:00CET will be analyzed in the following discussion.

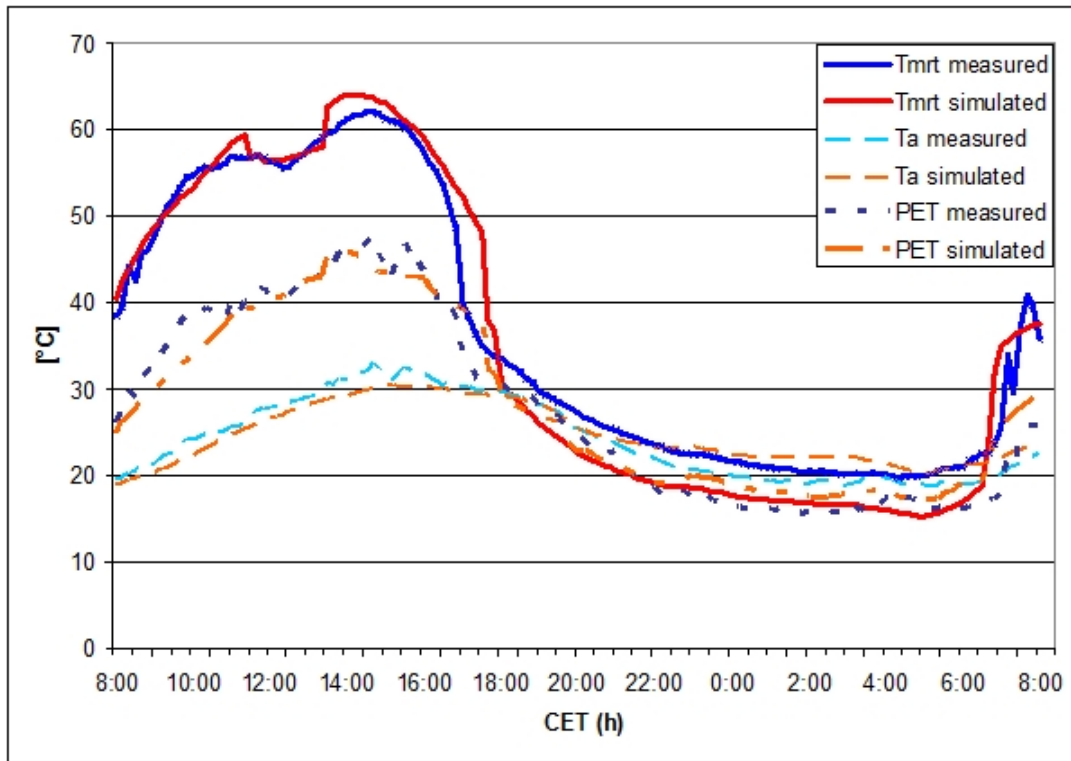


Figure 6: Comparison between measured and simulated air temperature  $T_a$ , Mean radiant temperature  $T_{mrt}$  and PET in 2m above ground level, May 24th 2007.

### 10.1.1. Mean radiant temperature

Due to the block structure of the model environment and the spacing of the radiation sensors used in the measurements, the average radiation temperature of two neighboring grid cells was taken.

From morning till early afternoon (16:40 CET), the simulated values and measurements are in good accordance with a maximum total deviation of  $3.41^{\circ}\text{C}$ , which equates a relative aberration of 5.4%, at 13:40 CET (figure 6).

This maximum difference at noon, as well as the delayed decrease of the radiative temperature in the evening of about 40 minutes, can be explained by the relatively coarse resolution and cubic nature of the model and uncertainties in the height of the buildings to the west of the measurement point, both leading to uncertainties in the calculation of shadows.

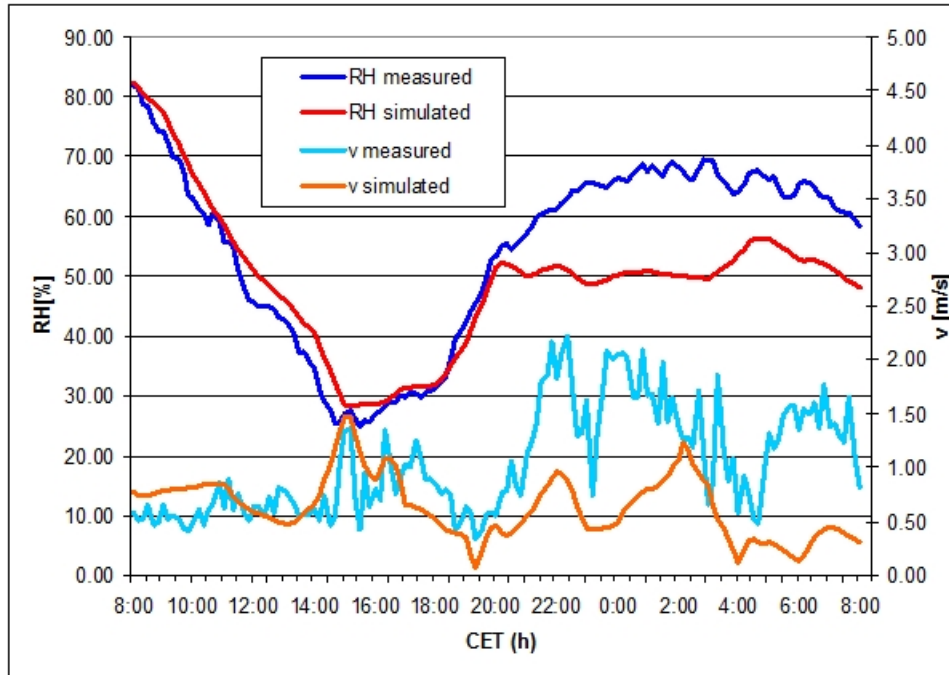


Figure 7: Comparison between measured and simulated relative humidity RH and wind speed  $v$  in 2m above ground level, May 24th 2007.

### 10.1.2. Wind speed

The measured wind speed shows much more turbulence than the simulated one (figure 7), as can be expected since the input data is based on hourly means and the turbulence within a street canyon is normally higher than in 53m above ground. The maximum deviation between measured and simulated wind speed during the day is  $0.6\text{ms}^{-1}$  and the root mean squared error  $0.28\text{ms}^{-1}$ .

### 10.1.3. Temperature and relative humidity

The simulated values are in good accordance with the measurements with a maximum difference of  $2.9^{\circ}\text{C}$  at 14:40 CET for air temperature and 7.4% at 14:10 CET for relative humidity (figure 7). The measured air temperature is at nearly all times higher than the simulated one, and the simulated relative humidity, as a consequence, at nearly all times higher than the measured one. This systematic aberration can be explained by the assumption made for the boundary conditions, i.e. a neutrally stratified atmosphere, which is not valid for a summer day with strong radiative input.

#### 10.1.4. Physiologically equivalent temperature

As PET is derived from the parameters mentioned above, calculating the energy fluxes of the human body, the simulated values also shows a good concordance with those derived from the measurements (figure 6). The big deviation in the evening can be explained by the difference in radiative temperature due to coarse the block structure of the model area and the uncertainties about building height. The deviations from 8 CET to 10:00 CET can be explained by the difference in wind speed, which is overestimated by 50% at this point of the simulation (Fig. 7).

Table 1: Root mean squared error of compared variables for different spans of time at survey area Erbprinzenstrasse

	root mean squared error		
	8-8 CET	8-20 CET	20-8 CET
v [m/s]	0.7	0.3	0.9
$T_a$ [°C]	1.7	1.2	2.1
RH [%]	9.7	3.5	13.3
$T_{mrt}$ [°C]	4.0	3.8	4.2
PET [°C]	2.4	2.5	2.4

#### 10.2. Vauban

For the second model area, Vauban, the comparison between measurements and simulated values shows a good accordance for wind speed (tab. 2) for the stationary measurement station. Unfortunately there are no reliable recordings of wind speed for the four points at which the hourly measurements took place. The simulated values for air temperature are also in good agreement with the measurements at all four points.

As for the relative humidity, the simulated values are considerably higher than the measured ones, indicating that the assumption made for the input profiles of the simulation, i.e. a constant relative humidity throughout the height of the 3D model, is not suitable for the simulation of a cloudless summer day. Furthermore local effects like the advection of more humid air in this part of town could be responsible for the great aberrations.

The deviations of the mean radiant temperature can be explained by the grid structure of the model and the fixed splitting of the global incoming short wave radiation into a direct and diffuse component.

### 11. Discussion

The comparison between measurements and the results of the simulations performed with ENVI-met show that the model output strongly depends on the quality of the data used for the forcing, i.e. the creation of the boundary conditions of the model. In the presented case studies the 1D input profiles of air temperature, wind speed and direction

Table 2: Root mean squared error for selected variables at measurement points in model are Vauban

	<b>root mean squared error</b>				
	stationary	mobile 1	mobile 2	mobile 3	mobile 4
$v$ [m/s]	0.2	-	-	-	-
$T_a$ [°C]	1.1	0.86	1.1	1.2	1.7
RH [%]	9.5	8.9	9.3	11	7.8
$T_{mrt}$ [°C]	5.0	3.7	3.9	4.2	4.2
PET [°C]	3.1	-	-	-	-

and specific humidity are derived from the measurements of a weather station on top of a building, 53m above ground and 1km, respectively 3km north of the model areas.

As the model results show, the assumptions made for the profiles, namely a neutrally stratified atmosphere with a logarithmic wind profile and constant relative humidity, are only suitable in special cases and can lead to large aberrations between measurements and simulations, especially if local wind systems are involved.

The deviation of the simulated radiative temperature from the measured one can mostly be explained by the cubic grid structure and the relatively coarse grid resolution of the model area, resulting in inaccuracies of the shading. As only cloudless days were simulated, the simulated incoming long wave radiation, which is calculated by ENVI-met from the temperature and water content of the air, is in good accordance with the measurements. The fixed splitting of the global short wave radiation into direct and diffuse short wave radiation by the arbitrary ratio of four to one also provides reasonably accurate results for short wave radiation fluxes.

## 12. Conclusion

The simulations show that the new forcing function of ENVI-met can produce reasonable results and enables the user to derive the microclimate within urban areas by using data from a single measurement point or from a mesoscale numerical simulation. As the model output of a micro scale climate model like ENVI-met strongly depends on the input, i.e. the boundary conditions, the quality of this input data is very important. For best results, the site where the data for the creation of the forcing profiles is collected should be close to the model area and free from influences of local structures, terrain and vegetation.

As users of ENVI-met are predominantly interested in the atmospheric conditions near ground level it is not necessary to get a detailed profile of the atmospheric conditions. As the case studies have shown one measurement point in combination with the assumptions used by ENVI-met suffice to get usable results. Ideally the measurement point should be closer to the ground than in this case study.

The data used for creating the inflow profiles has, in most cases, to be preprocessed, i.e. be smoothed in order to avoid numerical instabilities and get suitable results. This is

especially true for wind speed and wind direction.

Within the joint research project KLIMES the Forcing was used to validate the model with the point measurements made in the summer of 2007 and 2008. As shown in this study, the model validation can be considered successful, especially if the quality of the input data is taken into account.

The new forcing function of ENVI-met not only allows to compare simulations with measurements, it also enables the user to create specific weather scenarios, e.g. for research on climate change. Within the KLIMES project several such scenarios were simulated (see chapter V).

As of 2011 the forcing feature has also been used in a joint project with the Deutscher Wetterdienst in which ENVI-met was coupled with MUKLIMO\_3 [Sievers, 1995] in a one-way nesting. First results were very promising and future collaboration on this topic is planned.

## References

- O. Christensen, J. Christensen, B. Machehauer, and M. Botzet. Very high-resolution regional climate simulations over scandinavia - present climate. *Journal of Climate*, 11(12):3204–3229, 1998.
- B. Denis, R. Laprise, D. Caya, and J. Côté. Downscaling ability of one-way nested regional climate models: the big-brother experiment. *Climate Dynamics*, 18:627–646, 2002.
- J. Dudhia, D. Gill, K. Manning, W. Wang, and C. Bruyere. Psu/ncar mesoscale modeling system tutorial class notes and users' guide (mm5 modeling system version 3), 2005. URL <http://www.mmm.ucar.edu/mm5/documents/tutorial-v3-notes-pdf/mm5.pdf>. Retrieved 20 May 2011.
- F. Giorgi and G. Bates. The climatological skill of a regional model over complex terrain. *Monthly Weather Review*, 117(11):2325–2347, 1989.
- Y. Ji and A. Vernekar. Simulation of the asian summer monsoons of 1987 and 1988 with a regional model nested in a global gcm. *Journal of Climate*, 10(8):1965–1979, 1997.
- H. Mayer, J. Holst, P Dostal, F. Imbery, and D. Schindler. Human thermal comfort within an urban street canyon in central europe. *Meteorologische Zeitschrift*, 17(3):241–250, 2008.
- C.-H. Moeng, J. Dudhia, J. Klemp, and P. Sullivan. Examining two-way grid nesting for large eddy simulation of the pbl using the wrf model. *Monthly Weather Review*, 135(6):2295–2311, 2007.
- K. Schlünzen. Validierung hochauflösender regionalmodelle. *Berichte aus dem Zentrum für Meeres- und Klimaforschung*, (23), 1996.
- U. Sievers. Verallgemeinerung der stromfunktionsmethode auf drei dimensionen. *Meteorologische Zeitschrift*, 4:3–15, 1995.
- A. Staniforth. Regional modeling: a theoretical discussion. *Meteorol. Atmos. Phys.*, (63):15–29, 1997.
- T. Warner, R. Peterson, and R. Treadon. A tutorial on lateral boundary conditions as a basic and potentially serious limitation to regional numerical weather prediction. *Bulletin of the American Meteorological Society*, (78):2599–2617, 1997.
- D. Zhang, H. Chang, N. Seaman, T. Warner, and J. Fritsch. A two-way interactive nesting procedure with variable terrain resolution. *Monthly Weather Review*, 114(7):1330–1339, 1986.



# Part V.

## Simulating the urban microclimate with ENVI-met

### 1. Summary

In this chapter two different approaches of simulating the urban microclimate and assessing the impact of urban planning on the human thermal thermal comfort are shown:

- simulating existing/ planned urban quarters in order to asses their microclimatic performance and propose improvements concerning the urban design.
- simulating synthetic structures in order to develop general guidelines and concepts.

The first section of this chapter concentrates on simulations of real urban quarters with ENVI-met. These simulations were performed in the framework of the joint research project KLIMES and focus on the biometeorological performance of different urban structures which are typical for central European cities. The goal of these simulations was to identify those elements that intensify or mitigate the effect of the urban heat island (UHI). The simulations show that open spaces that allow wind flow and feature canopied vegetation are able to mitigate the thermal stress in an urban quarter while areas with high building density and little vegetation are most prone to high levels of heat stress.

The second part of this section deals with the simulation of a synthetic street canyon. The effects of different facade materials, ground surfaces, vegetation densities and galleries on microclimate within a street canyon during a hot summer day are assessed.

The results of this second set of simulations show that all measures only have moderate influence on the air temperature within the canyon but that some of these measures can greatly influence human thermal comfort by modulating the radiative budget of a human body within the street canyon. Of all investigated measures the blocking of incoming solar radiation by means of trees with a dense crown layer or by galleries provides the most agreeable biometeorological conditions within the street canyon. The comparison of different facade materials show that the human thermal comfort within the street canyon has to be weighed against the energy budget of buildings.

In both cases the human thermal comfort is evaluated by the use of the physiologically equivalent temperature PET.

## 2. Simulating the impact of global warming on the summerly urban microclimate in Central Europe

### 2.1. Introduction

The simulations discussed in the following section are the result of the joint research project KLIMES which took place between 2006 and 2009. Goal of the project was to analyze the human thermal comfort in central European cities during extended heat periods. Due to global warming such summerly heat waves are expected to occur more often and be longer lasting in the future [Jacob et al., 2008]. The study focused on several quarters in Freiburg, a city in South-West Germany that is known for its relatively warm climate. Within the project several measurement campaigns were conducted in combination with interviews of passerbys about their thermal sensation.

The simulations performed with ENVI-met within the scope of this project had the goal to identify the influence of certain typical urban structures on the urban microclimate and to develop possible strategies to mitigate heat stress within these structures.

As ENVI-met is not capable of simulating a whole city but rather single urban quarters four such urban quarters were selected for the subsequent simulations. These quarters represent different types of urban residential areas that are thought to be typical for central European cities. The microclimate of these model areas was then simulated with the boundary conditions of an extreme heat scenario which will consequently be referred to as worst case scenario: a summer day at the end of a longer lasting heat period with a maximum air temperature of over 35°C and a maximum solar irradiation.

### 2.2. Model areas

A total of four different model areas within the city of Freiburg were selected (fig. 1). Each of these areas represents an urban structure that can typically found in Central European cities:

- Wiehre is a central district of Freiburg with many buildings dating back from the 19th century.
- Weingarten is a residential area with relatively high buildings that were built in the 1960s.
- Rieselfeld is a newly developed quarter at the outskirts of the city.
- Vauban is a recently developed eco-friendly model district that was developed with special consideration to sustainable buildings and car free transportation.

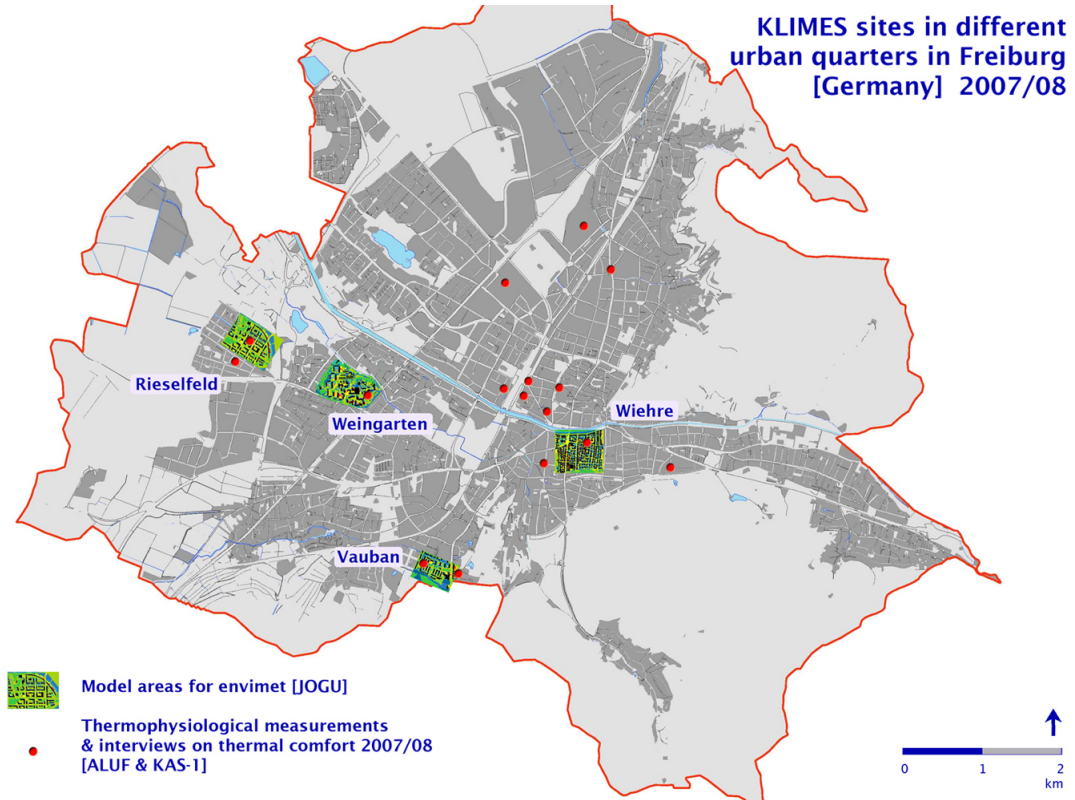


Figure 1: Map of Freiburg with simulated model areas and measurement sites

The model areas were created with the help of layout plans, aerial images and photos taken on site. The layout plans were used to define the outlines and height of the buildings. As these layout plans were partly outdated newer buildings were created by only using the information gained from aerial photos and photos taken on site. These photos were also used to model the ground surface and the vegetation within the quarters. The errors made by using this relatively inaccurate method of digitalization are believed to be smaller than the model resolution of  $>2\text{m}$ .

The version of ENVI-met used for these simulations is limited to about 3 million grid cells. The vertical and horizontal resolution of the model grid was set to the smallest possible values allowed by this constraint (tab. 1). In the following the results of only

Table 1: Size and resolution of the model areas (Note: model Wiehre has a telescoping vertical grid)

	size [cells]	resolution [m]	size [m]
Rieselfeld	$300 * \times 216 \times 30$	$2.5 \times 2.5 \times 2.5$	$750 \times 540 \times 75$
Vauban	$256 \times 197 \times 25$	$2.0 \times 2.0 \times 2.0$	$512 \times 394 \times 50$
Weingarten	$300 \times 230 \times 30$	$3.0 \times 3.0 \times 3.0$	$900 \times 690 \times 90$
Wiehre	$294 \times 262 \times 25$	$2.5 \times 2.5 \times 1.0$	$735 \times 655 \times 100$

two of these model areas - the model areas Vauban and Wiehre - are discussed in detail.

### **2.3. Model area Vauban**

The residential area Vauban is a relatively new quarter that has been designed as an eco-friendly model quarter with energy efficient buildings and a high portion of vegetation.

The buildings within the model area are mainly orientated along the north-south axis and have an average height of 12m. In the northern part of the model area there are many old trees with a dense crown and heights of 20m that are situated among the houses. A similarly dense crown layer can also be found at the southern border of the model area where the trees are situated along a small creek in a non built-up area (fig. 2).

In the middle of the model area the main street of the quarter, the Vaubanallee, runs from east to west. Next to the street there are tracks for the streetcar. Together with the sidewalk this provides an air supply corridor of about 20m width that runs roughly along the west-east axis.

At the east the model area is confined by a large building block with a height of 14-20m that runs in north-south direction. In the western direction the quarter continues for another approximately 400m with the same mix of buildings and vegetation that can be found in the center of the modeled area.

### **2.4. Model area Wiehre**

The quarter Wiehre is a popular housing area a short distance south of the city center. The area features a high percentage of old buildings, many of them in Wilhelminian style, dating from the late 19th century. Similarly structured quarters can be found in many central European cities. A representative section of this quarter was selected as model area.

The river Dreisam provides the only natural border at the northern part of the model areas. At all other model areas the quarter continues uninterrupted for another few hundred meters.

The majority of the buildings within the model area consists of apartment buildings with four to five floors. The streets are roughly orientated along the cardinal directions. The vegetation within the quarter is not evenly distributed, especially regarding trees within the streets. While only a few trees are situated along Günthertalstraße, and nearly none along Talstraße, other streets running parallel to them like Turmseestraße and Urachstraße are densely planted with tall, mostly deciduous, trees (fig. 3). This allows a direct evaluation of the effect of trees within road space on the human thermal comfort on street level.



Figure 2: Map of quarter Vauban.

## 2.5. Boundary conditions

The boundary conditions were created by using measurements of air temperature from the summer of 2003 when an exceptionally intense and long lasting heat wave struck central Europe in the beginning of August [Rebetez et al., 2006]. In order to create a real worst case scenario the date for the simulation was set to a cloudless June 21. with low wind speed (0.5m/s in 10m above ground). With this setup the irradiation during the simulated day is at a maximum while there is also only very little cooling by wind. The wind direction was set to west.

The soil temperature and relative humidity were also set to values that simulate dried up soils after a longer lasting heat period. The initial temperature of the soils is set to 25°C for the upper (0-20cm) and lowest (>50cm) layers and to 26°C for the middle (20-50cm) layer. The initial relative humidity is set to 10% for all three layers.

The start time of the simulation was set to 7CET, the end time to 22CET. In the following discussion only the results from 8CET onwards, i.e. one hour after initialization, are considered.



Figure 3: Map of quarter Wiehre.

## 2.6. Simulations

The highest values of the human thermal comfort index PET are reached at 14 CET, while the highest values for air temperature can be found at 16CET. The reason for this 2h discrepancy is that PET is strongly influenced by solar irradiation which has its peak value between 13 and 14 CET.

Due to the extreme boundary conditions even the lowest PET values found within the model areas are, for most part of the simulation above 23°C , a threshold above which heat stress is considered to start [Matzarakis and Mayer, 1996].

### 2.6.1. Results Vauban

Within the model area there are several areas that have an above average PET during the whole simulation. One of these areas is the market place (Alfred Döblin Platz [fig. 2]). The high PET values at the market square can be explained by two factors: the

building at the western border efficiently blocks the westerly wind, especially at the western side of the square, and a highly reflective surface layer in combination with no shading increases the radiation budget of the human standing on the square. At the east and north the square is surrounded by large deciduous trees with a distinct crown layer, but the center of the square is without any shading for most of the day.

At 14 CET the distribution of PET within the quarter shows, as expected, a strong correlation to the solar irradiation (shading) and wind speed (fig. 5). There is no apparent correlation between the soil type - i.e. natural unsealed or artificial, sealed surfaces - and PET. The dried up natural soils have roughly the same albedo as paved surfaces and also the same surface temperatures (fig. 4).

At 22 CET, 1.5 hours after sunset, the PET values shows a strong correlation to the surface type (fig. 6). The surface temperatures of the natural soils are now below those of the paved surfaces and therefore emit less long wave radiation and transfer less sensible heat to the air above them (fig. 4). Thus the small parks within the model area only act as cooling zones after sunset - if they are not regularly irrigated.

The areas with the highest PET values at 22 CET can be found below the trees and below the overhanging buildings along the south side of Vauban Allee. These elements which provide shading during the day now provide an additional source of long wave radiation, thereby increasing the radiation budget of a human standing beneath them. However at 22CET even the maximum PET values are not in a critical range anymore.

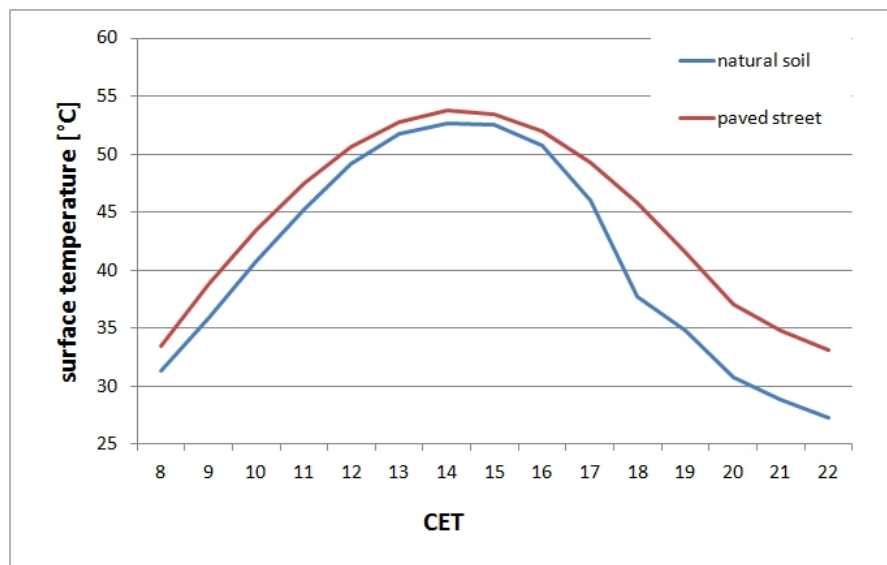


Figure 4: Diurnal variation of the surface temperature of natural soil (grid 101,91) compared to surface temperature of a paved street (grid 97,119).

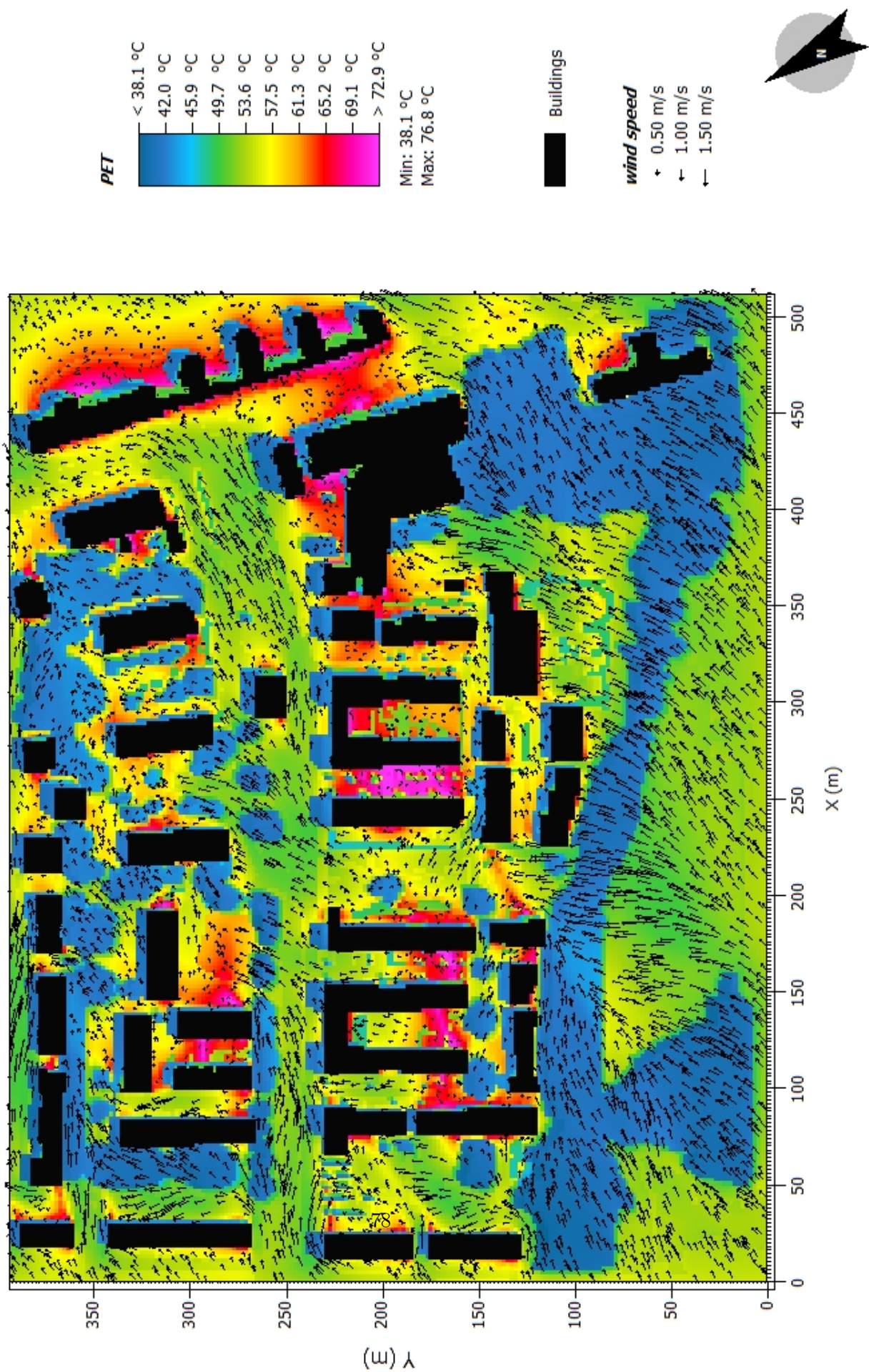


Figure 5: PET and wind speed at 14CET in 1.8m above ground in model area Vauban.



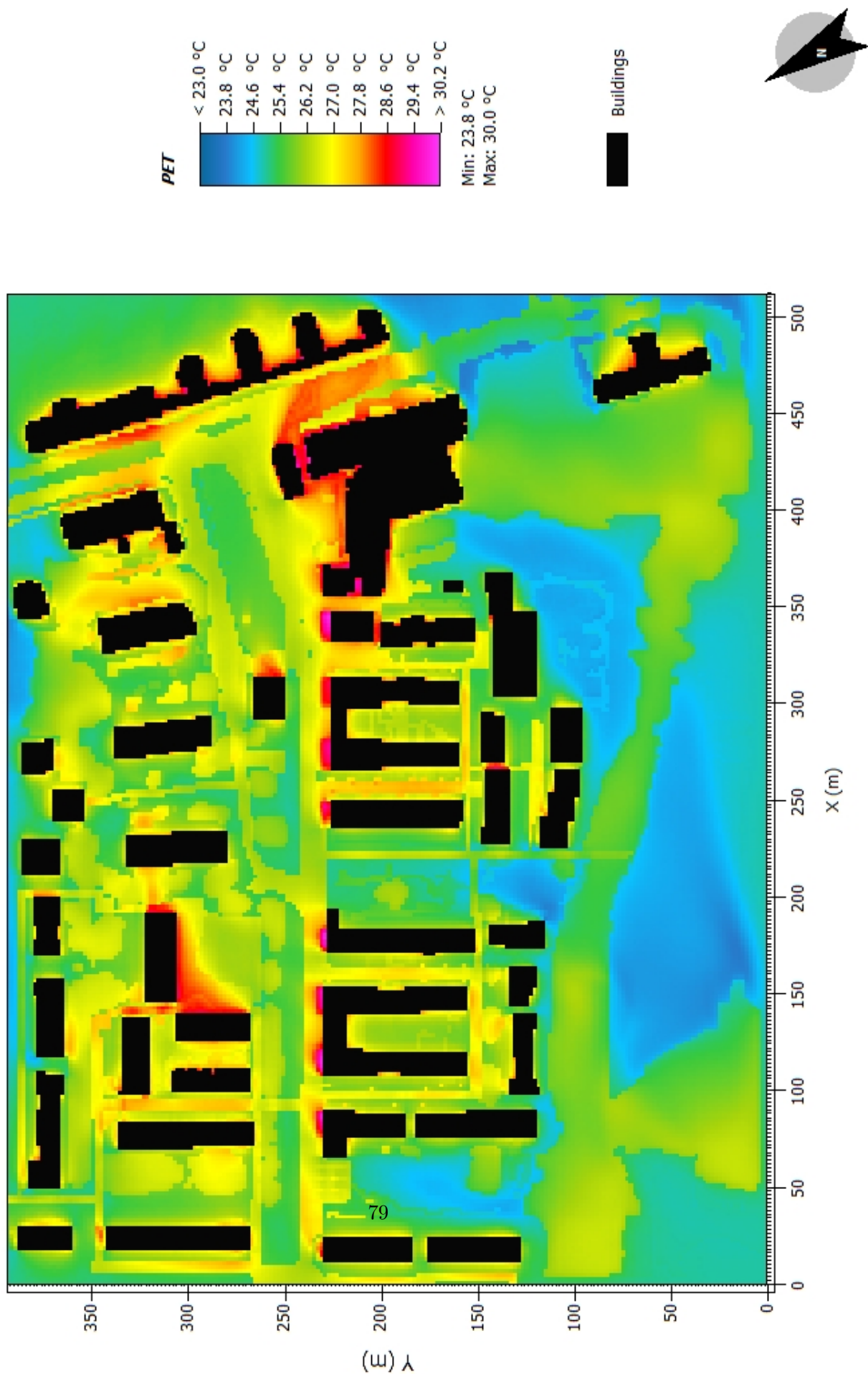


Figure 6: PET at 22CET in 1.8m above ground in model area Vauban.

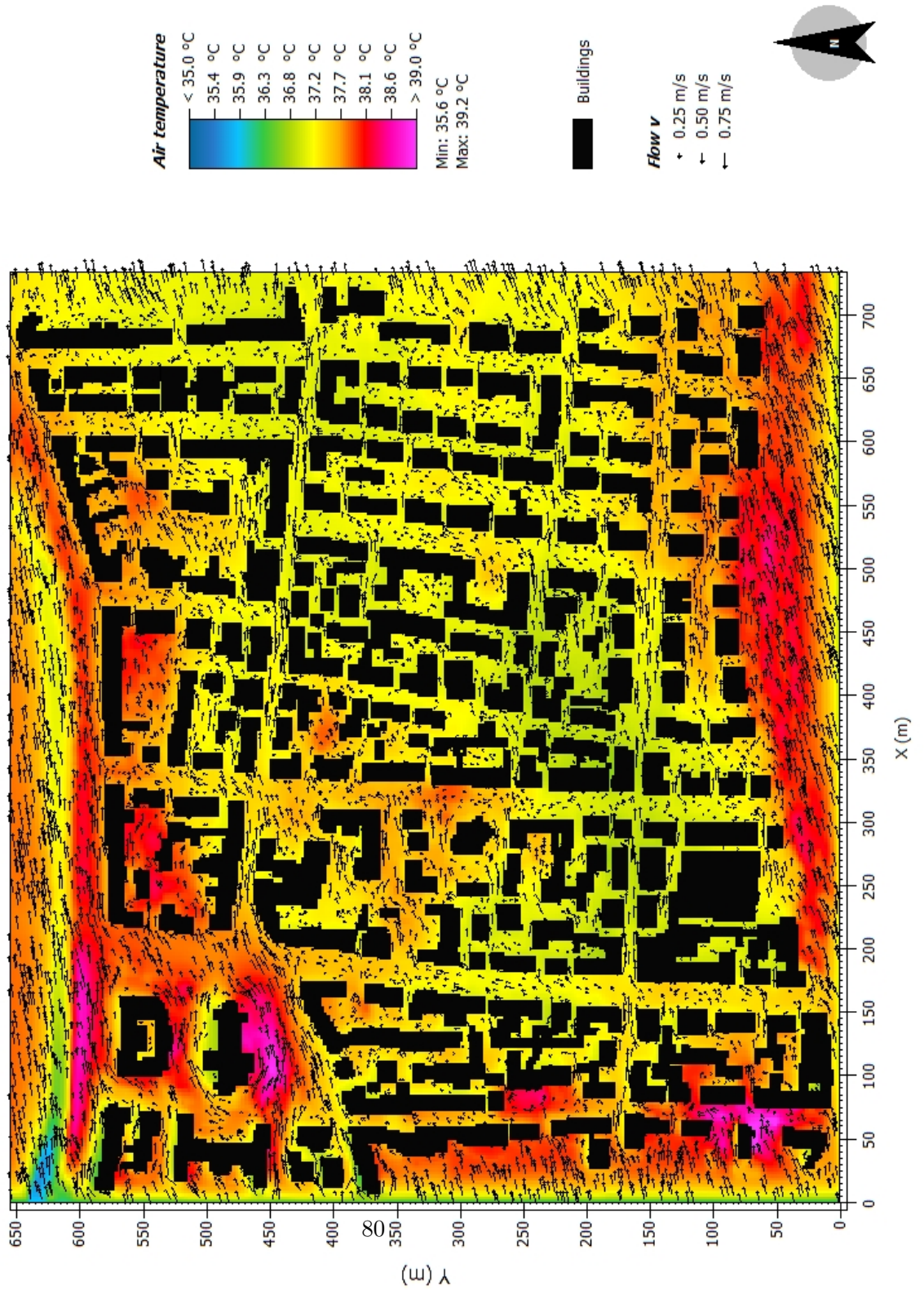


Figure 7: Air temperature and wind speed in 1.5m above ground at 14CET in model area Wiehre.



Figure 8: PET in 1.5m above ground at 14CET in model area Wiehre.

### 2.6.2. Results Wiehre

Due to the high building density the wind speed within the model area is generally very low near ground level. In the center of the model area only the streets that run in a west-east direction, like Talstraße and Erwinstraße, feature wind speeds above  $0.5\text{m}\cdot\text{s}^{-1}$ . The west wind is channeled into these streets (fig. 7).

The comparison between air temperature (fig. 7) and PET (fig. 8) shows no visible correlation between the two variables. At this time of day the human thermal comfort is mainly defined by the mean radiant temperature and wind speed. The impact of the differences in air temperature within the model area ( $3.6^{\circ}\text{C}$ ) do not have the same scale as the impact of these parameters on human thermal comfort. This effect is best visible at the square south of the church at the crossing of Talstraße and Günthertalstraße. The air temperature in this area is above  $38^{\circ}\text{C}$ . But due to the relatively high wind speeds and the shading provided by large trees, this area does not show an above average PET. Only a small region in the slipstream of the church and without shading shows a very high PET value of  $64^{\circ}\text{C}$ .

Like in the model area Vauban the areas with little wind speed and no shading show the highest levels of thermal stress with PET values of  $70^{\circ}\text{C}$  and above.

### 2.7. General discussion and Conclusion

Albeit the different structure of both model areas they show very similar results concerning the relevant meteorological variables.

Local cooling or heating of air near ground level can mainly be attributed to differences in surface shading and surface materials. Impervious surfaces like paved roads or sidewalks convert most of the absorbed radiative energy into sensible heat while moist natural surfaces convert a part of the absorbed radiative energy into latent heat, thus not directly heating the air parcel above but releasing moisture into the air [Oke, 1982]. If a natural soil is not irrigated regularly during periods without precipitation and dries up, natural soils act like impervious surfaces, converting almost all of the absorbed radiative energy into sensible heat. Furthermore dried up natural soils have a lower heat transfer coefficient than wet natural soils. This decreases the vertical energy flow and leads to higher surface temperatures. But at the same time the surface albedo is decreased [Idso et al., 1974], i.e. less radiative energy is absorbed by the soil. As a consequence the surface of the dried up natural soils in the worst case scenario heats up to about the same maximum temperature as asphalt surfaces.

In both scenarios the differences in air temperature in 1.8m above ground level within the model area can reach up to  $5^{\circ}\text{C}$  within a few hundred meters. In the 'normal' scenarios the air temperature in 1.8m above ground shows a distinct association with the distribution of natural soils and vegetation. The air temperature has the lowest values in shaded areas with natural soils while the highest values can be observed over streets that are fully exposed to the sun. In the worst case scenario this pattern is no longer this clearly visible. Zones with above-average air temperature can now also be found in

areas with natural soils.

Regarding the comfort index PET the simulations show a distinguished correlation of PET with the spatial distribution of vegetation and building density. A low building density results in an unblocked wind flow through the quarter. the consequently higher wind speeds result in lower PET values. A high vegetation density also blocks the wind but to a lesser extent than the buildings. Furthermore the shading provided by vegetation, especially by trees with a high dense crown layer, effectively lowers the radiation budget in its vicinity and results in the lowest PET values within the whole model area. As expected the PET values for the worst case scenario are generally higher than those for the 'normal' scenario. The increase over areas with natural soils is above average. This can be attributed to the above mentioned increase in air temperature and radiative budget due to the decreased soil water content.

All simulations show the same results: a relatively undisturbed air flow and a high density of vegetation with a distinct and dense crown layer can significantly ameliorate the summerly human thermal comfort. For several reasons there it is however not possible to give generalized recommendations for urban planning:

- PET is a static index. This means that PET - like most other indices for human thermal comfort - calculates the human physiological reactions until a steady state is reached. For this to be the case in reality the human would have to stand in the same spot for a prolonged period of time - or walk through an area with the same micro-meteorological conditions for a longer time. As any microclimate simulation of an urban quarter will show wind speed and radiative budget, two of the meteorological parameters that define human thermal comfort show large variations over small distances. To a lesser degree this is also true for air temperature and also specific humidity. As a consequence the energy balance of a person moving through an urban space only rarely reaches a steady state condition. Thus not the size of the areas with high PET values is crucial for a realistic evaluation of the thermal comfort within an urban area, but rather the distribution of PET values along the most frequent pathways through and within the area. The multi-agent botworld [Bruse, 2007] solves this problem by not calculating a static index but rather calculating the energy balance and physiological reactions of a bot (simulated person) moving through the area. By combining the calculated assessments of several hundreds of these bots it is possible to assess the thermal perception of an urban quarter from an inhabitants point of view.
- In this study only the summerly human thermal comfort in Central Europe is considered. In order to mitigate heat stress on a hot summer day a high wind speed and shading are desired. In spring or fall however the same measures that ameliorate human thermal comfort in summer may have a negative impact. In central Europe deciduous trees seem to be the best solution because they automatically adjust their shading according to the seasons. But in countrys closer to the equator

shading provided by buildings may be the better solution [Ali-Toudert and Mayer, 2004].

- Local situations have to be taken into account. Local wind systems or a summerly shortage in water supply have to be taken into account and might impede certain structural actions, like e.g. irrigation, that have a positive effect on summerly thermal comfort.

### **3. Simulating the impact of surface materials, vegetation and overhanging facades on human thermal comfort within a street canyon in Central European summers**

#### **3.1. Introduction**

Urban areas can often be found to be several degrees centigrade warmer than the surrounding rural areas [Oke, 1973]. This difference between urban micro climate and the climate of the surrounding rural areas, commonly referred to as the urban heat island effect, is largely due to the differences in albedo and heat storage capacity between urban artificial structures like pavements or facades on the one side and natural soils and plants on the other side. With climate change becoming reality [Houghton et al., 2001] summerly heat waves in central Europe are expected to become more frequent, intense and longer lasting. With their current layout most central European cities aggravate the negative impacts of summerly heat waves for their inhabitants. It is therefore necessary for architects and urban planners to develop strategies to mitigate the impact of climate change on human thermal comfort within the urban environment.

The following simulations focus on the impact of surface materials, vegetation and galleries on the human thermal comfort within a street canyon. For each setup four simulations, differing in the orientation and layout (H/W) of the street canyon were run. The physical equivalent temperature (PET) is used as a thermal comfort index in order to compare the impact of different layouts of the street canyon on human physiology.

#### **3.2. Model area**

A simple street canyon with a length of 50m and width of 10m and homogeneous, uninterrupted construction on both sides of the canyon was chosen as model area (fig. 9). The geographical position of the model area is set to 7° western longitude and 53° northern latitude.

The horizontal model resolution is 1m, the vertical resolution 2m, with the lowest grid cell divided into five sub grid cells with a height of 0.4m each. This division of the lowest grid cell provides a more accurate simulation of the energy exchange at the ground surface. The width of the sidewalk on both sides of the canyon is 2m, the roadway has a width of 6m. Based on this layout an overall of eleven different canyons was created (tab. 2). The canyons differ in the physical properties of the facades (Canyon 1 - 5), the ground surface (Canyon 8 & 11), vegetation (Canyon 6 & 7) and the existence of galleries (Canyon 6 & 7).

The height of the buildings lining the canyon is set to 10m (HW=1), respectively 20m (H/W=2). In order to check if the orientation of the street canyon has any influence on the general results of the simulations each canyon was modeled once in east-west direction and once in north-south direction.

This results in a total of four different versions of each of the eleven canyons.

Table 2: Overview of modeled canyons

	Absorption [%]	Reflection [%]	Emissivity [%]	Conductivity [W/(mK)]	Thickness [m]	Albedo	Albedo	Vegetation	Overhang
Canyon 1	50	30	90	0.2	0.3	0.4	0.2	-	-
Canyon 2	75	5	90	0.2	0.3	0.4	0.2	-	-
Canyon 3	10	70	90	0.2	0.3	0.4	0.2	-	-
Canyon 4	5	75	5	0.2	0.3	0.4	0.2	-	-
Canyon 5	50	30	90	0.5	0.2	0.4	0.2	-	-
Canyon 6	50	30	90	0.2	0.3	0.4	0.2	intermittent trees (height:15m)	-
Canyon 7	50	30	90	0.2	0.3	0.4	0.2	dense trees (height:15m)	-
Canyon 8	50	30	90	0.2	0.3	0.4	0.5	-	-
Canyon 9	50	30	90	0.2	0.3	0.4	0.2	-	continuous
Canyon 10	50	30	90	0.2	0.3	0.4	0.2	-	intermittent (4m every 4m)
Canyon 11	50	30	90	0.2	0.3	0.2	0.2	-	-



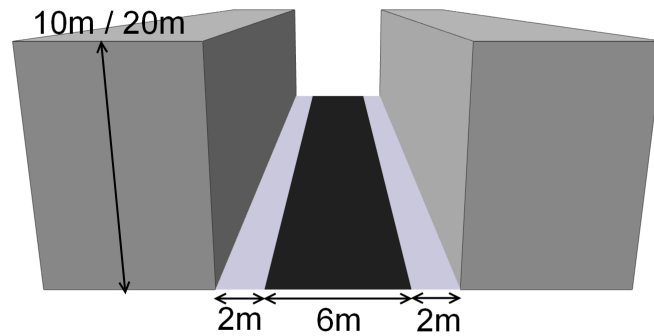


Figure 9: Geometrical layout of the synthetic canyon used in the simulations.

### 3.3. Simulation

The simulations focus on the effect of different measurements on mitigating human thermal discomfort within street canyons on a hot summer day in central Europe. Therefore a worst case scenario has been created, similar to the one used in the previous simulations of the four model areas in Freiburg. A cloudless June 21st has been selected as simulated day, as it is the day with the highest solar input on the northern hemisphere. Wind speed at the inflow boundary is set to  $0.5\text{ms}^{-1}$  at 10m above ground level. The wind is coming from a western direction in all simulations. The air temperature at the inflow boundary follows user defined diurnal variation and reaches up to  $35^{\circ}\text{C}$  in 2m above ground in the afternoon. The specific humidity of the air at the inflow boundary is set to  $10\text{gkg}^{-1}$  within the height of the 3D model domain throughout the whole day. Initialization temperatures for the soil were set to 298K for the upper layer and 299K for the middle and the lower layer. As the soil is sealed at all points within the model area the simulations settings for the relative humidity of the soil only apply to the physiology of the plants. The soil humidity is set to 40% for all layers.

The temperature inside the buildings, which influences the facade surface temperature, is set to a fixed value of  $20^{\circ}\text{C}$ . The simulation starts at 6 CET and runs for 24h.

After the simulation has finished the values for wind speed, air temperature, specific humidity and radiative temperature are used to calculate PET. Because of the vertical structure of the grid this is done at a height of 1.8m above ground instead of the more common 2m above ground. For the physiological parameters of the calculation of PET a 35 year-old male with a weight of  $75\text{kg}$ , a height of 1.75m, a clothing insulation of 0.9 and a work metabolism of 80W is chosen.

### 3.4. Results

In order to compare the impact of the different simulations on human thermal comfort the average PET of the whole street canyon as well as only of the two sidewalks on each side of the street canyon are regarded.

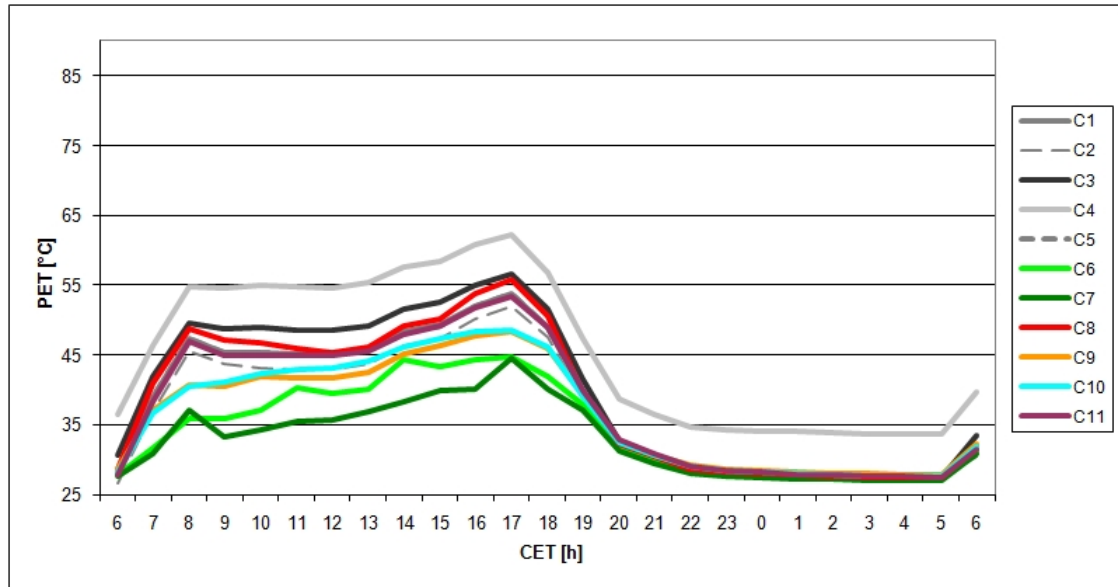


Figure 10: PET in 1.8m above ground averaged over whole street canyon. E-W orientation.  $H/W=1$ .

#### 3.4.1. Influence of orientation and $H/W$ of street canyon

As expected the orientation of the canyon has no influence on the general effect of the different layouts on the human thermal comfort within the canyon (figs. 15 and 17). The highest values of PET for every setup can be observed in the north-south orientated canyons at noon, when the shadows cast by the buildings are at a minimum and solar radiative input is at a maximum.

A higher  $H/W$  causes less direct solar radiation to enter the street canyon and therefore generally leads to lower PET values throughout most of the day. Maximum and average PET values of the whole canyon for  $H/W=2$  are up to  $2.5^{\circ}\text{C}$  lower than for  $H/W=1$ .

#### 3.4.2. Albedo of facades

The albedo of a facade influences the thermal comfort within a street canyon in two different ways:

- A higher albedo effectively reduces the surface temperature of facades by several degrees, thereby reducing the latent heat transfer as well as the emission of infrared

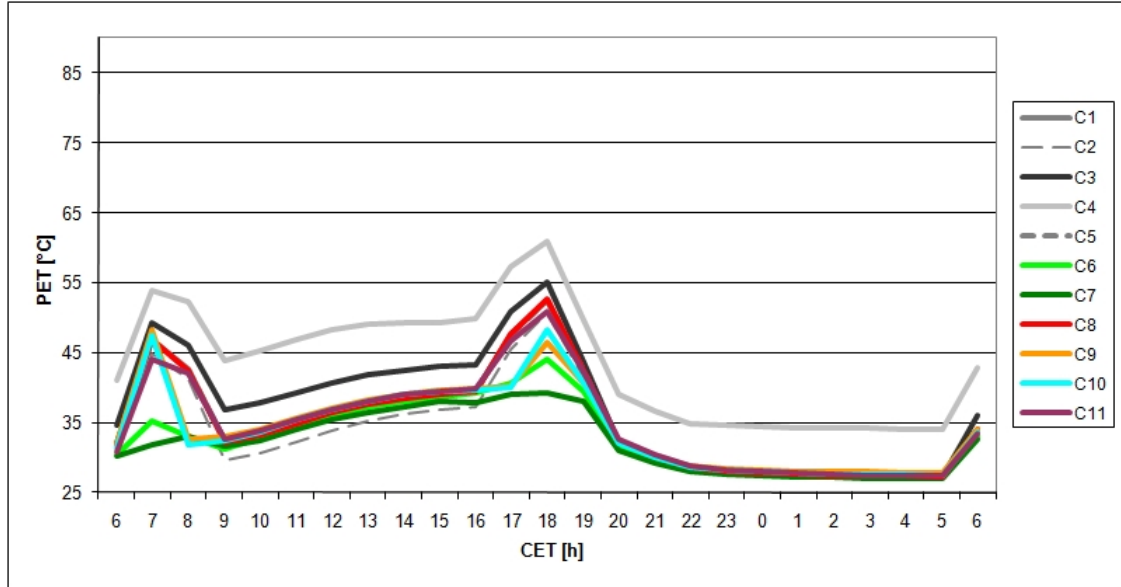


Figure 11: PET in 1.8m above ground averaged over southern pavement. E-W orientation. H/W=1

radiation. Thus a higher albedo leads to a lower air temperature and a lower radiative temperature in its vicinity. The effect of the facade temperature on air temperature of a canyon also strongly depends on the wind speed within the canyon. With the westerly wind direction used in the simulations the maximum difference in air temperature between the street canyons with white (Canyon 2) and black (Canyon 3) facades in 1.8m above ground is  $\sim 0.8^{\circ}\text{C}$  at 15CET for the east-west orientated street canyon with H/W=2. The largest differences in air temperature can be found along the walls, mainly along the southwards exposed. For the north-south orientated canyons with H/W=2 the difference at the same time is  $\sim 2^{\circ}\text{C}$  with a uniform distribution throughout the canyon.

- At the same time a higher albedo causes more incoming solar radiation to be reflected back into the street canyon, resulting in a higher radiative temperature within the canyon.

As can be seen from the simulations of Canyons 1 to 4 the negative effect on human thermal comfort of more solar radiation being reflected into the street canyon outweighs the positive of lower air temperatures. The maximum PET within the canyon with the black facades (Canyon 2) is 4-8 $^{\circ}\text{C}$  lower than the maximum PET within the canyon with a white facade (Canyon 3).

Relevant differences in PET are however limited to the time of incoming solar radiation, i.e. daylight hours. During the night the albedo of the facades has no influence on human thermal comfort within the street canyon.

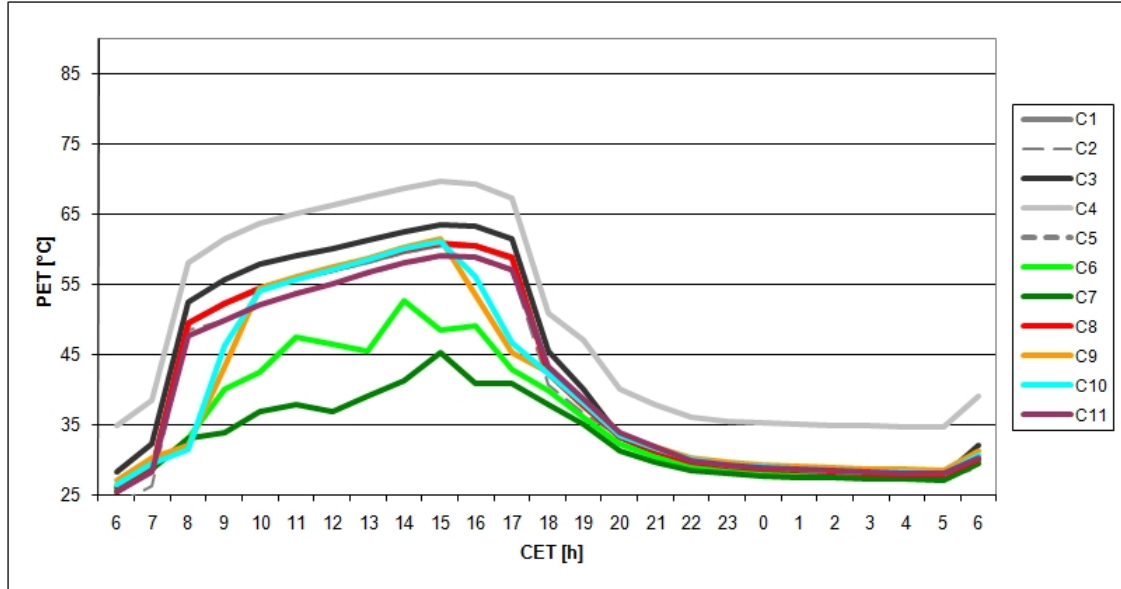


Figure 12: PET in 1.8m above ground averaged over northern pavement. E-W orientation. H/W=1

### 3.4.3. Emissivity of facades

The emissivity determines the absorption and emission of long-wave radiation. A lower emissivity causes less infrared radiation to be absorbed by the facade and to be reflected into the street canyon instead. This effectively lowers the temperature of the facade and as a consequence air temperature within the canyon. But at the same time it also increases the (long wave) radiation budget within the canyon.

Again, concerning human thermal comfort, the negative effects of the lower emissivity outweigh the positive effects by far. Furthermore this negative effect can also be seen during the night. The PET in canyon 4 is continuously 4-5°C higher than in the canyon 2 with otherwise identical walls.

### 3.4.4. Facade surface temperature

In order to assess the influence of the facade surface temperature alone on the human thermal comfort within the street canyon, canyon 5 has a thinner wall with a higher conductivity. As the temperature inside the buildings is kept at the constant value of 20°C, thus simulating an air-conditioned building, the facade surface temperature of canyon 5 is up to 2°C higher than that of canyon 1.

The lower facade temperatures however cause only very small differences in air temperature (<0.3°C) or PET (<1°C) within the canyon.

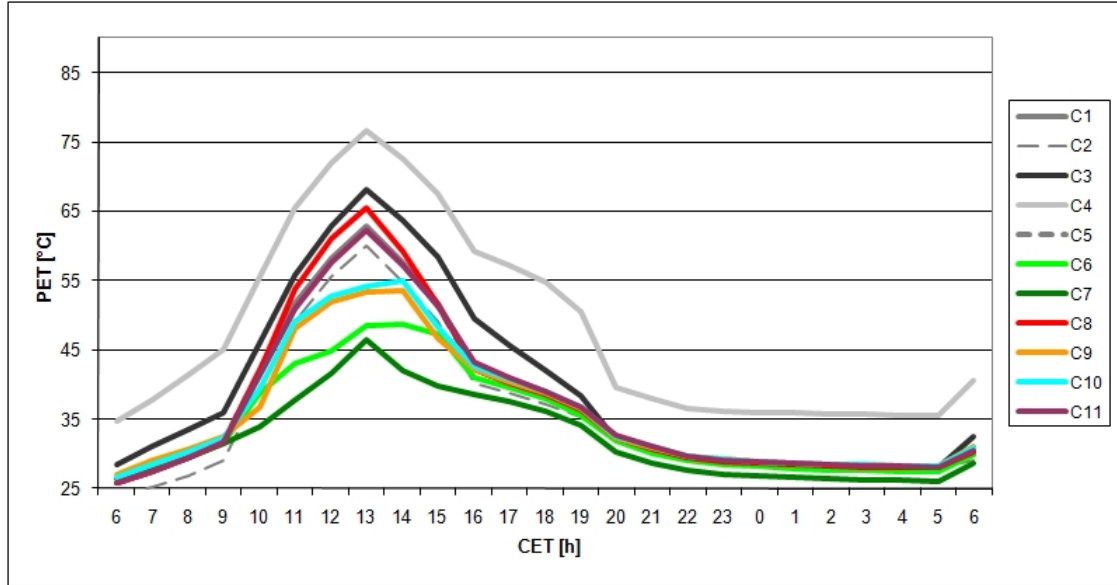


Figure 13: PET in 1.8m above ground averaged over whole street canyon. N-S orientation.  $H/W=1$ .

### 3.4.5. Trees

The two simulations that include large trees within the street canyon (Canyon 6 & Canyon 7) display the lowest average PET values in all configurations. Especially the peak PET values in the afternoon are efficiently reduced by more than  $25^{\circ}\text{C}$ .

The positive influence of the trees within the street canyon is mainly due to the reduction of the incoming solar radiation within the street canyon, which drastically reduces the mean radiant temperature. The reduction of the radiation budget also decreases the temperature of the ground surfaces and the facades, which in return leads to cooler air temperatures.

But the vegetation also has negative impacts on the factors that define human thermal comfort: the specific humidity increases due to the evaporation of the trees and wind speed decreases due to the additional drag of the leaves. In the north-south orientated canyons with  $H/W=2$  the increase in specific humidity compared to the same canyon without vegetation (canyon 1) is up to  $5.8\text{gkg}^{-1}$ . In combination with the low initial wind speed ( $< 0.5\text{ms}^{-1}$ ) and the chosen setup of high trees with a leafless base the wind speed in the lower 2m of the canyon decreases by less than  $0.1\text{ms}^{-1}$ .

Thus the negative effects on human thermal comfort are outweighed, at least for this setup, by the positive effects.

### 3.4.6. Albedo of ground surface

By increasing the albedo of the surface of the asphalt of the street within the canyon (canyon 8) the temperature of the asphalt is decreased by up to  $8^{\circ}\text{C}$ . The cooler surface

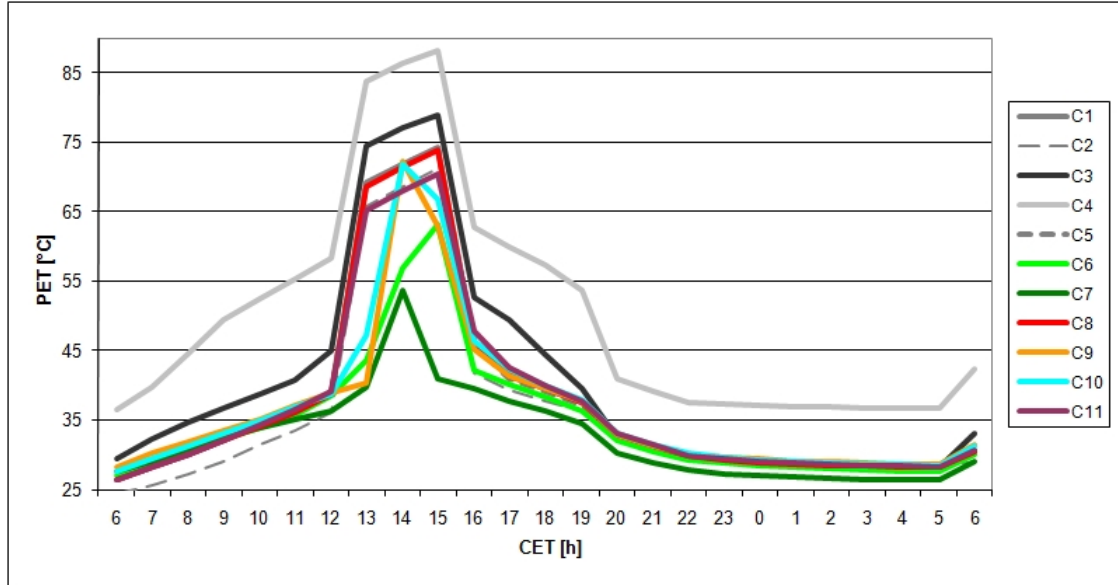


Figure 14: PET in 1.8m above ground averaged over eastern pavement. N-S orientation. H/W=1

temperature of the asphalt in turn causes a lower air temperature (up to 1.3°C in 1.8m above ground) and a lowering of the infrared radiation budget.

These positive effects on human thermal comfort are more than compensated by the increase in reflected short wave radiation. Peak and average PET values are only surpassed by the canyons with highly reflective facade surfaces (canyon 3 & canyon 4). A decrease of 20% in the albedo of the pavements (canyon 11) slightly decreases the PET values by up to 3°C. These maximum differences in PET compared to canyon 1 can be found directly above the pavement. The averaged PET of the whole canyon decreases by less than 0.5°C.

### 3.4.7. Galleries

The use of galleries changes the layout of the canyon to H/W=1.7, respectively H/W=3.3, thus drastically reducing the direct solar radiation at the bottom of the canyon. This reduction in the radiation budget leads to a decrease in PET of up to 13°C for the westward exposed sidewalk in the north-south orientated street canyon. Overall the continuous gallery shows the third lowest PET values in all simulations.

## 3.5. Discussion

The simulations show a clear ranking of the measurements regarding the improvement of human thermal comfort within the street canyon. Not surprisingly the reduction of the incoming direct solar radiation shows the best results in these simulations of a hot middle European summer day. Tall trees with a distinct, dense crown layer (canyon 6 &

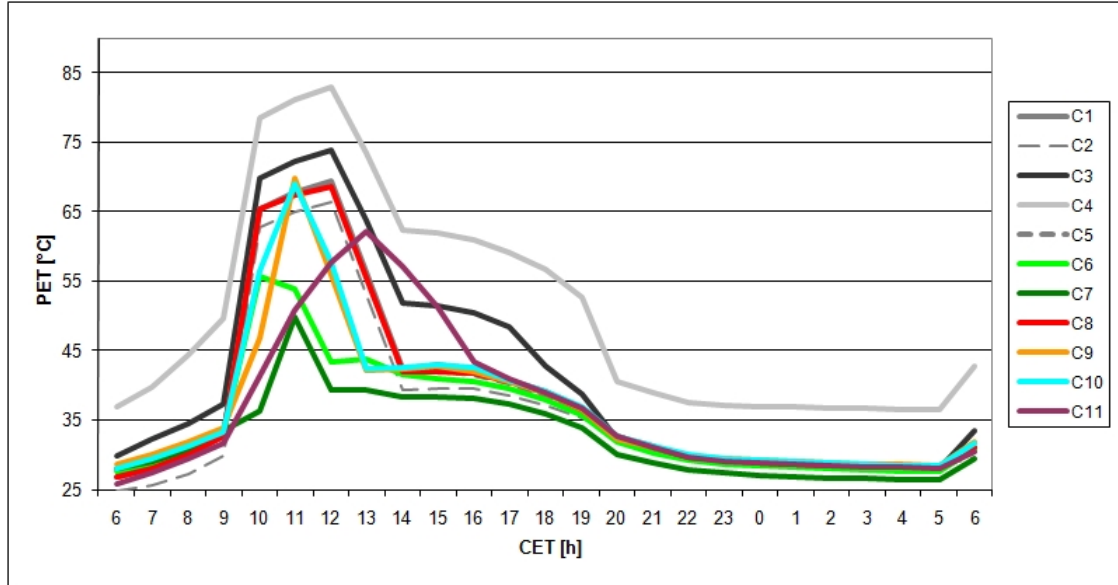


Figure 15: PET in 1.8m above ground averaged over western pavement. N-S orientation.  $H/W=1$

canyon 7) show the lowest average and peak PET values in all four different setups. The use of galleries (canyon 9 & canyon 10) shows comparable but slightly worse results. Regarding the applicability of these measures in central Europe both have their specific weaknesses. Galleries reduce the incoming solar radiation at all times of the years, resulting in a possibly negative impact on human thermal comfort in spring, autumn and winter when the PET values are too low instead of too high and the additional solar radiation is therefore welcome. Deciduous trees share this drawback to a far lesser degree as they lose their leaves in autumn and the blocking of direct solar radiation is therefore drastically reduced during autumn, winter and spring. While this seasonally adjusted influence of trees on the radiation budget within the street canyon makes trees seem as the perfect measure for ameliorating the human thermal comfort at street level, they also have other drawbacks from an urban planning point of view. Trees, especially those with dense foliage and therefore high evaporation rates, have to be regularly irrigated. Otherwise the tree loses its leaves and might even take permanent damage. Especially during summerly heat periods the rainfall often does not suffice to keep trees irrigated, so that artificial irrigation has to be provided by the city. The evaporation by the trees leaves also increases the specific humidity of the surrounding air, thereby negatively influencing the summerly human thermal comfort.

Furthermore trees also decrease the usable street area and cause constant further investments for tree care and street-cleaning [Dwyer et al., 1992]. Due to the overall low wind speed used for the simulations the decrease in wind speed at ground level that is usually caused by trees does not show in the PET index which is used to evaluate human thermal comfort. This blocking of air flow can have a negative effect on the air quality within

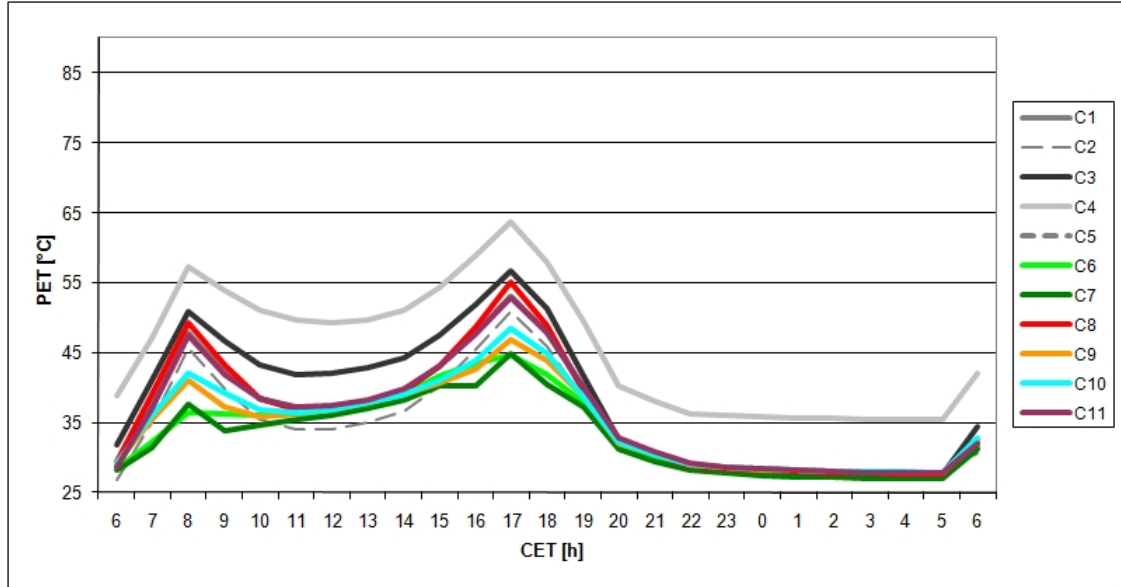


Figure 16: PET in 1.8m above ground averaged over whole street canyon. E-W orientation.  $H/W=2$

the street canyon. Furthermore the emission of Volatile Organic Compounds (VOCs), which varies by species, can lower the air quality by increasing the level of ozone and carbon monoxide in its vicinity [Kesselmeier and Staudt, 1999].

While the choice of facade materials only has very little influence on the human thermal comfort within the street canyon, the radiative properties of the facade surface have a very big impact. The higher the reflectivity of the facades the less radiation is absorbed by the facade and the more is reflected into the street canyon - and absorbed by a person standing/ walking there. The negative impact of a higher radiative energy budget on human thermal comfort outweighs by far the positive effect of cooler facades and as a consequence cooler air temperatures near the facades. This fact is often neglected by researchers who only focus on air temperature and end up recommending the usage of highly reflective surfaces as a measure for mitigating the UHI effect (e.g. Rajagopalan et al. [2008]). While lowering the air temperature by several degrees certainly is not the worst decision it might not be the best either - especially in areas with a high number of pedestrians.

Regarding the energy balance of buildings and thus the human thermal comfort within buildings, the situation is just the opposite: a higher albedo means that the facades absorb less energy, hence the inside of the building stays cooler and less energy is needed for the cooling of the building. This means that architects and construction engineers have to find the best trade off between the energy budget of the building they are designing on the one hand and the human thermal comfort within the vicinity of this building on the other hand.

The same principles as for the albedo of the facades apply to the albedo of the ground



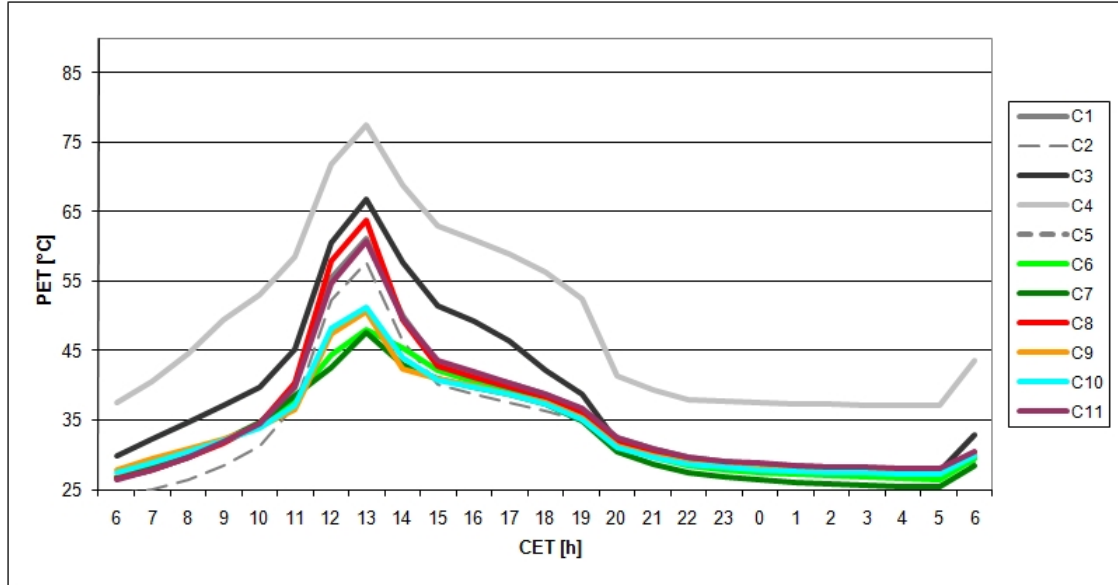


Figure 17: PET in 1.8m above ground averaged over whole street canyon. N-S orientation.  $H/W=2$

surfaces. A higher albedo of the surface leads to a lower temperature of the surface and also of the air in 1.8m above the ground. But again this positive effect is not reflected by the values of PET because at the same time the radiation budget of a human standing within the street canyon is increased as well.

### 3.6. Conclusion

For the meteorological conditions used in these simulations, i.e. a hot summer day in central Europe, the street canyon with dense vegetation (canyon 7) shows the lowest PET values of all model domains. The positive effect of shading by the dense crown layer outweighs, by far the negative effects of higher air humidity and lower wind speed. Furthermore it has been shown that trees also have positive sociological and even economical effects on their neighborhood [Dwyer et al., 1992]. All other measurements tested in these simulations are less efficient or even counterproductive and have strong unwanted side effects like a higher heat load for buildings or a decrease in human thermal comfort during other times of the years.

This study also shows that there is no standard solution for mitigating summerly heat stress within a street canyon because all possible measures have their trade-offs which also strongly depend on the specific situation concerning local wind systems, traffic, air pollution and sociocultural usage of the considered area. In an area zoned for economic activities, i.e. an area in which only very few people are subjects of the local outdoor microclimate, the use of highly reflective surfaces only has advantages: the buildings absorb less radiative energy and thus need less air conditioning in the summer and the

air temperature is lowered and therefore less heat is transferred from this zone to other parts of the city. The negative effects on PET, i.e. the higher mean radiation temperature, in the surrounding of the buildings does not have to be considered - because only very few people are concerned by this increase in PET.

But the same surface materials on the facades of the buildings along a shopping mall would have the same negative effect on the PET of thousands of shoppers. In this case the negative effects outweigh the benefits - at least from the point of human thermal comfort.

## References

- F. Ali-Toudert and H. Mayer. Numerical study on the effects of aspect ratio and orientation of an urban street canyon on outdoor thermal comfort in hot and dry climate. *Building and Environment*, 41:94–108, 2004.
- M. Bruse, 2007. URL <http://www.botworld.info>.
- J. Dwyer, E. McPherson, H. Schroeder, and R. Rowntree. Assessing the benefits and costs of the urban forest. *Journal of Arboriculture*, 18:227–234, 1992.
- J. Houghton, Y. Ding, D. Griggs, M. Noguer, P. van der Linden, X. Dai, K. Maskell, and Johnson C., editors. *Third Assessment Report: Climate Change 2001*. IPCC, 2001.
- S. Idso, R. Jackson, J. Reginato, B. Kimball, and F. Nakayama. The dependence of bare soil albedo on soil water content. *J. Appl. Met.*, 14:109–113, 1974.
- D. Jacob, H. Göttel, S. Kotlarski, Lorenz P., and K. Sieck. Klimaauswirkungen und anpassung in deutschland - phase 1: Erstellung regionaler klimaszenarien für deutschland. Technical report, Umweltbundesamt, 2008. URL <http://www.umweltdaten.de/publikationen/fpdf-1/3513.pdf>. Retrieved 15.02.2011.
- J. Kesselmeier and M. Staudt. Biogenic volatile organic compounds (voc): An overview on emission, physiology and ecology. *Journal of Atmospheric Chemistry*, 33(1):23–88, 1999.
- A. Matzarakis and H. Mayer. Another kind of environmental stress: Thermal stress. who collaborating centre for air quality management and air pollution control. *NEWSLETTER No. 18. WHO Collaborating Centre for Air Quality Management and Air Pollution Control*, pages 7–10, 1996.
- T. Oke. City size and urban heat island. *Atmospheric Environment*, 7:769–779, 1973.
- T. Oke. The energetic basis of the urban heat island. *Quart. J. R. Met. Soc.*, 108:1–34, 1982.
- P. Rajagopalan, H. Wong Nyuk, and D. Cheong Kok Wai. Microclimatic modeling of the urban thermal environment of singapore to mitigate urban heat island. *Solar Energy*, 82(8):727 – 745, 2008. URL <http://www.sciencedirect.com/science/article/pii/S0038092X08000364>.
- M. Rebetez, H. Mayer, O. Dupont, D. Schindler, K. Gartner, J. Kropp, and A. Menzel. Numerical study on the effects of aspect ratio and orientation of an urban street canyon on outdoor thermal comfort in hot and dry climate. *Ann. For. Sci.*, 63:569–577, 2006.



# Part VI.

## Parallelization of ENVI-met

### 1. Summary

Since the mid 2000s software does no longer automatically profit from the ever growing increase in computing power but has to be adapted - parallelized - to take advantage of the multiple processing units available in modern PCs.

The first part of this chapter describes an attempt to make ENVI-met profit from the computing power of modern graphics cards by letting a parallelized version of the often used ADI-routines run on the GPU. The programming language chosen for this task is OpenCL. The results of this parallelization however do not fulfill expectations and it will therefore not be implemented in future releases of ENVI-met.

The second part of this chapter discusses the possibilities to speed up ENVI-met by dividing the model area into several sub-areas and letting the simulation for each sub-area run on an own CPU - a process also known as parallelization by domain decomposition.

### 2. Introduction

The popularity of ENVI-met and its use in many countries around the globe can partly be attributed to the fact that ENVI-met - unlike many other climate simulations - runs on a standard desktop computer with a Microsoft Windows operating System. The constant increase in computing power and system memory, also known as Moore's law ??, allowed the simulation of larger areas and considerably decreased simulation times for areas of the same size - without any adaption of the source code. Not only ENVI-met but any kind of software automatically took advantage of the increased hardware power of new PCs.

In recent years however the situation changed: while Moore's law is still valid software does not profit automatically from the increased hardware power. This is because parallel computing has found its way into mainstream desktop computers in the form of multi-core CPUs. This means that in order to take advantage of the additional computing power the programmer has to change the source code of his software in a such a way that it distributes the calculations as equally as possible onto the different cores.

Furthermore another development of hardware has equipped todays standard personal computer with the same calculating power that large and expensive mainframe computers achieved only a few years ago: modern graphic cards with their powerful graphic processing units (GPUs). This relatively new approach for speeding up calculations is called "general purpose computing on graphics processing units" (GPGPU or GPGP) and requires even more extensive adaptations of the source code.

This sections describe how a GPGPU approach was implemented into ENVI-met and discusses the possibility of a different approach that takes advantage of multi-core CPUs.

## 3. GPGPU - theory

### 3.1. GPU evolution

GPUs were originally designed specifically for graphics. Back in the 1990s the use of a GPU was mainly limited to texture mapping and the rasterization of vertices - operations that benefit from a high level of parallelization. The rendering (or graphics) pipeline, i.e. the way the GPU processes the scene that is to be rendered, had a limited number of operations available that were hardwired on the chip.

These limitations do not apply for modern GPUs with their shaders. Shaders are set of software instructions which allow a programmable rendering pipeline. Furthermore the shader hardware is explicitly designed for parallel computing.

At the moment (2011) there are three different sets of shaders:

- vertex shader: these shaders can manipulate the position, color and texture coordinate of a vertex.
- geometry shader: these shaders can remove vertices from a mesh or add new ones. Their main purpose is to add details to the rendered geometry.
- pixel shader: these shaders calculate the color of an individual pixel.

Earlier graphic cards have special computational units for different kinds of shaders. All modern graphic cards use the unified shading architecture which allows all computational units to run any type of shading operation.

### 3.2. GPU vs CPU

Although CPUs and modern GPUs can be used for the same calculations there are some important differences between them. A standard CPU tries to execute a single program as fast as possible. In order to achieve this goal most modern CPUs have a lot of cache and several techniques like out-of-order execution or speculative execution that can greatly accelerate software but also require a lot of transistors. A larger number of transistors has several disadvantages: the higher the number of transistors, the more expensive the manufacturing because less CPUs can be created from a single wafer. And at the same time the power consumption of a CPU is generally increasing with the number of transistors.

A modern GPU on the other hand is designed to perform many calculations at the same time - because all the pixels of the screen have to be filled simultaneously. This kind of parallelism is generally referred to as single instruction, multiple data (SIMD) parallelism. Therefore the GPU does not need out-of-order or speculative execution but can be designed as an in-order processor with a relatively small amount of cache. This requires fewer transistors and therefore allows to place much more processing units onto the same area of die.

### 3.3. GPU manufacturers

In the last decade the GPU has been dominated by three companies: Intel, ATI (now part of AMD) and NVIDIA.

As of 2010 these three companies share 99% of the market for GPUs for personal computers and workstations ([Fischer, 2011]). Other competitors like VIA, SIS/XGI and Matrox are mainly focusing on special niche markets and performance-wise their products can not compete with those of Intel, ATI/AMD and NVIDIA.

Of the three biggest manufacturers of GPUs Intel has the highest overall market share (roughly 50%). However in the last years Intel has only focused on GPUs that are integrated into the chipsets of motherboards or directly into the CPU. These integrated chipsets are designed with heavy restrictions on the amount of transistors that can be used and therefore can performance-wise not compete with standalone graphic controllers. Furthermore Intel does at the moment (2010) not support any techniques that would allow the use of the integrated graphics chips for general purpose computing. Larrabee, Intel's try to develop a GPGPU device ([Seiler et al., 2008]), has been delayed several times and as of May 2011 there still is no release date available.

ATI/AMD and Nvidia both have a GPU lineup that covers the whole bandwidth from integrated graphic chips over high GPUs for gamers to special graphics cards for workstations. Both companies regularly update their product lineup several times a year in order to surpass their competitor.

Regarding GPGPUs Nvidia has - as of 2010 - a slight advantage over ATI/AMD. NVIDIA has established a highly popular proprietary programming language for their own GPGPUs, CUDA, while ATI/AMD could not establish its own GPGPU programming language which was called Close to Metal. Furthermore NVIDIA also sells PCI-E cards with GPGPUs that are only designed for GPGPU computing and not for the purpose of graphics.

## 4. OpenCL

### 4.1. Choosing the framework

As always when planning a new software project one of the first questions to answer is which programming framework one should choose. The following two frameworks that allow the development of applications that run on the GPU have been considered:

- CUDA (Compute Unified Device Architecture) by NVIDIA
- OpenCL (Open Computing Language) by the Khronos Group

Other frameworks like Close to Metal by AMD, BrookGPU by the Stanford University or DirectCompute by Microsoft were not considered due to limited further development (Close to Metal, BrookGPU) and limitation on a certain operating system (DirectCompute).

At the beginning of 2010 there already existed many projects that use CUDA and only very little that used the relatively new OpenCL. OpenCL however has the important advantage that it is an “open” standard in the sense that it is not controlled by a single company and is therefore not limited to graphics cards of a single manufacturer - as is the case with CUDA which is developed by graphics chip manufacturer NVIDIA. Another advantage of OpenCL over CUDA is that it also supports other computing devices than graphics cards such as standard x86 CPUs, Cell processors or DSP processors. Therefore ultimately OpenCL was chosen as framework for this project of using GPGPU to speed up ENVI-met.

## 4.2. General information about OpenCL

OpenCL was originally developed by Apple Inc. and is now, like also OpenGL, managed by the non-profit technology consortium Khronos Group which is focused on creating royalty-free, cross-platform, open standard application programming interfaces. The two major producers of high performance GPUs, NVIDIA and ATI/AMD, are among the members, as are the worlds largest producer of CPUs and GPUs, Intel [Khronos, 2010] (see fig. 1).

OpenCL is still a relatively new programming framework, the first public release dating



Figure 1: Members of the Khronos group. Source: <http://www.khronos.org/about/>

from the summer of 2009 when Apple Inc. released its operating system Mac OS X v10.6 (Snow Leopard) [Hakes and Evans, 2008]. OpenCL uses a subset of ISO C99 with some extensions for parallelism, making it very easy for programmers who know C to learn the new syntax.

Compared to standard C OpenCL has, as of Version 1.0, several limitations, among



them the following [Khronos, 2008]:

- pointers to functions are not allowed
- recursion is not possible
- the library functions of several C99 standard headers as `stdio.h` or `string.h` are not available and cannot be included
- arrays with variable length are not possible.

Additional elements featured in OpenCL but not in ISO C99 include [Khronos, 2008]:

- *half*: 16bit floats.
- vector data types with 2,4,8 or 16 elements. These are available for the data types *(u)char*, *(u)short*, *(u)int*, *(u)long* and *float*. Arithmetic, relational and logical operators can be applied to these vector data types. The operations are then applied component-by-component.
- *image2d\_t* and *image3d\_t*: two- and three dimensional images.

There exist also built-in math functions available for scalar or vector arguments, like sinus, cosinus etc.

Like OpenGL OpenCL also allows the implementation of additional data types or functions by a certain hardware manufacturer. These manufacturer specific definitions only work with the manufacturer specific hardware and may or may not later become part of the official data types and functions in later versions of OpenCL.

### 4.3. OpenCL architecture

**Platform model** The so called platform model of OpenCL [Khronos, 2008] consists of a single host on which the software runs and which is connected to one or more OpenCL devices (fig. 3). Every device can contain one or more compute units. These compute units correspond to the cores of a CPU or a GPU. The compute units themselves are further divided into processing elements on which the computations take place.

The OpenCL devices have their own RAM and communicate with the host device via an external bus. Usually this is the Peripheral Component Interconnect Express (PCIe) bus. The theoretical maximum transfer capacity of PCIe 2.0 on a sixteen-lane configuration (x16) is 8 GB/s. PCIe 3.0, which has been introduced in late 2010 [Shilov, 2010] is capable of up to 16 GB/s on x16.

#### 4.3.1. Execution model

Functions that execute on OpenCL devices are called kernels. The execution of these kernels is managed by the program running on the host device, the host program.

Several instances of a kernel run simultaneously on one or more OpenCL devices. When the host-program submits a kernel for execution it defines an index space (NDRange)

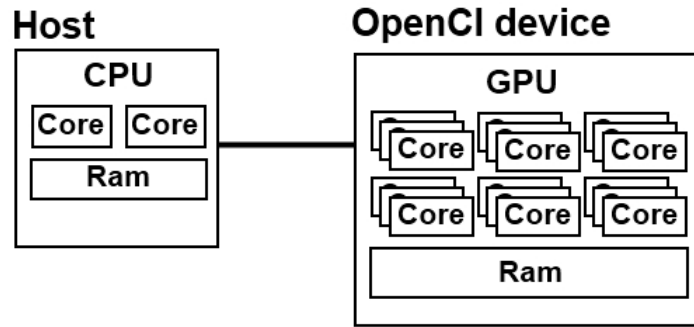


Figure 2: Schematic of an OpenCL system.

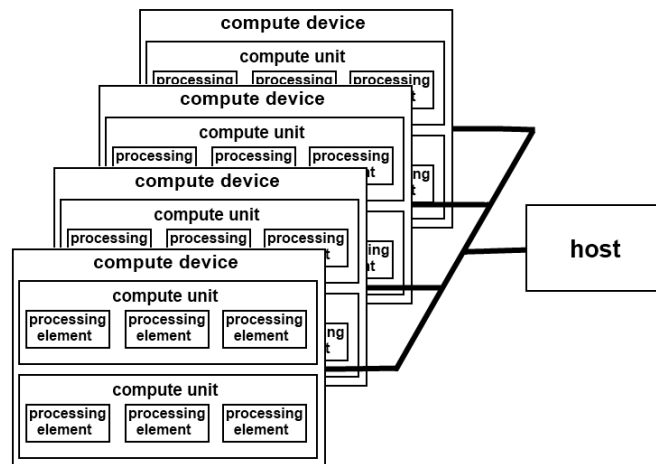


Figure 3: Platform model of OpenCL.

and calls an instance of the kernel for every point of that index space. The N-dimensional index space can have  $N=1$ ,  $N=2$  or  $N=3$  dimensions. The necessary dimension of the index space depends on the problem that is to be solved by the program: e.g. the processing of a linear array requires  $N=1$  while the processing of a 3D volume requires  $N=3$ . Each instance of a kernel is called a work-item and has a global ID which is derived from the index space. Each work-item executes the same code.

A work-group consist of several work-items and also has a unique ID. The work-group allows to synchronize the calculation of several work-items. The work-items of a work-group are calculated simultaneously on the processing elements of a compute device (fig. 4). The size of a work-group therefore depends on the OpenCL device that is used and as a consequence should not be hard-coded.

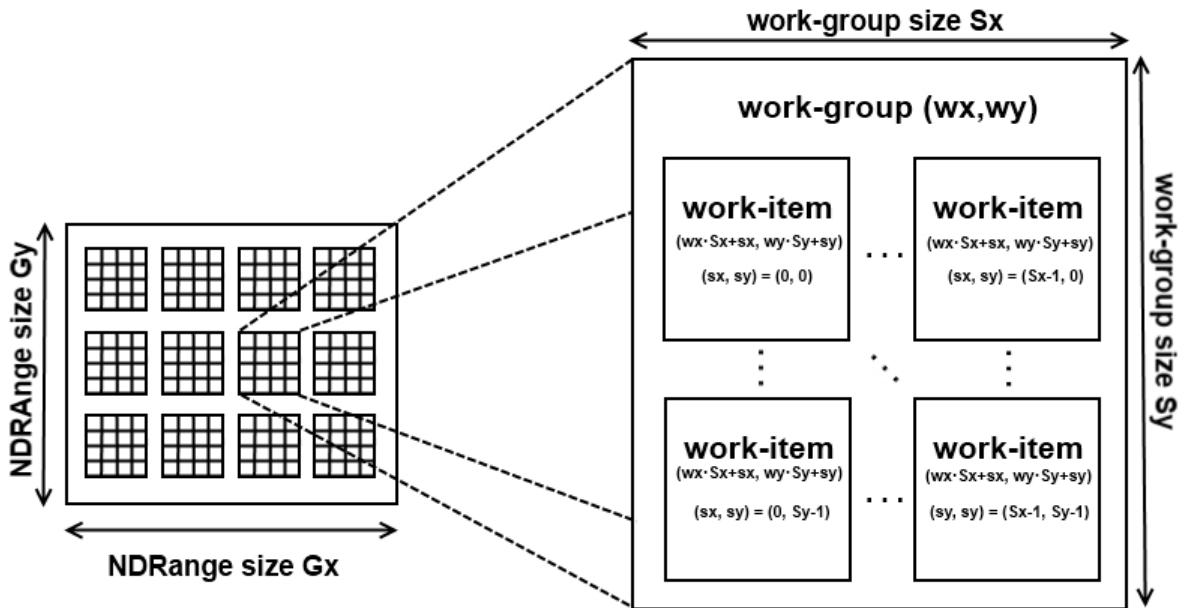


Figure 4: Example showing index space, work-group and work-items with their global IDs.

The host controls the execution of the OpenCL program via a data structure called command queue. Commands that are placed within this command queue control the execution of the kernels (kernel execution commands), the data transfer to, from and within the OpenCL device (memory commands) and the order of execution of commands (synchronization commands). The command queue supports in-order and out-of-order execution.

#### 4.3.2. Memory model

OpenCL features four different types of memory (fig. 5):

- global memory: read-write access for all work-items in all work-groups.
- constant memory: a part of global memory with read-only access. It remains constant throughout the run-time of a kernel and only the host has write permission.
- local memory: memory which is local to a work-group, i.e. is only accessible by the work-items of the work-group.
- private memory: memory that is private to a work item, i.e. memory that can only be accessed by the specific work-item.

On graphics-cards local memory corresponds to on-chip memory [NVIDIA, 2009]. Therefore local and private memory are, on most current devices, considerably faster than global or constant memory. It has however also a very limited size of typically 16kB. The memory of the host and the memory of the OpenCL device are independent of each other. There are two modes for copying data: a blocking memory transfer only transfers data once the host memory is safe to use. A non-blocking memory transfer copies the data regardless the state of the host memory. It is also possible for the host to map a region from an OpenCL memory object into its address space so that the host can read from this region or write to it.

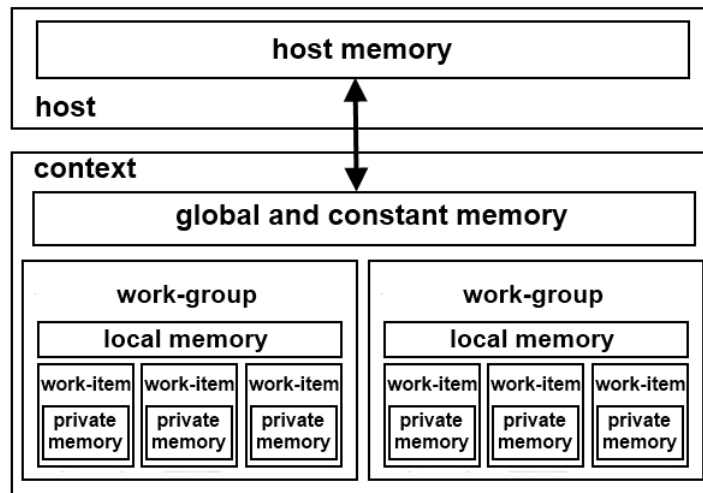


Figure 5: Schematic of memory concept of OpenCL.

### 4.3.3. Programming Model

OpenCL supports data parallel and task parallel programming models and as a consequence also a mixture of both.

Data parallelism means that each processing unit performs the same task, but on a different set of data. Task parallelism on the other hand means that each processing unit performs a different task, but on the same set of data.

The main focus of OpenCL however is on data parallelism.

## 5. Implementation in ENVI-met

### 5.1. Conversion from Delphi to C++

ENVI-met was written in Delphi (Pascal). In regard to the parallelization using GPGPU with OpenCL this programming language (as of 2010) has two major flaws:

- no support for OpenCL.
- no possibility to compile native 64bit applications.

There exist a few projects that want to make OpenCL usable for Delphi, but at the beginning of 2010 none of these projects was able to provide a stable and tested header for OpenCL.

The lack of a 64bit compiler has no direct impact on the ability to use OpenCL. 32bit applications however limit the memory that can be used by a single application to 2GB, thereby limiting the maximum size of a model area that can be simulated with ENVI-met. An increase in the speed of calculation would therefore only result in a faster simulation time but would not allow larger simulation areas.

Furthermore the Delphi development software and compiler are only available for Microsoft Windows. An alternative, the freely available compiler named Free Pascal, is also capable of compiling for Linux and Mac OS X. For these operating systems there even are 64bit version of the compiler available. But Free Pascal is neither 100% compatible with Delphi, requiring minor adaptations of the source code, nor is there a 64bit compiler for Microsoft Windows [Lazarus].

Therefore the decision was made to convert the code from Delphi to C++ before starting the implementation of the parallelization. The code was converted with the help of a tool that could automatically convert some parts of the code, as e.g. loops and if-clauses, and helped speed up the process of the conversion significantly.

## 5.2. ADI-Routines

The next step of the process of the parallelization of ENVI-met was to identify procedures that could be transferred onto the graphics card. ENVI-met consists of many procedures and routines, some of which are only run once per simulation while others are repeated for every second of simulated time. In order to speed up ENVI-met noticeably only those calculations that are performed frequently were considered for parallelization. The routines most often used by ENVI-met are the so called *Alternating Direction Implicit* (ADI) ([Peacemen and Roachford, 1955],[Douglas, 1955],[Douglas, 1962],[Douglas and Roachford, 1956]) routines that are used for solving the multi dimensional differential equations. The ADI method is implicit and therefore numerically stable even with big time steps  $\Delta t$  and has a first-order accuracy in space and a second-order accuracy in time ([Douglas, 1957]).

The ADI method divides the original differential equation into  $n$  equations, each of which implicitly calculates the exchange processes in one of the  $n$  dimensions of space under consideration. For  $n=3$  dimensions the ADI method can be written as:

$$\frac{\phi^* - \phi^n}{\Delta t} = \langle \partial \phi^* \rangle_x + \langle \partial \phi^n \rangle_y + \langle \partial \phi^n \rangle_z + f \phi^* + R_\phi \quad (1a)$$

$$\frac{\phi^{**} - \phi^*}{\Delta t} = \langle \partial \phi^{**} \rangle_y + \langle \partial \phi^n \rangle_y \quad (1b)$$

$$\frac{\phi^{n+1} - \phi^{**}}{\Delta t} = \langle \partial \phi^{n+1} \rangle_z - \langle \partial \phi^n \rangle_z \quad (1c)$$

With  $\phi$  as the variable under consideration,  $n$  as the actual, known, time step and  $n+1$  the future time step and  $\phi^*$  and  $\phi^{**}$  as the interim solutions of the ADI method.

The order in which the three dimensions are calculated is arbitrary.

The implicit difference equation for the space direction  $i$  can be written as:

$$\langle \partial \phi^{n+1} \rangle_i \rightarrow \frac{\phi_a^{n+1} - \phi_a^n}{\Delta t} = A_a^i \phi_{a-1}^{n+1} + B_a^i \phi_a^{n+1} + C_a^i \phi_{a+1}^{n+1}. \quad (2)$$

With the coefficients  $A_a^i, B_a^i$  and  $C_a^i$  as:

$$A_a^i = \frac{\delta_a^\psi}{\Delta_a^i} (adv A_a^i + \delta_{a-1}^c \frac{K_a^{i-}}{\Delta_a^{i-}}) \quad (3a)$$

$$B_a^i = -\frac{\delta_a^\psi}{\Delta_a^i} adv B_a^i - \frac{\delta_a^\psi}{\Delta_a^i} (\delta_{a-1}^c \frac{K_a^i}{\Delta_a^{i-}} + \delta_{a+1}^c \frac{K_a^{i+}}{\Delta_a^{i+}}) \quad (3b)$$

$$C_a^i = \frac{\delta_a^\psi}{\Delta_a^i} (-adv C_a^i + \delta_{a+1}^c \frac{K_a^{i+}}{\Delta_a^{i+}}) \quad (3c)$$

With the following definitions:

- $\Delta_a^i$ : centered differences. Grid box  $a$  with variable centered in space direction  $i$ .
- $\Delta_a^{i+}$ : forward difference between  $a$  and  $a+1$  in direction  $i$
- $\Delta_a^{i-}$ : backward difference between  $a$  and  $a+1$  in direction  $i$
- $a$  designates the component of the three dimensional grid point coordinates  $i, j, k$  which is variable in space direction  $i$ .  $a=i$  for  $i=x$ ,  $a=j$  for  $i=y$  and  $a=k$  for  $i=z$ .
- $\delta^\psi$  is an indicator that indicates obstructed cells and walls.  $\psi$  designates the direction of the wall ( $\psi=x, y, z$ ) or the center of the grid cell ( $\psi=c$ ). If a cell is blocked by a building or by the digital elevation model then (fig. 6) :

$$\begin{aligned} \delta_{i,j,k}^c &= 0 \\ \delta_{i,j,k}^x &= \delta_{i+1,j,k}^x = 0 \\ \delta_{i,j,k}^y &= \delta_{i,j+1,k}^y = 0 \\ \delta_{i,j,k}^z &= \delta_{i+1,j,k+1}^z = 0 \end{aligned}$$

For the solution of this system of equations it has to be transformed into a vector system  $\mathbf{A} \times \mathbf{x} = \mathbf{y}$  with  $\mathbf{A}$  as the coefficient matrix with  $A \times A$  elements,  $\mathbf{y}$  a vector that contains known variables and  $\mathbf{x}$  as the solution vector.

For each direction in space such a vector system has to be solved.  $\mathbf{x}$  can then be calculated by multiplying the inverted matrix  $\text{inv } \mathbf{A}$  with  $\mathbf{y}$ :

$$\mathbf{x} = \text{inv } \mathbf{A} \times \mathbf{y}.$$

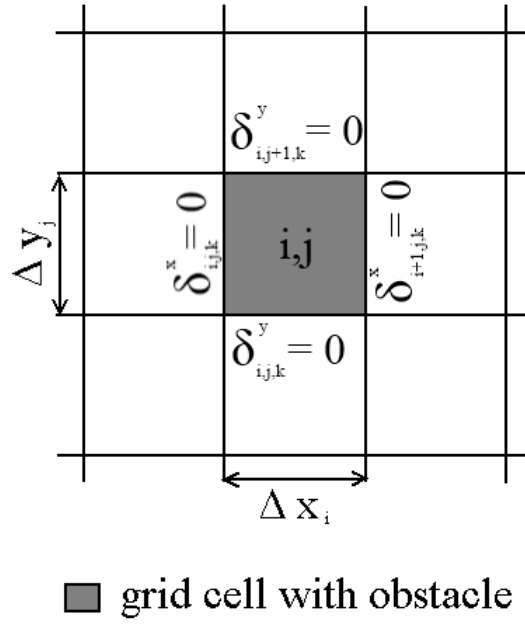


Figure 6: Schematic of grid.

The inversion of the tridiagonal matrix  $\mathbf{A}$  is accomplished by a LU decomposition [Press et al., 1990].

The complete ADI method can be written as:

$$x^* = inv\mathbf{A}^I \times \mathbf{y}^I(\phi^n) \quad (4a)$$

$$x^{**} = inv\mathbf{A}^{II} \times \mathbf{y}^{II}(\phi^n, \phi^*) \quad (4b)$$

$$x^{n+1} = inv\mathbf{A}^{III} \times \mathbf{y}^{III}(\phi^n, \phi^{**}) = \begin{bmatrix} \phi_0^{n+1} \\ \phi_1^{n+1} \\ \phi_2^{n+1} \\ \vdots \\ \phi_a^{n+1} \end{bmatrix} \quad (4c)$$

With one matrix inversion the prognostic variables for the searched time step ( $\phi_{i,j,k}^{n+1}$ ) are calculated synchronously for all grid points  $[0(1),A]$  in the direction which is calculated implicitly while the other two directions are constant. If the ADI is calculated implicitly in the x-direction then:  $i = [1,I]$ ,  $j = \text{const}$ ,  $k = \text{const}$ . In this case a separate matrix inversion has to be calculated for every coordinate  $j=[2,J-1]$  and  $k=[1,K-1]$  in order to get a complete result for all grid points within the model area. All in all the ADI step in x-direction thus needs  $(J-1-2) \times (K-1-1)$  matrix inversions, all of which can be calculated simultaneously because they are not interdependent.

The other ADI steps in the other directions are calculated in an analogue way. The values at the borders of the model area are not calculated in the ADI routines and later set according to the boundary conditions of the model.

### 5.3. Implementation

As explained in the previous section the parallelization of the so called ADI routine consists of the parallel execution of the matrix inversions needed for a single step, i.e. calculation in one direction of space, of the ADI routine.

In the non-parallelized version of ENVI-met the source-code for the ADI-routines contains the following steps:

1. calculation of the coefficients  $A_a^i, B_a^i, C_a^i, f\phi^*$  and  $R_\phi$  for all inner grid points ([2..I-1,2..J-1,1..K-1]).
2. first step of ADI routine (e.g. x-direction): sequential LU-decomposition for  $i=2..I-1$  and  $j=2..J-1$ .
3. second step of ADI routine (e.g. y-direction): sequential LU-decomposition for  $j=2..J-1$  and  $k=1..K-1$ .
4. third step of ADI routine (e.g. z-direction): sequential LU-decomposition for  $i=2..I-1$  and  $k=1..K-1$ .

The Delphi source code for an ADI routine in x-direction and for the LU-decomposition can be found in the appendix in listings 1 and 2.

The OpenCL version of the ADI routine has the following steps:

1. (CPU) calculation of the coefficients  $A_a^i, B_a^i, C_a^i, f\phi^*$  and  $R_\phi$  for all inner grid points ([2..I-1,2..J-1,1..K-1]).
2. (GPU) allocate memory on OpenCL device and copy data
3. (GPU) launch kernel for first step of ADI (e.g. x-direction): parallel LU-decomposition for  $i=2..I-1$  and  $j=2..J-1$ .
4. (CPU & GPU) read back results
5. (GPU) launch kernel for second step of ADI (e.g. y-direction): parallel LU-decomposition for  $j=2..J-1$  and  $k=1..K-1$ .
6. (CPU & GPU) read back results
7. (GPU) launch kernel for third step of ADI (e.g. z-direction): parallel LU-decomposition for  $i=2..I-1$  and  $k=1..K-1$ .
8. (CPU & GPU) read back results



The Delphi and OpenCL source code for the OpenCL version of the ADI of air temperature can also be found in the appendix in listings 3.

The ADI routines are implemented for the following variables:

- turbulence  $E$
- dissipation  $\epsilon$
- specific humidity  $q$
- potential temperature  $T$
- wind components  $u, v, w$

The update interval of these variables, i.e. the frequency of the ADI calculations, depends on the settings of the simulation and the simulated time of day. With the standard settings the wind components, turbulence and dissipation are calculated every 900 seconds of simulated time while the potential temperature and specific humidity are updated at least every ten seconds of simulated time.

## 6. Results

The results discussed in the following section were measured on a an Intel Xeon W3530 @2.8GHz with 12GB of Ram running Ubuntu 10.1. The graphics card used in these tests is a Nvidia Geforce GTX 470. This GPU has 448 cores a maximum clock frequency of 1215 MHz. The 1280 MB of GDDR5 Ram are clocked at 1674 MHz. The driver version 256.25 and OpenCl 1.0 were used for the test calculations. The measured memory transfer rate from host to device is  $5109MBs^{-1}$  and  $5510MBs^{-1}$  from the device to the host.

For a comparison of the computing time between CPU and GPU the ADI routine for the calculation of the potential temperature is regarded (fig. 7). The other ADI routines show very similar results.

The results show a strong correlation between the size of the simulated model area, i.e. the number of grid cells, and the speedup achieved by the OpenCL version of the ADI routine.

For a number of grid cells below approximately 70000 the OpenCL version of ENVI-met takes a longer time to compute than the standard version that only uses the CPU. At 300000 grid cells the OpenCL version already shows a speedup of 2.9 and at 1.2 million grid cells a speedup of 3.7.

This increase in speedup with the size of the model area can be explained when regarding the computing times of the single steps of the ADI routines (tab. 1): the allocation of the memory on the OpenCL device and the transfer from the host to the OpenCL device, i.e. the transfer of all variables needed for the LU decomposition of the matrices from the memory of the PC into the memory of the graphics card, is the step of the computation that takes the longest time. The LU decomposition of the matrices itself always runs faster on the OpenCL device. Even for a small model area with only

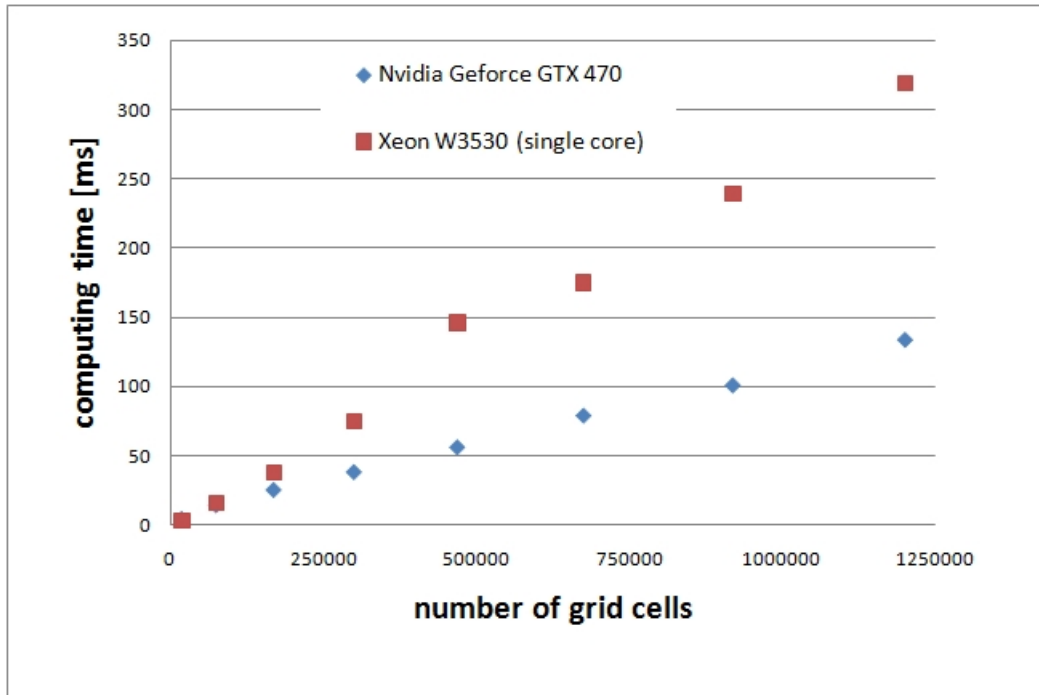


Figure 7: Comparison of computing time for ADI routine for potential temperature between CPU and GPU

$25 \times 25 \times 30$  grid cells the LU decomposition on the graphics card only takes 1ms opposed to 3ms on the CPU - while the total process including memory transfer takes 4ms on the GPU. The time taken for the allocation and transfer of the memory from the host to the device increases with the number of grid cells. This increase is directly proportional to the number of grid cells and is therefore lower than the increase in computing time for the LU decomposition. Thus the more grid cells the model area has the less influence the time it takes to copy the data from the host to the OpenCL device has on the overall computing time of the ADI routine.

The actual speedup this implementation of GPGPU computing causes for the whole simulation is difficult to validate as the ratio between the calculation of the ADI routines and other functions is not constant but rather depends on the model area (distribution of buildings, plants and digital elevation model), the boundary conditions and the simulated date and time. On an empty model area the observed speedup ranges from 0.9 for very small areas to up to 1.3 for an area of  $200 \times 200 \times 30$  grid cells.

## 7. Discussion

The parallelization of ENVI-met via OpenCL shows a considerable decrease of computing time, especially for areas above 1 million grid cells. However this decrease is far

	computing time CPU [ms]	computing time GPU [ms]
memory transfer	-	32
z-direction	40	22
x-direction	48	6
y-direction	31	8
<b>sum</b>	<b>119</b>	<b>70</b>

Table 1: Comparison of computing times of ADI routine between CPU and GPU. Size of model area: 150x150x35 (=787500) grid cells.

below our initial expectations. At the beginning of the project it was hoped that the use of of a GPGPU could lead to a speedup factor of at least ten for the ADI routines and of at least 4 for the whole simulation. Therefore the results can be considered to be a disappointment.

There are mainly two reasons why the ADI routines are not as well suited for parallelization on a GPGPU as previously thought:

- The amount of data that needs to be transfered from the host to the OpenCL device in relation to the number of calculations performed. For the LU decomposition a total of 16 float arrays with the size of the model area have to be transfered from the memory of the host to the memory of the OpenCL device. With each of the values of the arrays only being used once or twice in the calculations.
- The number of memory accesses needed for the LU decomposition. For each step of the LU decomposition a lot of memory accesses take place. As the amount of local memory (48kbyte) does not suffice to accommodate all necessary variables only the much slower global memory of the graphics card can be used.

Unfortunately neither of these two problems can easily be solved at the moment. Future developments of GPGPUs might offer new possibilities and help up speed ENVI-met. At the moment an OpenCL augmented version of ENVI-met is only available for Linux and it is only available for internal testing with no concrete plans for a public distribution.

## 8. Alternative parallelization on CPUs

As the use of GPGPUs has not brought the speed-up that was hoped for another concept for using the parallel architecture of modern PCs was devised. This concept relies on multi-core CPUs rather than GPGPUs. This project has however not yet been implemented in ENVI-met.

### 8.1. Theory

The basic idea of this concept is to divide the ENVI-met model area into a number equaling the number of CPU-cores available on the host and to let each core calculate

the microclimate of one of these sub-areas. In order to couple the sub-areas the lateral boundary conditions at the inflow borders of the sub-areas have to be defined by the outflow-profiles of the upstream sub-areas.

This approach is known as domain composition and widely used for the parallelization of simulations concerning spatial problems (e.g. see [Armstrong and Densham, 1992]).

## 8.2. Proposition for an implementation into ENVI-met

If this mode of parallelization was to be implemented into ENVI-met the software would require several changes and additions that are described in the following sections.

### 8.2.1. Decomposition of the model area

The first and also most important step of a parallelization of ENVI-met is the decomposition of the model area into several smaller areas.

Before the decomposition starts there are two choices that have to be made:

- borders: overlapping borders or non-overlapping borders (fig. 8).
- sub-areas: equally sized or randomly shaped.

The first choice is easy to make: for ENVI-met only overlapping borders are suitable because they allow a better interconnection of adjacent sub-areas than a non-overlapping border. Non-overlapping sub-areas are only suited for calculations with no exchange of information between the sub-areas. The second choice is a much more difficult one: in

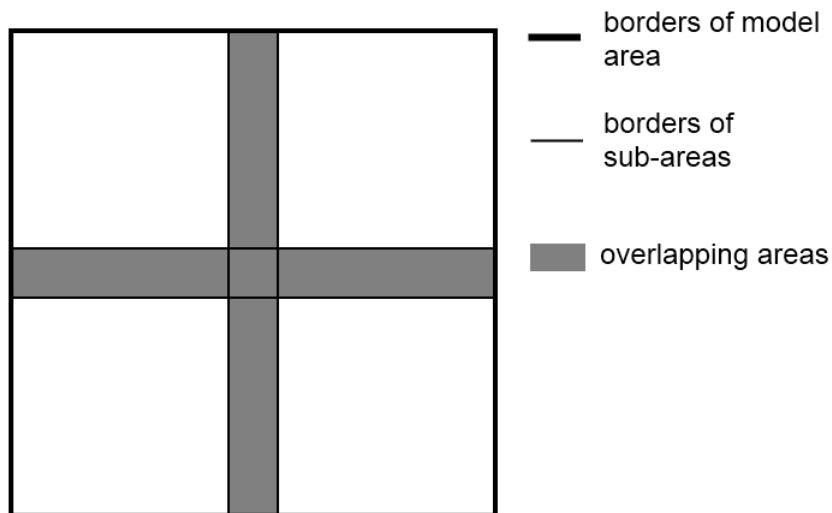


Figure 8: Schematic of overlapping borders.

order to achieve an ideal speedup from the parallelization the calculation of the atmospheric processes in all sub-areas should take the same time because the sub-areas have to be synchronized regularly along their overlapping borders. With an empty model area, i.e. a model area without any buildings, digital elevation model and plants, equally sized sub-areas would well comply with this criteria. Once buildings, a digital elevation model or plants are involved and not evenly distributed across the model area a decomposition into evenly shaped and sized sub-areas will not fulfill this criteria anymore.

The computing time of ENVI-met mainly depends on the following three factors:

- the number of grid cells of the model area
- the configuration of the model area (i.e. distribution of buildings and digital elevation model)
- the meteorological boundary conditions, especially wind speed and wind direction.

While the number of grid cells is a known factor, the influence of the model configuration and the boundary conditions on the computing time is much more difficult to assess. ENVI-met calculates the turbulence field and wind field in a quasi-prognostic way: the fields are recalculated until the maximum change is below a certain threshold (e.g. 1% of the geostrophic wind speed in case of the wind field) or a certain number of iterations has been reached - so that the simulation won't be trapped in an infinite loop. Thus ENVI-met needs the more simulation time the more turbulent the flow within the model area is. As rough rules of thumb it can be said that the flow is more turbulent and thus the computing time longer the more complex the distribution of buildings within the model area and the higher the wind speed. This means an evenly shaped model area like e.g. an north american suburb with its broad streets and well aligned, evenly sized houses will take less computing time to simulate than a same size model of a historic central-european town centre that dates from medieval times.

Concerning the wind direction not even a rough thumb rule can be applied. A model area might run fine with winds coming from east but might take a lot more computing time or even crash due to numerical instabilities of the turbulence and wind fields if the wind comes from the south - with otherwise identical settings. Thus a decomposition that might be favorable for one wind direction might have an adverse effect if the wind direction is not constant throughout the simulation.

Because of these problems concerning the estimation of the computing time necessary to calculate a certain model area ENVI-met should implement two different approaches for the decomposition of the model area:

- a semi-automatic decomposition.
- a manual, user-defined decomposition.

The semi-automatic decomposition would divide the model into a user-defined number of sub-areas with an equal number of grid cells. The user has the possibility to change

the layout of the decomposition, i.e. if the model area is divided along the x-axis, y-axis or both (fig. 9).

The manual mode would allow the advanced user to manually define the borders of the

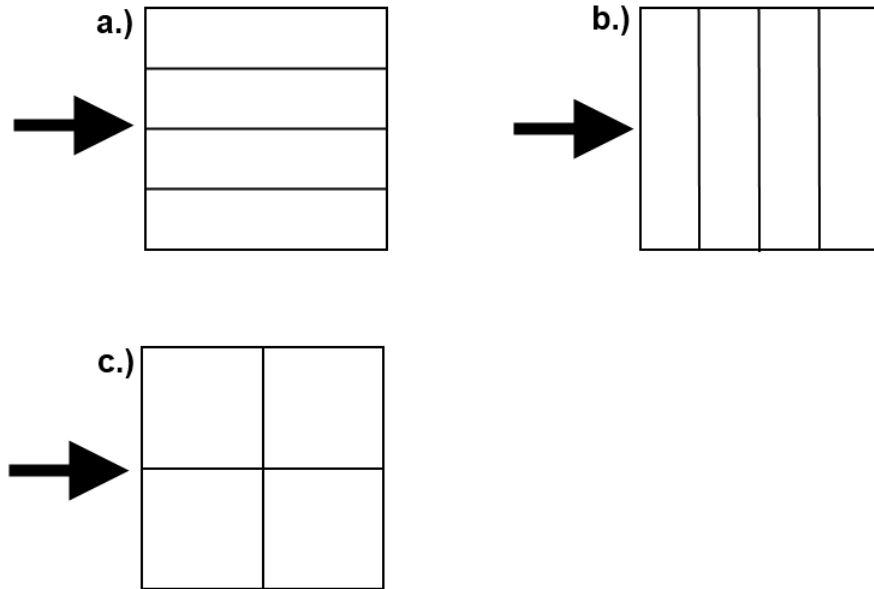


Figure 9: Schematic of possible decompositions of a model area. a.) Decomposition along x-axis. b.) decomposition along y-axis. c.) decomposition along x- and y-axis.

sub-areas. An advanced user with experience in micro-climatic modeling could thus find the ideal decomposition of the model area.

The maximum number of sub-areas would in both cases be defined by the number of CPU cores available on the PC the calculation takes place.

### 8.2.2. Initialization

The initialization of ENVI-met does not have to be changed for the proposed parallelization. All variables of the 3D model have to be initialized for the whole model area.

### 8.2.3. Model run - exchange between sub-areas

For the prognostic main loop of the simulation every sub-area is assigned its own thread, i.e. the calculations for each sub-area are performed on a separate core. If overlapping borders are selected for the sub-areas every thread has to use private memory because otherwise two or more threads will calculate the variables of the same grid point.

During the simulation the sub-areas have to exchange data from time to time in order

to update their boundary conditions. In order to get an accurate and consistent update of the border areas the intervals between this update should occur at least as often as the recalculation of the wind field.

At these points in the simulation all threads have to be synchronized, i.e. the sub-area that takes longest to calculate defines the runtime.

For the exchange the centered variables are copied between the arrays of the sub-areas (fig. 10). The non-centered components - wind speed - are copied according to a similar scheme (fig. 11).

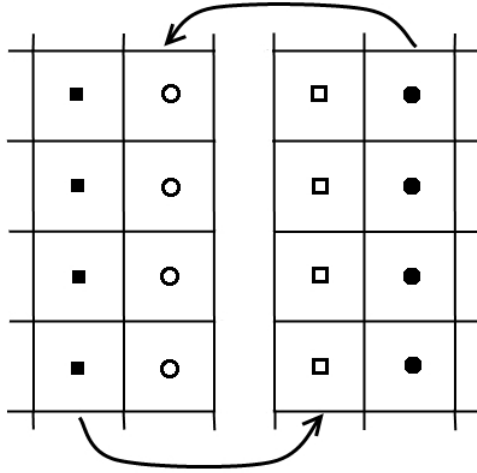


Figure 10: Schematic of exchange of centered variables between the sub-areas.

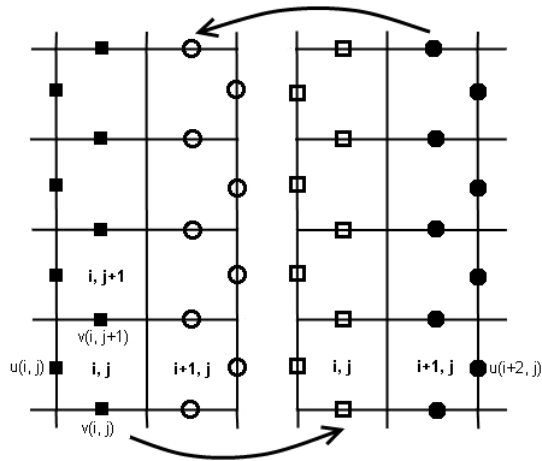


Figure 11: Schematic of exchange of wind components between the sub-areas.

The data output can then be created by combining the results of the sub-areas.

### 8.3. Discussion

The implementation of a parallelization based on the decomposition of the model area offers a promising perspective for the acceleration of ENVI-met and requires only moderate changes to the source code. The routines that for the calculation of the spatial and temporal development of the different parameters can remain untouched. Only the handling of the boundary conditions of the sub-areas would have to be adjusted.

The biggest advantage of this approach of parallelization is that every modern PC could benefit as multi-core CPUs have been a standard component in PCs for years. Single-core CPUs are still being produced but only used in low-end devices. Current mainstream PCs usually have four cores.

The speedup that can be expected from this method strongly depends on the selected breakup of the specific model area and also on the boundary conditions of the wind. But an acceleration of a factor above 3 on a quad-core CPU is realistic even for a suboptimal decomposition.

### 8.4. Summary

At the moment one of the biggest challenges for the future development of ENVI-met is to speed up the simulation and allow the simulation of larger model areas within an acceptable time frame - while keeping one of the biggest advantages of ENVI-met: the possibility to run microclimate simulations on any personal computer or even laptop.

This can only be accomplished by taking advantage of the parallel computing structures that can nowadays be found in any personal computer: massively parallel GPGPUs of the graphic cards and multiple CPU-cores.

As this research has shown the numerical methods of ENVI-met are unfortunately not well suited for calculation in a massively parallel environment like a graphics card. The ADI-routines which take up most of the calculating power of ENVI-met have an unfavorable ratio of calculations to memory transfer and therefore do not show the speedup of several magnitudes generally associated with GPGPU computing. Other routines might be better suited for this kind of parallelization but are not called as often as the ADI routines so that even a massive speedup in the calculation of these routines would only slightly increase the overall speed of the simulation.

The overall acceleration of the GPGPU acceleration of the ADI-routines is noticeable - but comes at a relatively high cost: modern high-end graphics cards often cost more than a whole personal computer with integrated graphics and generally are the components with the highest power consumption within a PC.

As the evolution of graphics cards is - at the moment - still continuing at a very high pace and new functions are implemented into every new generation of GPUs, ENVI-met might profit more from GPGPU-computing within a few years.

In the foreseeable future however the acceleration of ENVI-met via the decomposition of the model area onto the available cores of the CPU seems to be the better choice. Every



user of ENVI-met would benefit from this development, even without new investments into new hardware.

As so often in software development a first implementation of this kind of parallelization could be ready within a few months but the optimization of the algorithms that govern the decomposition of the model area in the most favorable manner, i.e. to divide the model area in such a way that the computations in all sub-areas takes approximately the same time, would take a much longer time.

## References

- M. Armstrong and P. Densham. Domain decomposition for parallel processing of spatial problems. *Computers, Environment and Urban Systems*, 16(6):497 – 513, 1992.
- J. Douglas. On the numerical integration of  $\partial^2 u / \partial x^2 + \partial^2 u / \partial y^2 = \partial u / \partial t$  by implicit methods. *J. Society of indust. Applied Mathematics*, 3(1):42–56, 1955.
- J. Douglas. A note on the alternating direction implicit method for the numerical solution of heat flow problems. *Proceedings of the American Mathematical Society*, 8:409–412, 1957.
- J. Douglas. Alternating direction methods for three space variables. *Numerische Mathematik*, 4:41–63, 1962.
- J. Douglas and H. Roachford. On the numerical solution of heat conduction problems in two and three space variables. *Transaction of the American Mathematical Society*, 82:421–439, 1956.
- M. Fischer. Grafikchip-markt: Nvidias anteil rutscht drastisch ab, 2011. URL <http://heise.de/-1237548>. Retrieved 09. June 2011.
- J. Hakes and B. Evans, 2008. URL <http://www.apple.com/pr/library/2008/06/09snowleopard.html>. Retrieved 25. February 2011.
- Group Khronos, 2010. URL <http://www.khronos.org/members/promoters>.
- OpenCL Working Group Khronos. Khronos opencl working group: The opencl specification, version 1.0, revision 29, 2008. URL <http://www.khronos.org/registry/cl/specs/opencl-1.0.29.pdf>.
- Lazarus. URL <http://www.lazarus.freepascal.org/index.php/page,7.html>.
- NVIDIA. Opencl programming for the cuda architecture, version 2.3., 2009. URL [http://www.nvidia.com/content/cudazone/download/OpenCL/NVIDIA\\_OpenCL\\_ProgrammingOverview.pdf](http://www.nvidia.com/content/cudazone/download/OpenCL/NVIDIA_OpenCL_ProgrammingOverview.pdf). Retrieved 24. February 2011.
- D. Peacemen and H. Roachford. The numerical solution of parabolic and elliptic differential equations. *J. Society of indust. Applied Mathematics*, 3(1):28–41, 1955.
- W. Press, B. Flannery, S. Teukolsky, and W. Vetterling. *Numerical Recipes in C*. Cambridge University Press, New York, 1990.
- L. Seiler, D. Carmean, E. Sprangle, T. Forsynth, M. Abrash, P. Dubey, S. Junkins, A. Lake, J. Sugerman, R. Cavin, R. Espasa, E. Grochowski, T. Juan, and P. Hanrahn. Larrabee: A many-core x86 architecture for visual computing. *ACM Transactions on Graphics*, 27(3):1–15, 2008.

A. Shilov. Pci special interest group publishes pci express 3.0 standard, 2010. URL [http://www.xbitlabs.com/news/other/display/20101118151837\\\_PCI\\\_Special\\\_Interest\\\_Group\\\_Publishes\\\_PCI\\\_Express\\\_3\\\_0\\\_Standard.html](http://www.xbitlabs.com/news/other/display/20101118151837\_PCI\_Special\_Interest\_Group\_Publishes\_PCI\_Express\_3\_0\_Standard.html). Retrieved 24 February 2011.

## A. Index of symbols

### A.1. latin letters

Table 1: Index of symbols - latin letters

Symbol	Unit	Description
$A$	$m^2$	surface area
$a_s$	-	albedo of the ground surface
$c_p$	$J(kgK)^{-1}$	specific heat capacity of air (p=const)
$c_{wall}$	$J(kgK)^{-1}$	heat capacity of facade
$e$	$hPa$	water vapour pressure
$E$	$m^2s^{-2}$	turbulent kinetic energy
$f$	$s^{-1}$	coriolis parameter
$fvf$	-	facade view factor
$g$	$ms^{-2}$	gravitational acceleration
$g_s$	$mm s^{-1}$	stomatal conductance
$G$	$Wm^{-2}$	soil heat flux
$h_c$	$W(m^2K)^{-1}$	heat convection coefficient
$J_{f,evap}$	$ms^{-1}$	evaporation flux at surface of foliage
$J_{f,trans}$	$ms^{-1}$	transpiration flux at surface of foliage
$J_{f,h}$	$Kms^{-1}$	direct heat flux at surface of foliage
$K_\Phi$	$m^2s^{-1}$	turbulent exchange coefficient of $\Phi$
$K_h^w$	$m^2s^{-1}$	heat exchange coefficient at facade surface
LAD	$m^2m^{-3}$	leaf area density
N	1/8	cloud cover
x, y, z	$m$	cartesic coordinates
$p$	$Pa$	air pressure
$p'$	$Pa$	local pressure pertubation
$q$	$kgkg^{-1}$	specific air humidity
$Q_{lw}$	$Wm^{-2}$	long wave radiation
$Q_{sw}$	$Wm^{-2}$	short wave radiation
$Q_\Phi$	$ \Phi s^{-1}$	local source of $\Phi$
$S_u, S_v$ and $S_w$	$ms^{-2}$	local source or sink terms for impulse
$t$	$s$	time
$T_a$	$K$	air temperature
$T_f$	$K$	surface temperature of foliage
$T_{mrt}$	$K$	mean radiant temperature
$T_s$	$K$	soil temperature
$T_w$	$K$	temperature of facade
$\mathbf{u}$	$ms^{-1}$	three dimensional wind vector
$u, v, w$	$ms^{-1}$	wind speed in x, y and z direction
$u_g, v_g$	$ms^{-1}$	geostrophic wind speed in x and y direction
$V$	$m^3$	air volume
$vf$	-	view factor
$W$	$ms^{-1}$	mean wind speed

## A.2. greek letters

Table 2: Index of symbols - greek letters

Symbol	Unit	Description
$\Delta x, \Delta y, \Delta z$	$m$	dimension of the grid cells
$\epsilon$	$m^2 s^{-3}$	dissipation of kinetic energy
$\epsilon_f$	-	emissivity
$\eta$	$m^3 m^{-3}$	volumetric water content of the soil
$\lambda_w$	$W(m^2 K)^{-1}$	heat transfer coefficient of facade
$\rho$	$kg m^{-3}$	air density
$\rho$	$kg m^{-3}$	density of facade material
$\sigma_{svf}$	-	sky view factor
$\theta$	$K$	potential temperature

## B. Source code listings

Listing 1: Delphi source code of ADI routine of air temperature in x-direction

```
// ADI in X-direction
TRIfirst:=1;
TRIlLast:=II;
For j:= 2 to JJ-1 DO
  For k:=1 to KK-1 DO BEGIN

    // Definition of the main- and secondary diagonals
    For n:=2 to II-1 DO BEGIN // j,k = const
      aa[n]:=-AX[n,j,k];
      ab[n]:=-Bx[n,j,k]-Hilf2[n,j,k]+inv_dt;
      ac[n]:=-Cx[n,j,k];
    END;

    // Definition of the y-vector for the first step
    For n:=2 to II-1 DO
      Y[n]:= inv_dt*Hilf[n,j,k] - Ax[n,j,k]*T[n-1,j,k]
        - Bx[n,j,k]*T[n,j,k] - cx[n,j,k]*T[n+1,j,k]
        - Hilf2[n,j,k]*Hilf[n,j,k];

    // define open BC using EXPLICIT conditions
    // (using the boundary value from the last time step)
    AB[1]:=1; AC[1]:=0; y[1]:=T[1,j,k];
    ab[II]:=1; aa[II]:=0; Y[II]:=T[II,j,k];

  // Set BC matrix.
```

```

// (only either AC (inflow=1) or AA(inflow=II ,JJ) is needed)
if inflowX>0 then begin
  if BCtype_TQ=bc_forced then Begin
    y[InflowX]:=Temp_1D[k];
    AC[InflowX]:=0; AA[InflowX]:=0;
  end;
  if BCtype_TQ=bc_cyclic then Begin
    y[InflowX]:=T[outflowx ,j ,k];
    AC[InflowX]:=0; AA[InflowX]:=0;
  end;
end;

// call Tridiag (LU-Decomposition)
{$I ..\lib\TriDiag.inc}

// Save intermediary result for this column
For n:=1 to II DO Hilf[n,j ,k]:=Zw[n];

END; // loop over j ,k

```

Listing 2: Delphi source code for LU-decomposition

```

// TRIDIAG Routine
//
// needs defined:
//   TRIfirst, TRIlast: first/ last Grid used
//   TRILoop:
//   bet: Double;
//   gam: Array [0.. maximum_of_grids] of Double;
//
// Set TRIfirst and TRIlast to define
// borders of Vektor/Matrix
// (Try to set them OUTSIDE any loops !
// Most of the time they are
// constant over large parts of code !)
//
//
// Code for Matrix Inversion via LU Decomposition
// (works only on spare "TRIDIAG" Matrixes)
// <<bet>> changed to its inverse operator **
bet:=1/ab[TRIfirst]; ZW[TRIfirst]:= y[TRIfirst]*bet;
For TRILoop:=TRIfirst+1 to TRIlast DO BEGIN
  gam[TRILoop]:=ac[TRILoop-1]*bet;
  bet:=1/( ab[TRILoop]-aa[TRILoop]*gam[TRILoop] );
  ZW[TRILoop]:=( y[TRILoop]-aa[TRILoop]*ZW[TRILoop-1])*bet;
  END; { *Loop* }

For TRILoop:=TRIlast-1 Downto TRIfirst DO
  ZW[TRILoop]:=ZW[TRILoop]-gam[TRILoop+1]*ZW[TRILoop+1];

```

Listing 3: OpenCL kernel for (complete) ADI of air temperature in x-direction

```

/*****
** OPENCL Kernel for tridiag of Temperature ****
*****
***** May 2010 ****
*****
*/
//----- x- direction -----
__kernel void ADI_Temp_x(__global const float* _ax,
                        __global const float* _bx,
                        __global const float* _cx,
                        __global const float* _t,
                        __global float* _hilf,
                        __global const float* _hilf2,
                        __global const float* _temp_1d,
                        float _inv_dt,
                        int _mx,
                        int _my,
                        int _mz,
                        int _ii,
                        int _jj,
                        int _kk,
                        int _BCtype_Tq,
                        int _inflowx,
                        int _outflowx)
{
// local arrays
float AA[500]; float AB[500]; float AC[500];
float y[500]; float gam[500];
//local vars
int k,n,i,TRILoop;
float bet;

// x,y point in grid
int ty = get_global_id(0); if(ty>=_jj){return;}
int tz = get_global_id(1); if(tz>=_kk){return;}
int m = ty*_mz+tz;

// predefine variables
{ long n_end = _ii ; for(n = 2 ; n < n_end ; ++n) {
AA[n] =-_ax[n*_my*_mz+m];

```



```

AB[n] = -_bx [n*_my*_mz+m] - _hilf2 [n*_my*_mz+m] + _inv_dt ;
AC[n] = -_cx [n*_my*_mz+m] ;
y [n] = _inv_dt * _hilf [n*_my*_mz+m]
      - _ax [n*_my*_mz+m] * _t [(n-1)*_my*_mz+m]
      - _bx [n*_my*_mz+m] * _t [n*_my*_mz+m]
      - _cx [n*_my*_mz+m] * _t [(n+1)*_my*_mz+m]
      - _hilf2 [n*_my*_mz+m] * _hilf [n*_my*_mz+m] ;
}}

// define open BC using EXPLICIT conditions
// (using the boundary value from the last time step)
AB[1] = 1; AC[1] = 0; y[1] = _t [_my*_mz+m] ;
AB[_ii] = 1; AA[_ii] = 0; y[_ii] = _t [_ii*_my*_mz+m] ;

// Set BC matrix.
// (only either AC (inflow=1) or AA(inflow=ii ,jj) is needed)
if (_BCtype_Tq==2) {
  y[_inflowx] = _temp_1d[tz] ;
  AC[_inflowx] = 0; AA[_inflowx] = 0;
}
if (_BCtype_Tq==3) {
  y[_inflowx] = _t [_outflowx*_my*_mz+m] ;
  AC[_inflowx] = 0; AA[_inflowx] = 0;
}

// LU-decomposition
bet = 1/AB[1] ;
_hilf [_my*_mz+m] = y[1] * bet ;
for (TRILoop=2; TRILoop<=_ii; ++TRILoop){
  gam [TRILoop] = AC [TRILoop-1] * bet ;
  bet = 1 / ( AB [TRILoop] - AA [TRILoop] * gam [TRILoop] ) ;
  _hilf [TRILoop*_my*_mz+m] = (y [TRILoop] - AA [TRILoop] *
    _hilf [(TRILoop-1)*_my*_mz+m]) * bet ;
}

for (TRILoop=_ii-1; TRILoop>=1; --TRILoop){
  _hilf [TRILoop*_my*_mz+m] = _hilf [TRILoop*_my*_mz+m] -
gam [TRILoop+1] * _hilf [(TRILoop+1)*_my*_mz+m] ;
}
}

```

Listing 4: C++ source code for launching the OpenCl kernel of ADI for air temperature in x-direction

```

// Allocate the OpenCL buffer memory objects for source and
// result on the device (once for all)
cm_ax = clCreateBuffer(cxGPUContext,
    CLMEM_READ_WRITE | CLMEM_COPY_HOST_PTR,
    sizeof(cl_float) * (max_x+1)*(max_y+1)*(max_z+1) ,
    ax, &ciErrNum);
shrCheckError(ciErrNum, CL_SUCCESS);
cm_ay = clCreateBuffer(cxGPUContext,
    CLMEM_READ_ONLY | CLMEM_COPY_HOST_PTR,
    sizeof(cl_float) * (max_x+1)*(max_y+1)*(max_z+1) ,
    ay, &ciErrNum);
shrCheckError(ciErrNum, CL_SUCCESS);
cm_az = clCreateBuffer(cxGPUContext,
    CLMEM_READ_ONLY | CLMEM_COPY_HOST_PTR,
    sizeof(cl_float) * (max_x+1)*(max_y+1)*(max_z+1) ,
    az, &ciErrNum);
shrCheckError(ciErrNum, CL_SUCCESS);
cm_bx = clCreateBuffer(cxGPUContext,
    CLMEM_READ_ONLY | CLMEM_COPY_HOST_PTR,
    sizeof(cl_float) * (max_x+1)*(max_y+1)*(max_z+1) ,
    bx, &ciErrNum);
shrCheckError(ciErrNum, CL_SUCCESS);
cm_by = clCreateBuffer(cxGPUContext,
    CLMEM_READ_ONLY | CLMEM_COPY_HOST_PTR,
    sizeof(cl_float) * (max_x+1)*(max_y+1)*(max_z+1) ,
    by, &ciErrNum);
shrCheckError(ciErrNum, CL_SUCCESS);
cm_bz = clCreateBuffer(cxGPUContext,
    CLMEM_READ_ONLY | CLMEM_COPY_HOST_PTR,
    sizeof(cl_float) * (max_x+1)*(max_y+1)*(max_z+1) ,
    bz, &ciErrNum);
shrCheckError(ciErrNum, CL_SUCCESS);
cm_cx = clCreateBuffer(cxGPUContext,
    CLMEM_READ_ONLY | CLMEM_COPY_HOST_PTR,
    sizeof(cl_float) * (max_x+1)*(max_y+1)*(max_z+1) ,
    cx, &ciErrNum);
shrCheckError(ciErrNum, CL_SUCCESS);
cm_cy = clCreateBuffer(cxGPUContext,
    CLMEM_READ_ONLY | CLMEM_COPY_HOST_PTR,
    sizeof(cl_float) * (max_x+1)*(max_y+1)*(max_z+1) ,

```

```

        cy, &ciErrNum);
shrCheckError(ciErrNum, CL_SUCCESS);
cm_cz = clCreateBuffer(cxGPUContext,
    CLMEM_READ_ONLY | CLMEM_COPY_HOST_PTR,
    sizeof(cl_float) * (max_x+1)*(max_y+1)*(max_z+1),
    cz, &ciErrNum);
shrCheckError(ciErrNum, CL_SUCCESS);
cm_t = clCreateBuffer(cxGPUContext,
    CLMEM_READ_ONLY | CLMEM_COPY_HOST_PTR,
    sizeof(cl_float) * (max_x+1)*(max_y+1)*(max_z+1),
    t, &ciErrNum);
shrCheckError(ciErrNum, CL_SUCCESS);
cm_quell_t = clCreateBuffer(cxGPUContext,
    CLMEM_READ_ONLY | CLMEM_COPY_HOST_PTR,
    sizeof(cl_float) * (max_x+1)*(max_y+1)*(max_z+2),
    quell_t, &ciErrNum);
shrCheckError(ciErrNum, CL_SUCCESS);
cm_hilf = clCreateBuffer(cxGPUContext,
    CLMEM_READ_WRITE | CLMEM_COPY_HOST_PTR,
    sizeof(cl_float) * (max_x+1)*(max_y+1)*(max_z+1),
    hilf, &ciErrNum);
shrCheckError(ciErrNum, CL_SUCCESS);
cm_hilf2 = clCreateBuffer(cxGPUContext,
    CLMEM_READ_ONLY | CLMEM_COPY_HOST_PTR,
    sizeof(cl_float) * (max_x+1)*(max_y+1)*(max_z+1),
    hilf2, &ciErrNum);
shrCheckError(ciErrNum, CL_SUCCESS);
cm_tchange = clCreateBuffer(cxGPUContext,
    CLMEM_READ_WRITE | CLMEM_COPY_HOST_PTR,
    sizeof(cl_float) * (max_x+1)*(max_y+1)*(max_z+1),
    tchange, &ciErrNum);
shrCheckError(ciErrNum, CL_SUCCESS);
cm_localSprayCooling = clCreateBuffer(cxGPUContext,
    CLMEM_READ_ONLY | CLMEM_COPY_HOST_PTR,
    sizeof(cl_float) * (max_x+1)*(max_y+1)*(max_z+1),
    localSprayCooling, &ciErrNum);
shrCheckError(ciErrNum, CL_SUCCESS);
cm_Restterm = clCreateBuffer(cxGPUContext,
    CLMEM_READ_ONLY | CLMEM_COPY_HOST_PTR,
    sizeof(cl_float) * (max_x+1)*(max_y+1)*(max_z+1),
    Restterm, &ciErrNum);
shrCheckError(ciErrNum, CL_SUCCESS);
cm_temp_1d = clCreateBuffer(cxGPUContext,
    CLMEM_READ_ONLY | CLMEM_COPY_HOST_PTR,

```

```

        sizeof( cl_float ) * ( max_zges+1 ) ,
        ltemp_1d , &ciErrNum );
shrCheckError( ciErrNum , CL_SUCCESS );

//--- ADI x-direction (opencl)---
int lifx = inflowx;
int lofx = outflowx;
int lbc_tq = BCtype_Tq;
gettimeofday(&start , NULL);

// Set the Argument values
ciErrNum = clSetKernelArg( ADI_temp_x_kernel ,
                           0 , sizeof( cl_mem ) , ( void* ) &cm_ax );
ciErrNum |= clSetKernelArg( ADI_temp_x_kernel ,
                           1 , sizeof( cl_mem ) , ( void* ) &cm_bx );
ciErrNum |= clSetKernelArg( ADI_temp_x_kernel ,
                           2 , sizeof( cl_mem ) , ( void* ) &cm_cx );
ciErrNum |= clSetKernelArg( ADI_temp_x_kernel ,
                           3 , sizeof( cl_mem ) , ( void* ) &cm_t );
ciErrNum |= clSetKernelArg( ADI_temp_x_kernel ,
                           4 , sizeof( cl_mem ) , ( void* ) &cm_hilf );
ciErrNum |= clSetKernelArg( ADI_temp_x_kernel ,
                           5 , sizeof( cl_mem ) , ( void* ) &cm_hilf2 );
ciErrNum |= clSetKernelArg( ADI_temp_x_kernel ,
                           6 , sizeof( cl_mem ) , ( void* ) &cm_temp_1d );
ciErrNum |= clSetKernelArg( ADI_temp_x_kernel ,
                           7 , sizeof( cl_float ) , ( void* ) &linv_dt );
ciErrNum |= clSetKernelArg( ADI_temp_x_kernel ,
                           8 , sizeof( cl_int ) , ( void* ) &mx );
ciErrNum |= clSetKernelArg( ADI_temp_x_kernel ,
                           9 , sizeof( cl_int ) , ( void* ) &my );
ciErrNum |= clSetKernelArg( ADI_temp_x_kernel ,
                           10 , sizeof( cl_int ) , ( void* ) &mz );
ciErrNum |= clSetKernelArg( ADI_temp_x_kernel ,
                           11 , sizeof( cl_int ) , ( void* ) &lii );
ciErrNum |= clSetKernelArg( ADI_temp_x_kernel ,
                           12 , sizeof( cl_int ) , ( void* ) &ljj );
ciErrNum |= clSetKernelArg( ADI_temp_x_kernel ,
                           13 , sizeof( cl_int ) , ( void* ) &lkk );
ciErrNum |= clSetKernelArg( ADI_temp_x_kernel ,
                           14 , sizeof( cl_int ) , ( void* ) &lbc_tq );
ciErrNum |= clSetKernelArg( ADI_temp_x_kernel ,
                           15 , sizeof( cl_int ) , ( void* ) &lifx );

```

```

ciErrNum |= clSetKernelArg(ADI_temp_x_kernel,
                          16, sizeof(cl_int), (void*)&lofx);
shrCheckError(ciErrNum, CL_SUCCESS);

clEnqueueWriteBuffer(cqCommandQueue, cm_hilf,
                    CL_FALSE, 0, sizeof(cl_float) *
                    (max_x+1)*(max_y+1)*(max_z+1),
                    hilf, 0, NULL, NULL);

szLocalWorkSize[0]=16;
szLocalWorkSize[1]=16;
szGlobalWorkSize[0]=shrRoundUp(szLocalWorkSize[0], jj);
szGlobalWorkSize[1]=shrRoundUp(szLocalWorkSize[1], kk);

// Launch kernel
ciErrNum = clEnqueueNDRangeKernel(cqCommandQueue,
                                  ADI_temp_x_kernel, 2, NULL, szGlobalWorkSize,
                                  szLocalWorkSize, 0, NULL, NULL);
shrCheckError(ciErrNum, CL_SUCCESS);

// Read back results and check accumulated errors
ciErrNum = clEnqueueReadBuffer(cqCommandQueue,
                               cm_hilf, CL_TRUE, 0, sizeof(cl_float) *
                               (max_x+1)*(max_y+1)*(max_z+1), hilf,
                               0, NULL, NULL);
shrCheckError(ciErrNum, CL_SUCCESS);

```

## C. List of figures

### List of Figures

1.	Schematic of vertical grid layout with a.) constant b.) telescoping grid . . .	6
2.	Schematic of basic model layout . . . . .	7
3.	Schematic of the sub models of ENVI-met. . . . .	8
1.	Schematic of the new 3-node model . . . . .	30
2.	Building block with three different building zones (color coded). The energy budget and indoor temperature is calculated separately for each of the three building zones. . . . .	33
3.	Comparison of simulated surface temperature of a westward facade for a cloudless summer day (23.06.) between old and new facade model. (Albedo=0.3; Heat transmission = $4.3 Wm^{-2}K^{-1}$ ) . . . . .	35
4.	Comparison of simulated facade temperatures of a westward facade for a cloudless summer day between fixed and variable indoor temperature. . .	36
5.	Example of single walls in model area. . . . .	36
6.	Prototype of the new model area editor for ENVI-met . . . . .	38
7.	Wall directions. . . . .	39
8.	Transformation of a complex polygon based 3D model (rear) into block based ENVI-met model area (front) . . . . .	40
9.	Boundary conditions for incoming long wave and short wave (direct and diffuse) radiation. Measurements taken by on-site weather station. . . . .	41
10.	Model area and building with test roofs (top left). Facade materials and soil type color-coded . . . . .	42
11.	Measurements of wind speed and boundary conditions for simulation in 10m above ground. Black line: moving average (60 minutes) of measurements. Grey triangles: values used for the boundary conditions of the simulation. . . . .	42
12.	Air temperature in 2m above ground at inflow boundary. . . . .	43
13.	Measured and simulated surface temperature of black roof element . . . . .	44
14.	Measured and simulated surface temperature of grey roof element . . . . .	45
15.	Measured and simulated surface temperature of white roof element . . . . .	45
16.	Measured and simulated surface temperature of silver roof element . . . . .	46
17.	Modeled surface temperature of a complex building model. . . . .	48
1.	Concept of nesting: a high resolution nesting area (red) is positioned within a coarser resolution model area (black) that provides the lateral boundary conditions for the nesting area. . . . .	55
2.	Schematic work flow of ENVI-met with Forcing enabled . . . . .	58
3.	Model area Erbprinzenstrasse (372 x 236m). Buildings (grey), vegetation (green) and surface materials color coded. Red dot: measurement site. . .	62
4.	Model area Vauban (512 x 386m). Buildings (grey), vegetation (green) and surface materials color coded. . . . .	63

5.	Positions of stationary (1) and mobile (2-5) measurement sites within model area . . . . .	64
6.	Comparison between measured and simulated air temperature $T_a$ , Mean radiant temperature $T_{mrt}$ and PET in 2m above ground level, May 24th 2007. . . . .	65
7.	Comparison between measured and simulated relative humidity RH and wind speed $v$ in 2m above ground level, May 24th 2007. . . . .	66
1.	Map of Freiburg with simulated model areas and measurement sites . . .	73
2.	Map of quarter Vauban. . . . .	75
3.	Map of quarter Wiehre. . . . .	76
4.	Diurnal variation of the surface temperature of natural soil (grid 101,91) compared to surface temperature of a paved street (grid 97,119). . . . .	77
5.	PET and wind speed at 14CET in 1.8m above ground in model area Vauban. . . . .	78
6.	PET at 22CET in 1.8m above ground in model area Vauban. . . . .	79
7.	Air temperature and wind speed in 1.5m above ground at 14CET in model area Wiehre. . . . .	80
8.	PET in 1.5m above ground at 14CET in model area Wiehre. . . . .	81
9.	Geometrical layout of the synthetic canyon used in the simulations. . . .	87
10.	PET in 1.8m above ground averaged over whole street canyon. E-W orientation. $H/W=1$ . . . . .	88
11.	PET in 1.8m above ground averaged over southern pavement. E-W orientation. $H/W=1$ . . . . .	89
12.	PET in 1.8m above ground averaged over northern pavement. E-W orientation. $H/W=1$ . . . . .	90
13.	PET in 1.8m above ground averaged over whole street canyon. N-S orientation. $H/W=1$ . . . . .	91
14.	PET in 1.8m above ground averaged over eastern pavement. N-S orientation. $H/W=1$ . . . . .	92
15.	PET in 1.8m above ground averaged over western pavement. N-S orientation. $H/W=1$ . . . . .	93
16.	PET in 1.8m above ground averaged over whole street canyon. E-W orientation. $H/W=2$ . . . . .	94
17.	PET in 1.8m above ground averaged over whole street canyon. N-S orientation. $H/W=2$ . . . . .	95
1.	Members of the Khronos group. Source: <a href="http://www.khronos.org/about/">http://www.khronos.org/about/</a>	102
2.	Schematic of an OpenCL system. . . . .	104
3.	Platform model of OpenCL. . . . .	104
4.	Example showing index space, work-group and work-items with their global IDs. . . . .	105
5.	Schematic of memory concept of OpenCL. . . . .	106
6.	Schematic of grid. . . . .	109
7.	Comparison of computing time for ADI routine for potential temperature between CPU and GPU . . . . .	112

8.	Schematic of overlapping borders. . . . .	114
9.	Schematic of possible decompositions of a model area. a.) Decomposition along x-axis. b.) decomposition along y-axis. c.) decomposition along x- and y-axis. . . . .	116
10.	Schematic of exchange of centered variables between the sub-areas. . . .	117
11.	Schematic of exchange of wind components between the sub-areas. . . .	117



## D. List of tables

### List of Tables

1.	physical properties of selected roof elements . . . . .	43
2.	Comparison between measured and simulated facade surface temperatures. Average deviation and root mean square error . . . . .	46
1.	Root mean squared error of compared variables for different spans of time at survey area Erbprinzenstrasse . . . . .	67
2.	Root mean squared error for selected variables at measurement points in model area Vauban . . . . .	68
1.	Size and resolution of the model areas (Note: model Wiehre has a telescoping vertical grid) . . . . .	73
2.	Overview of modeled canyons . . . . .	86
1.	Comparison of computing times of ADI routine between CPU and GPU. Size of model area: 150x150x35 (=787500) grid cells. . . . .	113
1.	Index of symbols - latin letters . . . . .	122
2.	Index of symbols - greek letters . . . . .	123



